

The Pennsylvania State University  
The Graduate School  
Department of Mechanical and Nuclear Engineering

**EFFECTS OF RUST DEPOSITION AT THE  
AXIAL SEAL PIN BETWEEN TWO BLADES**

A Thesis in  
Mechanical Engineering

by  
Duane L. Breneman

© 2011 by Duane L. Breneman

Submitted in Partial Fulfillment  
of the Requirements  
for the Degree of  
Master of Science

December 2011

The thesis of Duane L. Breneman was reviewed and approved\* by the following:

Karen A. Thole  
Head of the Department of Mechanical and Nuclear Engineering  
Professor of Mechanical Engineering  
Thesis Advisor

Daniel C. Haworth  
Professor-In-Charge of MNE Graduate Programs  
Professor of Mechanical Engineering

Horacio Perez-Blanco  
Professor of Mechanical Engineering

\*Signatures are on file in the Graduate School.

## **ABSTRACT**

Rust deposits in the gap associated with the axial seal pin between two turbine blades can inhibit the vibration dampening of the pin, which can ultimately result in premature failure of components. This study investigated mechanisms leading to rust deposition in the axial seal pin between two blades. An initial particle characterization study revealed that one of the dominating effects on rust deposition is centrifugal forces. Rotation compacts rust particles significantly, doubling their bulk density when spun at engine representative forces. Static and rotating test facilities were developed to flow compressed air and particles through full-scale engine hardware and test coupons representative of the axial seal pin geometry. Rust was injected at ambient temperatures and engine-realistic pressure ratios. Reductions in flow were measured to be as high as 74%. In static tests, increasing the pressure ratio increased flow blockage for a given rust amount, whereas in rotating tests, flow blockage was independent of pressure ratio. The amount of blockage was highly sensitive to the geometry of associated area near the axial seal pin particularly under rotating conditions.

## TABLE OF CONTENTS

LIST OF TABLES .....	vi
LIST OF FIGURES .....	vii
ACKNOWLEDGEMENTS .....	x
NOMENCLATURE .....	xi
Chapter 1. INTRODUCTION .....	1
Chapter 2. RELEVANT PAST STUDIES .....	3
2.1 Mechanisms for Particle Delivery and Deposition .....	3
2.2 Previous Gas Turbine Deposition Studies.....	3
2.3 Uniqueness of the Present Study.....	7
Chapter 3. EXPERIMENTAL FACILITY AND METHODOLOGY .....	9
3.1 Creation of Representative Particle Samples .....	9
3.2 Particle Heating Tests and Procedures .....	12
3.3 Particle Centrifuge Tests and Procedures.....	15
3.4 Test Facilities .....	17
3.5 Description of Engine Hardware and Flow Area .....	25
3.6 Description of Rotating Test Coupons .....	30
3.7 Data Analysis .....	34
3.8 Procedure for Static Tests .....	41
3.9 Procedure for Rotating Tests.....	44
3.10 Comparison of Static Baseline and Predicted Flow Functions.....	46
3.11 Comparison of Static and Rotating Baseline Flow Functions .....	52
3.12 Derivation of Test Matrices .....	53
3.13 Uncertainty Analysis .....	56
Chapter 4. RESULTS FROM STATIC TESTS .....	58
4.1 Effect of Heating .....	58
4.2 Effect of Centrifugal Forces .....	62
4.3 Effect of Rust Injection on Engine Hardware .....	64
Chapter 5. RESULTS FROM ROTATING TESTS.....	79
5.1 Rust Deposition.....	79
5.2 Flow Blockage.....	84
Chapter 6. CONCLUSIONS.....	88
REFERENCES .....	91
Appendix A. CALCULATIONS FOR STATIC TESTS.....	94
Nomenclature.....	94
Flow Function Calculation.....	94
Blockage Calculation .....	96
References .....	97
Appendix B. CALCULATIONS FOR ROTATING TESTS .....	98
Nomenclature.....	98
Overview.....	98
Chamber Differential Pressure Correction.....	99
Appendix C. UNCERTAINTY ANALYSIS FOR STATIC TESTS .....	102
Nomenclature.....	102
Flow Function Uncertainty .....	102

Reduction in Flow Function Uncertainty.....	105
References.....	107
Appendix D. UNCERTAINTY ANALYSIS FOR ROTATING TESTS.....	108
Nomenclature.....	108
Flow Function Uncertainty .....	109
Reduction in Flow Function Uncertainty.....	113
References.....	113
Appendix E. ENGINEERING DRAWINGS.....	114

## LIST OF TABLES

Table 3.1. Elemental Compositions of Turbine Samples and Representative Laboratory Particle Mixtures .....	10
Table 3.2. Metal Oxide Mixture 5 Composition.....	10
Table 3.3. Elemental Compositions of Samples from Field-Run Blade.....	12
Table 3.4. Particle Heating Test Matrix .....	13
Table 3.5. Particle Centrifuging Test Matrix .....	16
Table 3.6. Static Test Facility Cross-sectional Flow Areas .....	18
Table 3.7. Centrifugal Acceleration in Engine and Rotating Test Facility.....	21
Table 3.8. Surface Finishes of Engine Hardware and Plunge-EDM Samples .....	34
Table 3.13. Test Matrix for Static Tests .....	54
Table 3.14. Test Matrix for Rotating Tests.....	55
Table 3.15. Parameter Nominal Values and Uncertainties for Static Tests .....	56
Table 3.16. Parameter Nominal Values and Uncertainties for Tests at $\Omega = 0.002$ .....	57
Table 3.17. Parameter Nominal Values and Uncertainties for Tests at $\Omega = 1$ .....	57
Table 4.1. Particle Heating Tests for Samples of Various Compositions.....	59
Table 4.2. Particle Heating Tests for Engine Representative Compositions .....	60
Table 4.3. Particle Centrifuging Tests .....	63

## LIST OF FIGURES

Figure 1.1. Two adjacent turbine blades with air leakage at the axial seal pin. ....	2
Figure 3.1. The mixture 5 size distribution included the range of particle sizes found in Payne Creek CT1. ....	11
Figure 3.2. Particle sample locations on the field-run blade. ....	12
Figure 3.3. Comparison of particle composition before and after heating in the kiln. ....	14
Figure 3.4. Metal oxide particles shown while being heated in the kiln. ....	15
Figure 3.5. Metal oxide particles shown after being heated in the kiln and cooling to room temperature (same samples as in Figure 3.4). ....	15
Figure 3.6. Centrifuge tube containing a particle sample. ....	16
Figure 3.7. A schematic of the static test facility used for rust injection studies. ....	17
Figure 3.8. The static test chamber was designed to contain two turbine blades in a configuration representative of their positions in an engine rotor. ....	19
Figure 3.9. A schematic of the rotating test facility used for rust injection studies. ....	21
Figure 3.10. Top view of rotating chamber with lid removed. ....	24
Figure 3.11. Particle diffuser plate position relative to test coupon. ....	24
Figure 3.12. Two blades from the first row of a land-based gas turbine engine. ....	26
Figure 3.13. The installation of the blades as viewed from the underside of the test chamber. ..	27
Figure 3.14. The flow area at the seal pin as viewed from the front of the test chamber (front panel, front bar, and front blade removed for clarity). ....	27
Figure 3.15. The seal pin clearance consisted of two clearance gaps between the seal pin and rear and front blade platforms (side cross-sectional view). ....	28
Figure 3.16. Data from multiple test chamber assemblies were compared to show consistency in the flow area. ....	29
Figure 3.17. The section of the engine hardware used to create the rotating test coupon (dimensions in mm). ....	30
Figure 3.18. Coupon 1 had a lip near the seal pin contact area, while coupon 2 had the lip removed for a smooth transition. ....	32
Figure 3.19. Three-dimensional optical profilometry surface plot for engine hardware. ....	33
Figure 3.20. Three-dimensional optical profilometry surface plot for plunge-EDM sample 4. ..	33
Figure 3.21. The seal pin flow area may be approximated as a nozzle downstream of a large reservoir. ....	35
Figure 3.22. The predicted flow function versus pressure ratio curve for the assumed seal pin flow area and discharge coefficient. ....	39
Figure 3.23. Baseline flow function for clean engine hardware. ....	41
Figure 3.24. Blocked flow conditions reached steady values shortly after injecting rust particles (shown for rust mass of 0.23 g). ....	43
Figure 3.25. Blockage was measured in terms of a reduction in flow function evaluated at the blocked pressure ratio (zoomed view shown). ....	44
Figure 3.26. Flow function for flow through a single coupon 1 at $\Omega = 0.002$ . ....	45
Figure 3.27. Baseline flow functions for coupons 1 and 2 at $\Omega = 0.002$ and $\Omega = 1$ with three identical coupons open to flow. ....	46
Figure 3.28. Predicted flow function and experimental curve fit flow function for clean engine hardware, static tests. ....	47

Figure 3.29. The ratio of experimental to predicted flow functions varied with pressure ratio for the static tests. ....	48
Figure 3.30. Flow of gas through a nozzle with a non-ideal entrance condition; low and high pressure ratio cases [28]. ....	49
Figure 3.31. Effective seal pin flow area as a function of pressure ratio for engine hardware. ..	52
Figure 3.32. Comparison of scaled rotating coupon flow function with full-scale static engine hardware. ....	53
Figure 4.1. Metal oxide particles shown initially and at various temperatures during heating (Sample numbers correspond to test numbers in Table 4.1.). ....	59
Figure 4.2. Visual comparison of unheated mixture 5 particles (left) with particles heated to 850°C (right), scale in inches. ....	61
Figure 4.3. Size distributions for unheated and heated particles. Particle size tests were performed at ambient conditions following heating. ....	62
Figure 4.4. Size distributions for particles heated for varying lengths time. ....	62
Figure 4.5. Centrifuged particles shown before and after removal from the centrifuge tube. ....	64
Figure 4.6. Rust deposits on the rear face of the front blade after injecting 0.23 g of rust. ....	65
Figure 4.7. Rust deposits on the front face of the rear blade after injecting 0.23 g of rust; shown after removing the seal pin. ....	65
Figure 4.8. Blockage versus injected rust mass for three pressure ratios. ....	66
Figure 4.9. Blockage versus rust mass to air mass flow rate ratio for three pressure ratios. ....	67
Figure 4.10. Comparison of single-quantity and cumulative rust injection tests performed at a pressure ratio of 1.15. ....	68
Figure 4.11. Blockage versus pressure ratio for various injected rust masses. ....	69
Figure 4.12. Larger particles deposited upstream of the seal pin in the large flow area between the seal pin and the root. ....	71
Figure 4.13. Very small particles deposited at the narrowest flow area where the seal pin contacted the front blade. ....	71
Figure 4.14. Deposition sample locations for ESEM particle size analysis. ....	72
Figure 4.15. ESEM images of rust particles at 500x magnification; sample numbers correspond with labels in Figure 4.14. ....	73
Figure 4.16. An ESEM image divided into 9 cells with particles encircled for size analysis. ....	74
Figure 4.17. Histograms of particle sizes from deposition samples; sample numbers correspond with locations given in Figure 4.14. ....	75
Figure 4.18. Test chamber positions for rust injection testing and disassembly. ....	76
Figure 4.19. Maximum blockage test for cumulative total rust injection of 5.3 g at a pressure ratio of 1.15. ....	77
Figure 5.1. Rust deposition locations inside the rotating chamber. ....	80
Figure 5.2. Rust deposition by location for coupon 1, $PR_{rot} = 1.6$ , $\Omega = 0.002$ . ....	80
Figure 5.3. Rust deposition by location for coupon 1, $PR_{rot} = 1.6$ , $\Omega = 1$ . ....	81
Figure 5.4. Rust deposition in coupon 1 after at test performed at $\Omega = 1$ , $PR_{rot} = 1.6$ (outward radial view). ....	81
Figure 5.5. Rust deposition in coupon 1 after tests performed at $PR_{rot} = 1.6$ (scale in inches). ..	82
Figure 5.6. Rust deposition in coupon 2 after tests performed at $PR_{rot} = 1.6$ (scale in inches). ..	83
Figure 5.7. Rust deposition in coupon 1 after rust injection test at $\Omega = 1$ compared with a blade removed from field service (seal pins removed) [1]. ....	84
Figure 5.8. Flow blockage as a function of deposited rust mass, coupon 1, $\Omega = 0.002$ . ....	85



Figure 5.9. Flow blockage as a function of deposited rust mass, coupons 1 and 2, $\Omega = 0.002$ and $\Omega = 1$ , $PR_{rot} = 1.6$ . .....	86
Figure 5.10. Coupon 1 before and after removal of rust deposited on trailing contoured surface. ....	87
Figure 6.1. Original blade platform design and proposed modification. ....	90

## **ACKNOWLEDGEMENTS**

There are many individuals who made the work presented in this thesis possible. First and foremost, I want thank my advisor, Karen, for all of her efforts in providing this research opportunity and for supporting me through the graduate program. Her technical expertise and optimism were invaluable as we worked through research challenges together. I am also especially grateful to Mike, our research associate, for his technical advice and support. It was a pleasure working with so many great lab mates. Robert, Jason, Seth, Alan, Molly, Steve L., Greg, Steve W., Nick, Amy, Jeff, Ken, and Katie – I will miss working with you all. I will especially miss running with Robert, Jason, Seth, and Greg. I want to credit Phil and the folks at Engineering Shop Services for all of their skilled machining work on this project. I am also grateful to our undergraduate assistants, Brian and Chris, for their help. Finally, I want to thank Siemens Energy for providing funding for this work. It was a pleasure working with Vince and Kok-Mun, the project monitors.

Many people also supported me in a relational sense throughout this project. I am extremely grateful to my wife, Stephanie, for her love and encouragement as she walked along side me through graduate school. I am thankful for my parents' unwavering care and support. My brother, Kyle, and sister-in-law Danielle encouraged me many times through their phone calls and emails. I am grateful for the listening ear I often found in my friend Jim Charles. I am also thankful for many friends who made State College a brighter place with their hospitality and friendship. I was especially blessed through friendships with Robert and Ariel, Eric and Ruth, Luke and Hannah, Kiron and Rachel, and the people of University Mennonite Church. Finally, I give thanks to God for His love and gift of salvation. The peace and hope available through His son Jesus Christ sustains eternally.

# NOMENCLATURE

## General

$a_c$	centrifugal acceleration
$a_{c,e}$	engine centrifugal acceleration at base load conditions
$A$	area
$A_{sp}$	seal pin flow area based on the assumed seal pin clearance
$c$	speed of sound
$c_p$	specific heat
$C_D$	discharge coefficient
$CF$	correction factor: $CF = \frac{FF_0}{FF_p}$
$d$	diameter
$FF$	static dimensional flow function: $FF = \frac{\dot{m}\sqrt{T_0}}{P_0} \quad (m \cdot s \cdot K^{1/2})$
$FF_p$	predicted flow function from isentropic flow relations and the assumed seal pin flow area and discharge coefficient
$FF_{rot}$	rotational dimensional flow function: $FF_{rot} = \frac{\dot{m}\sqrt{T_{0,rot}}}{P_{0,rot}} \quad (m \cdot s \cdot K^{1/2})$
$FF_0$	baseline static flow function from curve fit of flow data for clean engine hardware
$FF_{0,rot}$	baseline rotational flow function from curve fit of flow data for clean test coupons
$FP$	nondimensional flow parameter: $FP = \frac{\dot{m}\sqrt{R \cdot T_0}}{A \cdot P_0}$
$L_c$	characteristic length scale
$L_{sp}$	seal pin length
$LFE$	laminar flow element
$m_{rust}$	rust mass
$\dot{m}$	mass flow rate
$Ma$	Mach number
$MLR$	mass loading ratio: $MLR = \frac{m_{rust}}{\dot{m}_{air}} \quad (s)$
$p$	static pressure
$P_0$	total pressure upstream of the nozzle or seal pin flow area
$P_{0,rot}$	rotational total pressure upstream of the nozzle or seal pin flow area
$PR$	upstream total to downstream static pressure ratio: $PR = \frac{P_0}{p_b}$
$PR_{rot}$	upstream total rotational to downstream static pressure ratio: $PR_{rot} = \frac{P_{0,rot}}{p_b}$
$r$	radius
$R$	gas constant

$R_q$	root-mean-square average surface height relative to the mean
$Re$	Reynolds number
$RFF$	reduction in flow function evaluated at blocked pressure ratio: $RFF = 1 - \frac{FF}{FF_0} \Big _{PR}$
$Stk$	Stokes number: $Stk = \frac{\tau_p}{\tau_f}$
$T$	temperature
$T_0$	total temperature upstream of the nozzle or seal pin flow area
$T_{rot}$	rotational temperature
$T_{0,rot}$	rotational total temperature upstream of the nozzle or seal pin flow area
$t_{sp}$	assumed seal pin clearance for one-dimensional analysis
$v$	velocity

### Greek

$\gamma$	ratio of specific heats
$\mu$	dynamic viscosity
$\rho$	density
$\rho_l$	bulk density before centrifuging
$\rho_c$	bulk density after centrifuging
$\tau$	time scale
$\omega$	rotating speed
$\Omega$	centrifugal acceleration relative to engine: $\Omega = \frac{a_c}{a_{c,e}}$

### Subscripts

$b$	evaluated downstream of the nozzle or seal pin flow area
$f$	fluid
$p$	particle
$r$	radial component
$th$	evaluated at the nozzle throat or seal pin flow area

## Chapter 1. INTRODUCTION

Land-based gas turbine engines provide one of the most operationally flexible forms of fossil fuel power generation due to their relatively short startup times and their ability to ramp up and down to meet changing power demands. Because of their operational flexibility, gas turbines may be used intermittently and experience significant down time, during which particulate matter such as rust can build up in air supply piping and other components susceptible to oxidation. Upon startup of the engine, rust particles enter the engine and can deposit throughout flow passages in the engine. Deposition has the potential to significantly reduce the flow through small passages and even alter the performance of structural components.

One particular area where rust particles have been found to deposit is at the axial seal pin between two adjacent blade platforms [1]. To prevent ingestion of the hot main gas flow between blade platforms, high pressure air is supplied from beneath the blade platform as illustrated in Figure 1.1. The axial seal pin performs two functions: it reduces leakage of high pressure air into the mainstream gas flow; and it acts as a mobile vibration damper for the blades. When rust particles deposit around the seal pin, they can prevent movement of the pin so that adjacent blade platforms are in rigid contact with one another. The inability of the pin to move inhibits its vibration damping capability, resulting in blade failure due to fatigue from cyclic vibration stresses. One such incident occurred in a gas turbine at the Payne Creek, Florida power generating facility [1].

This thesis presents an experimental study to determine various effects of rust deposition on leakage flow through the axial seal pin area. The primary objective of this study is to understand the parameters controlling particle deposition at the axial seal pin. Ultimately an improved understanding of deposition in this region should guide design changes to eliminate the problem of vibration-induced failure. Results from an initial particle characterization study are presented and show the effects of engine-representative temperatures and centrifugal accelerations on rust particles. A static test facility was designed to flow clean and particle-laden air through the axial seal pin between two first row blades. Additionally, a rotating test facility was designed to perform similar flow and particle injection experiments on a smaller test coupon representative of the engine hardware. Flow blockage and particle deposition results from both test facilities are discussed.

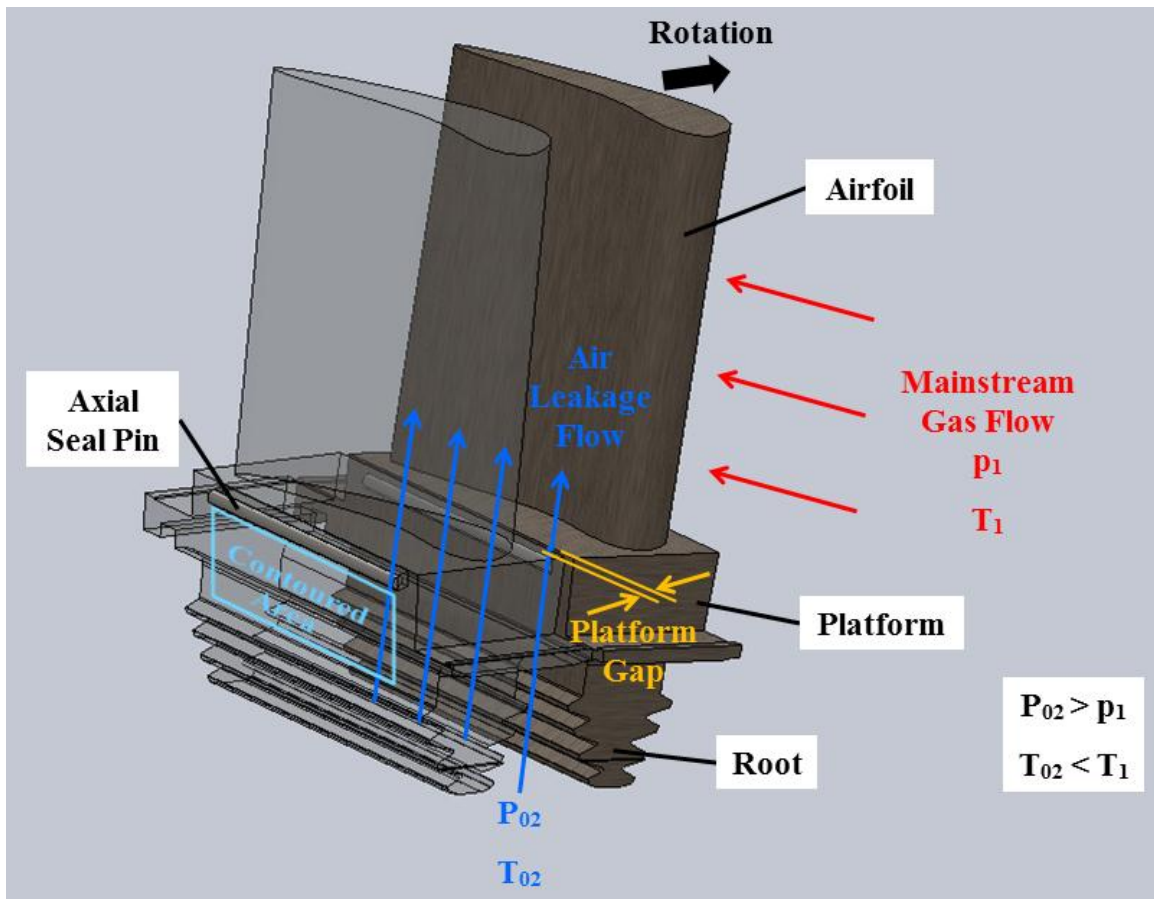


Figure 1.1. Two adjacent turbine blades with air leakage at the axial seal pin.

## **Chapter 2. RELEVANT PAST STUDIES**

Problems common to both aerospace and land-based gas turbines include erosion and deposition due to particle ingestion, which have been the subject of many previous studies. In propulsion turbines, where filtration is impractical due to size and weight restrictions, sand and volcanic ash have caused severe engine component wear and engine shutdowns while flying through particulate-laden clouds from volcanic eruptions [2-4]. Land-based engines face problems such as cooling hole blockage due to ingestion of particles from piping, casings, and rotor hardware and combustion of heavy oils and synthetic fuels. While land-based engines have large filters upstream of the air intake, test results show that particles with sizes sufficient to block cooling holes still enter the engine internal air system [5]. This chapter provides some general background on mechanisms of deposition as well as a review of past deposition studies. Finally, the uniqueness of the present study is discussed.

### **2.1 Mechanisms for Particle Delivery and Deposition**

Since the focus of this study is on particle deposition, it is important to understand what mechanisms cause particles to approach and adhere to a surface. For particles larger than 1  $\mu\text{m}$  moving as a disperse phase in a continuous medium, inertial effects are the dominant deposition mechanism. As fluid velocity or particle size is increased, particles are less responsive to bends in the flow streamlines, resulting in impaction with surfaces. Whether or not a particle adheres to a surface depends in part on the particle size and velocity. Van der Waals forces become important near a surface and drive particle adhesion. These forces are due to instantaneous dipoles created from shifts in the electron clouds around atomic nuclei, and their attractive strength is measured in terms of interaction energy. Very near a surface, the interaction energy becomes infinite, resulting in deposition of small particles that come within one particle radius of the surface [6]. Larger particles or particles with a high velocity may rebound if their inertia exceeds the attractive van der Waals force. Particles investigated in this study were larger than 1  $\mu\text{m}$ , so inertial effects were anticipated to dominate particle behavior.

### **2.2 Previous Gas Turbine Deposition Studies**

Early studies of particle behavior in gas turbines focused on the effects of particles in the main gas flow path with initial motivation provided by engine failures during encounters with

volcanic ash clouds. A series of three studies by Dunn et al. and Batcho et al. investigated effects of volcanic ash ingestion in a series of full-scale engine tests [7-9]. Two turbofan engines were cycled through their operational ranges while subjected to a continuous stream of ash particles similar to Mt. St. Helens ash. All of these studies were primarily focused on erosion and noted significant performance deterioration due to compressor blade erosion. Various particle concentrations and compositions were tested, but very little deposition was observed on hot-section surfaces. The lack of deposition was because the turbine inlet temperatures, which were between 870°C and 890°C, were too low to result in melting and subsequent deposition of the ash material. An interesting finding was that ingested particles underwent substantial erosion and breakage, decreasing in average diameter from 38  $\mu\text{m}$  at the compressor inlet to 6  $\mu\text{m}$  at the compressor by-pass [9]. Particle samples taken downstream of the by-pass at compressor stage 16 did not exhibit further decrease in particle size, which indicated most particle erosion occurred in the fan and early compressor stages.

The scale and expense of full-scale engine tests has resulted in the development of representative engine test sections such as the hot section test system (HSTS) used by Kim et al. [10] and Weaver et al. [11] to investigate deposition of volcanic ash and soil particles. The HSTS consisted of a particle feeder, combustor, and nozzle guide vanes. For volcanic ash particles, Kim et al. [10] reported deposition occurring above a threshold turbine inlet temperature between 1066°C and 1121°C. Similarly, for soil composed of quartz, red art clay, and feldspar, Weaver et al. [11] reported deposition occurring above a threshold combustor exit temperature of 1149°C. Both studies observed no deposition below their respective threshold gas temperatures. Weaver et al. [11] also found a threshold surface temperature of 816°C below which no particles were deposited. Thus, surface temperatures near the particle melting temperature have been established as a key factor in determining deposition.

Wenglarz et al. [12] studied ash deposits from coal water fuels on two sections of generic specimens downstream of a combustor. In their experiments, the gas temperature at the first section was varied between 980°C and 1100°C, and specimen surface temperatures were varied from about 100°C below up to the gas temperature. The study found that at a first section inlet gas temperature of 1100°C, increasing the specimen temperature yielded an increase in deposition, yet no correlation between deposition and surface temperature was observed for the lower inlet gas temperature. This finding again suggests the existence of a threshold gas



temperature above which particles soften, thus promoting deposition. The authors noted a reported ash fusion temperature of 1170°C from the ASTM cone test may overestimate the particle softening temperature due to the testing method. In any case, both the gas and specimen temperatures reported in this study were in the neighborhood of the particle softening temperature.

To compare characteristics of deposition formed over several hours in an experimental setting with deposition formed on actual engine components over thousands of operating hours, Jensen et al. [13] created an accelerated deposition test facility. Their facility flowed particle-laden gas at temperatures up to 1200°C over test coupons representative of engine blade and vane surfaces. Through a detailed chemical and structural analysis of deposits, Jensen et al. [13] concluded their facility was able to create engine-representative depositions by matching total particle mass loading to typical engine conditions. Their results also showed the existence of a threshold deposition temperature between 900°C and 1100°C, but the authors cautioned this result may have been specific to their test facility since actual turbine components experience deposits with gas temperatures less than 900°C.

In 2006, Hamed et al. [14] wrote a thorough review of past studies on erosion and deposition, which includes some of those previously mentioned. Their review covers the effects of temperature, particle size, particle composition, surface composition, impact velocity and angle, and coefficient of restitution. Also, a discussion of deposition mechanisms is provided. All of the studies covered in their review focused on particle effects in the compressor or turbine main gas path.

Investigations of particle deposition in cooling flow paths are of particular relevance to the present study. Walsh et al. [15] performed an early study of particle deposition in internal film-cooling passages and developed a method for characterizing deposition in terms of flow blockage. They injected masses of sand into flow through a test coupon and measured blockage in terms of a reduction in dimensionless flow parameter at a particular pressure ratio. Tests were performed on cylindrical test coupons representative of film cooling holes on the leading edge of an airfoil. Several interesting results were found in these tests. After injecting a lump mass of sand, a step decrease in flow parameter and a step increase in pressure ratio were observed. Blockages up to 11% reduction in flow parameter (RFP) were measured, and blockage increased for heated tests as compared with ambient temperature tests. For engine-representative coolant

and metal temperatures, blockage was shown to increase strongly with metal temperature, and a dramatic increase in blockage was observed when metal temperature increased above about 1000°C. Blockage also decreased with increasing pressure ratio and increased with particle diameter. Finally, blockage increased with the mass of sand injected for all pressure ratios.

Following the method by Walsh et al. [15], Land et al. [16] and Cardwell et al. [17] investigated sand deposition and blockage in double-wall geometries with impingement- and film-cooling holes similar to those found in the blade outer air seal and combustor liner. Their double-wall test coupon had one wall of impingement-cooling holes angled at 90° to the surface followed by a second wall of film-cooling holes set at a 30° angle to the surface. Sand particles injected into the coupons were composed primarily of quartz ( $\text{SiO}_2$ ) and aluminum oxide ( $\text{Al}_2\text{O}_3$ ) with traces of other metal oxide compounds.

Land et al. [16] studied the effects of injected sand quantity, sand particle size, pressure ratio, alignment of impingement- and film-cooling holes, and wall spacing. They measured blockages ranging from 3% to 80% RFP. Blockage was shown to increase with the mass of sand injected and with sand particle size, particularly for particles larger than 150  $\mu\text{m}$ . An increase in blockage with pressure ratio was observed for pressure ratios of 1.02 to 1.1 and was attributed to particles depositing in the impingement-cooling holes. Blockage decreased as pressure ratio was increased from 1.1 to 1.7 because higher velocities carried the particles through the impingement holes and resulted in particle breakage between the two walls. The resulting smaller particles were more likely to flow through the film-cooling holes, thus reducing blockage. Finally, an optimal wall spacing that minimized blockage was determined.

Cardwell et al. [17] investigated effects of parameters including pressure ratio, coolant and surface temperature, hole alignment, and mass of injected sand particles. Similar to the results in [16], they found blockage increased with pressure ratio. The increase in blockage was attributed to increasingly ballistic particle behavior as pressure ratio, and, by extension, velocity in the holes was increased. Ballistic particles unable to follow turning of the flow were more likely to impact the surface, thus increasing the probability of deposition and blockage. Blockage was also found to increase most strongly with the coupon surface temperature, with the most notable increase in blockage occurring when the metal temperature was increased from 871°C to 982°C. This metal temperature is comparable with the threshold temperatures noted in other studies [10-13]. Cardwell et al. [17] also noted coupons with unaligned impingement- and

film-cooling holes experienced less blockage due to the benefit of particle breakage within the coupon.

Several previous experimental and computational studies have focused on methods for removing particulates from coolant flow such as cyclone filtration. Schneider et al. [18] studied cyclone particle separation in flow through a representative rotating turbine disk cooling system with a blade root. Moving from the rotor disk cavity inlet to the blade root, they observed a decrease in size of deposited particles by a factor of 10, which was attributed to a decrease in cyclone collection efficiency for smaller particle sizes and an increase in the number of smaller particles due to breakage. Friedlander [6] notes that particle collection efficiency reaches a minimum for the size range of 0.1 to 1  $\mu\text{m}$ , the intermediate region where neither diffusion nor inertial effects dominate particle motion. For the case of a cyclone separator, a later study by Schneider et al. [19] found the particle collection efficiency decreased substantially for particles less than 10  $\mu\text{m}$  diameter, thus illustrating the challenge of mechanically separating small particles. Through comparisons of computational and experimental particle collection, Schneider et al. [20] showed that particle shape may significantly influence drag forces on particles. They found a correlation proposed by Haider and Levenspiel [21] was necessary to account for the non-spherical shape of their test particles.

### **2.3 Uniqueness of the Present Study**

Several studies of sand-laden flow through internal flow geometries have given insight into blockage of coolant passages and methods of particle collection. To the author's knowledge, no previous studies have investigated rust particle ingestion and deposition. Since rust, which is mostly iron oxide, differs considerably from sand, comprised mainly of silicon dioxide, effects of rust particle ingestion may differ from those previously reported for sand. For example, the density of rust is about 5200  $\text{kg/m}^3$ , which is nearly twice that of sand, about 2650  $\text{kg/m}^3$ . This density difference may cause rust particles of a given size to exhibit more inertial behavior than similarly sized sand particles. In addition, rust particles are softer than sand and are therefore more easily crushed, which could influence particle behavior on impact with a solid surface.

Most internal flow geometries for which sand blockage was studied had minimum flow areas in the shape of a cylindrical channel. In contrast, the present study investigates rust particle deposition at the axial seal pin between two blades, which has a comparatively smaller flow area

created by surface roughness at the locations of seal pin-blade platform contact. This study provides opportunity to further investigate blockage trends observed in several studies following the method in [15] to determine their dependence on geometry. Finally, the inclusion of rotation yielding engine-representative centrifugal acceleration makes possible the investigation of the effects of centrifugal forces on flow and particle deposition.

## **Chapter 3. EXPERIMENTAL FACILITY AND METHODOLOGY**

The first three sections of this chapter describe the particle characterization study that was performed in preparation for simulating engine-representative particle deposition in the laboratory. Various particle mixtures were created and compared with particle samples taken from field-run gas turbines. Basic tests were also performed to determine the importance of engine conditions including elevated temperature and centrifugal acceleration.

The latter sections of this chapter describe two test facilities that were designed for rust injection in engine hardware and two hardware-representative test coupons. A static test facility was designed to investigate the flow behavior and particle deposition at the axial seal pin between two full-scale gas turbine blades. A smaller-scale rotating test facility was designed to investigate the effects of rotation on flow and particle deposition in two test coupons similar to the axial seal pin flow area. Provided in this section are descriptions of the test facilities, engine hardware, representative test coupons, and their flow areas along with a derivation of the dimensional flow functions used in the data analysis. Flow through clean engine hardware and the test coupons is compared with a one-dimensional prediction, and a correction factor to the prediction is provided. The procedures for flow and particle injection tests are outlined, and the test matrices are presented. Finally, an estimation of parameter uncertainty is provided. Results from the particle characterization and particle injection tests are discussed in Chapters 4 and 5.

### **3.1 Creation of Representative Particle Samples**

The sponsor obtained many samples of particle deposits from the rotor air cooler piping and the engine internal air system of two turbines at the Payne Creek power generating facility, namely turbines CT1 and CT2 [1]. The samples were composed of metal oxide compounds. Excluding oxygen, of the elements present in the samples, the six most commonly found in all of the samples were aluminum, calcium, iron, zinc, silicon, and chromium. Mass normalized elemental compositions for the averages of all samples taken in each turbine are given in Table 3.1. Also shown in Table 3.1 are five mixtures of metal oxide compounds made in the laboratory to represent the range of particle compositions found in CT1 and CT2.

**Table 3.1. Elemental Compositions of Turbine Samples and Representative Laboratory Particle Mixtures**

Mass %	Al	Ca	Fe	Zn	Si	Cr
<b>Payne Creek CT1</b>	5.12	5.39	63.2	11.5	14.1	0.67
<b>Payne Creek CT2</b>	1.42	7.29	77.8	10.9	0.55	2.11
<b>Mixture 1</b>	3.06	6.57	72.6	11.3	6.46	0.00
<b>Mixture 2</b>	3.01	6.47	71.5	11.2	6.36	1.49
<b>Mixture 3</b>	30.7	25.9	21.0	18.2	1.99	2.27
<b>Mixture 4</b>	3.17	25.6	28.7	24.5	14.3	3.74
<b>Mixture 5</b>	0.93	0.32	86.3	10.2	1.02	1.26

Mixture 5 was an average of the elemental compositions from samples taken nearest to the row one blades in CT1 and CT2 and was most representative of particles deposited near the seal pin. This mixture was composed primarily of red iron oxide and zinc oxide and was used to perform the particle injection tests in this study. Shown in Table 3.2, commercial powders were purchased and mixed together to produce the desired composition. The melting points of the metal oxide compounds were all above 1500°C.

**Table 3.2. Metal Oxide Mixture 5 Composition**

Manufacturer	Product	Listed Size (µm)	Mass %	Melting Point (°C)
Sigma Aldrich	Red Iron (III) Oxide, Fe <sub>2</sub> O <sub>3</sub>	powder	86.3	1538
Aldrich	Zinc Oxide, ZnO	powder	10.2	1975
Sigma Aldrich	Chromium (III) Oxide, Cr <sub>2</sub> O <sub>3</sub>	50	1.26	2435
Aldrich	Silicon Dioxide, SiO <sub>2</sub>	< 78	1.02	1610
Aldrich	Aluminum Oxide Powder, Al <sub>2</sub> O <sub>3</sub>	< 10	0.93	2040
Sigma Aldrich	Calcium Oxide, CaO	powder	0.32	2614

The particle size distribution for a sample from CT1 had a median diameter of 19 µm and included particles ranging in size from submicron to 200 µm. The mixture 5 particle size distribution was measured from a dry sample by laser diffraction and was found to have a median diameter of 20 µm with particles ranging from submicron to about 1000 µm. The dry laser diffraction technique was also used to characterize the particle sizes of field-run engine

particle samples. From Figure 3.1, it is evident that mixture 5 spanned the size distribution of particles found in CT1 and also contained some larger particles. The percent of total particles shown is defined as the number of particles within a particular size range divided by the total number of particles counted. As noted in previous literature, the laser diffraction method involves some preprocessing that breaks up large conglomerations of particles and thus may give a somewhat smaller size distribution than what would have been observed for the unprocessed particles [15].

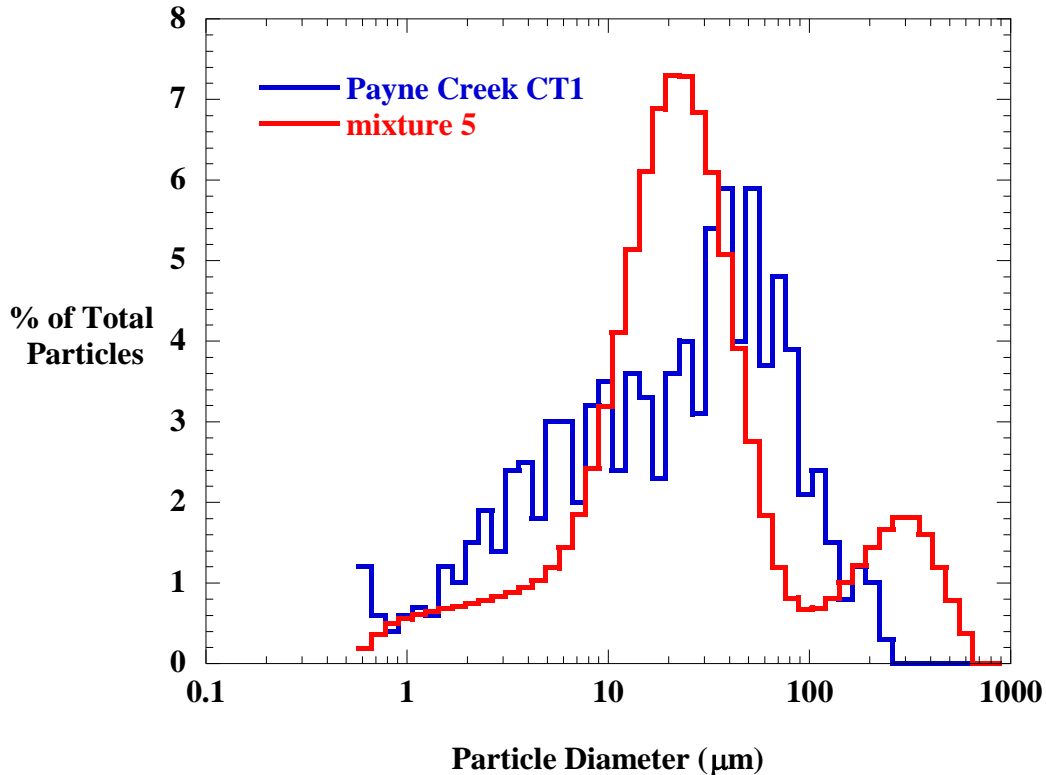


**Figure 3.1. The mixture 5 size distribution included the range of particle sizes found in Payne Creek CT1.**

Additional particle composition analysis was performed on samples taken from a field-run blade. As depicted in Figure 3.2, samples were taken from the root and from the contoured area between the root and the seal pin slot and are subsequently referred to as *root* and *contour*, respectively. Shown in Table 3.3 are the elemental compositions of the field-run blade samples, which were similar to the Payne Creek turbine samples in that they contained primarily iron and zinc. Notable differences are the presence of sulfur and nickel in the root and contour samples.

These elements were found in some of the Payne Creek samples but were not among the six most commonly present elements.

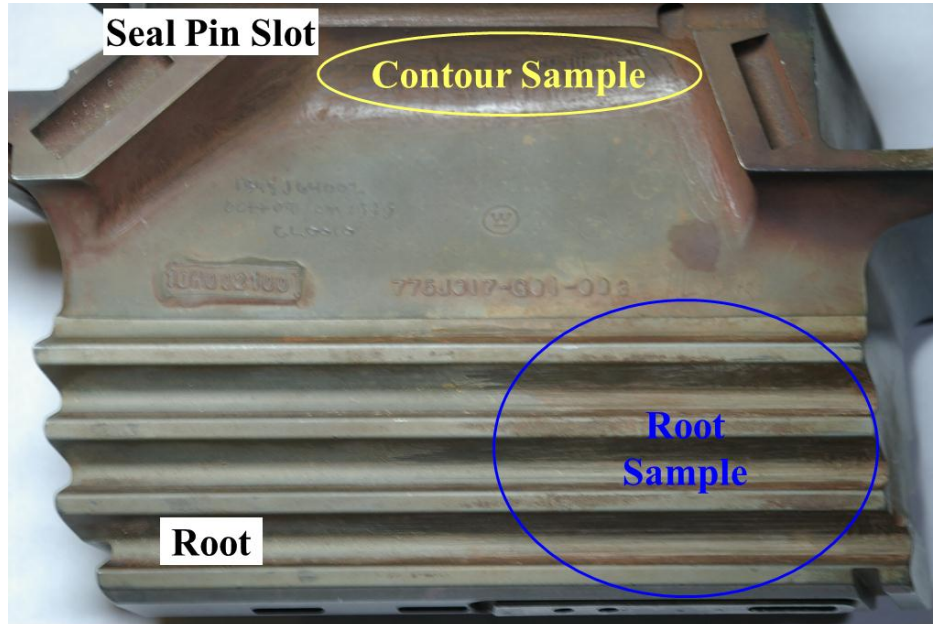


Figure 3.2. Particle sample locations on the field-run blade.

Table 3.3. Elemental Compositions of Samples from Field-Run Blade

Mass %	Al	Ca	Cr	Fe	K	Ni	S	Si	Zn
<b>Root</b>	5.69	3.75	2.65	45.9	1.68	5.05	18.7	10.2	6.49
<b>Contour</b>	1.62	2.65	1.90	38.7	0.56	9.60	4.59	3.76	36.6

### 3.2 Particle Heating Tests and Procedures

A test matrix, shown in Table 3.4, was created to determine the effects of heating on particle samples including sand, various metal oxide compounds, and previously discussed metal oxide mixtures representative of samples from field-run turbines. Temperatures selected for these tests ranged from 538°C to 1093°C in order to approximately span the temperature range from the row one engine coolant at 478°C to the row one blade root at 850°C [22,23]. Particles were placed in a kiln and brought to the target temperature at a rate of 222°C/hr. The exposure time was measured from the time at which the kiln reached the target temperature.



**Table 3.4. Particle Heating Test Matrix**

Sample Composition	Kiln Temperature (°C)	Exposure Time (min.)
100% Sand	1010	0
100% Black Fe <sub>2</sub> O <sub>3</sub>	538 - 1093	0 - 30
100% Red Fe <sub>2</sub> O <sub>3</sub>	538 - 1052	0 - 30
100% Al <sub>2</sub> O <sub>3</sub>	816	0
50% Red Fe <sub>2</sub> O <sub>3</sub> , 50% Black Fe <sub>2</sub> O <sub>3</sub>	538 - 1093	30
90% Red Fe <sub>2</sub> O <sub>3</sub> , 10% Al <sub>2</sub> O <sub>3</sub>	538 - 1093	0 - 30
90% Black Fe <sub>2</sub> O <sub>3</sub> , 10% Al <sub>2</sub> O <sub>3</sub>	1052	0
45% Red Fe <sub>2</sub> O <sub>3</sub> , 45% Black Fe <sub>2</sub> O <sub>3</sub> , 10% Al <sub>2</sub> O <sub>3</sub>	1052	0
Mixture 1	816 - 1093	0 - 120
Mixture 2	850	0 - 120
Mixture 3		
Mixture 4		
Mixture 5		

While heating in the kiln, particles were placed on ceramic blocks and exposed to the atmosphere for prolonged periods, raising concern over particle contamination. To check for sample contamination, unheated and heated samples were analyzed using an environmental scanning electron microscope (ESEM) and the energy dispersive X-ray spectroscopy (EDS) technique. Results shown in Figure 3.3 show the same elements were present before and after heating, which indicates the heating process did not contaminate the samples.

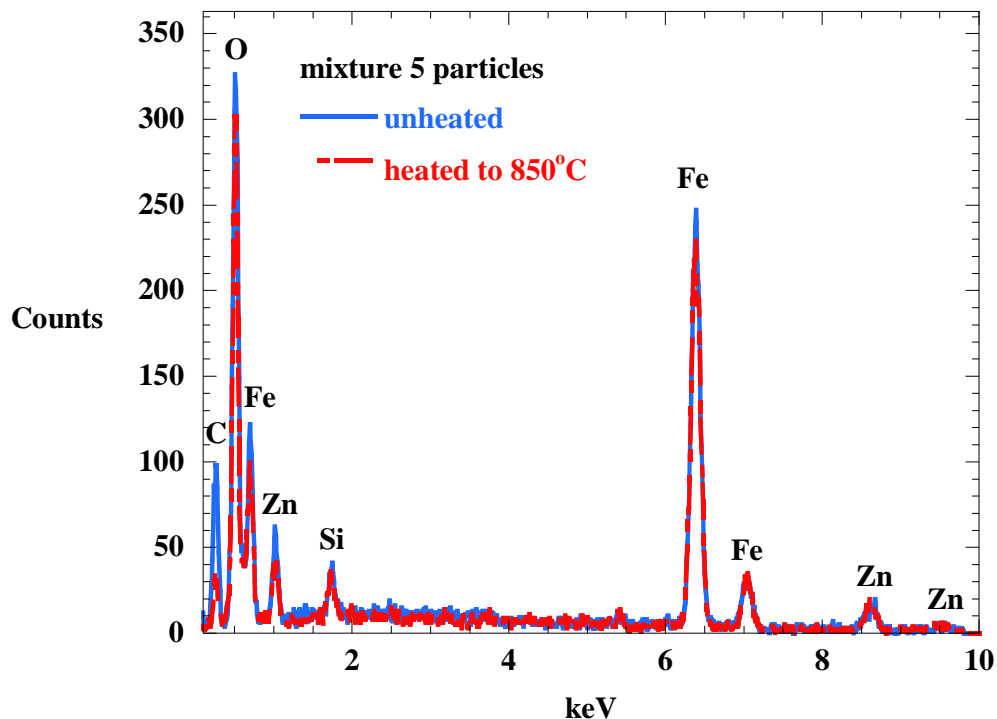


**Figure 3.3. Comparison of particle composition before and after heating in the kiln.**

Results for the particle characterization study included both visual observation and particle size analysis. Sample appearance observations were made both at elevated temperatures and subsequently after samples cooled to ambient conditions. From a comparison of Figure 3.4 and Figure 3.5, it can be observed that conglomeration and color changes occurring at elevated temperatures remained after the samples cooled back to room temperature. The persistence of these appearance changes after samples cooled indicated that chemical and physical changes occurring in the samples during heating were permanent.

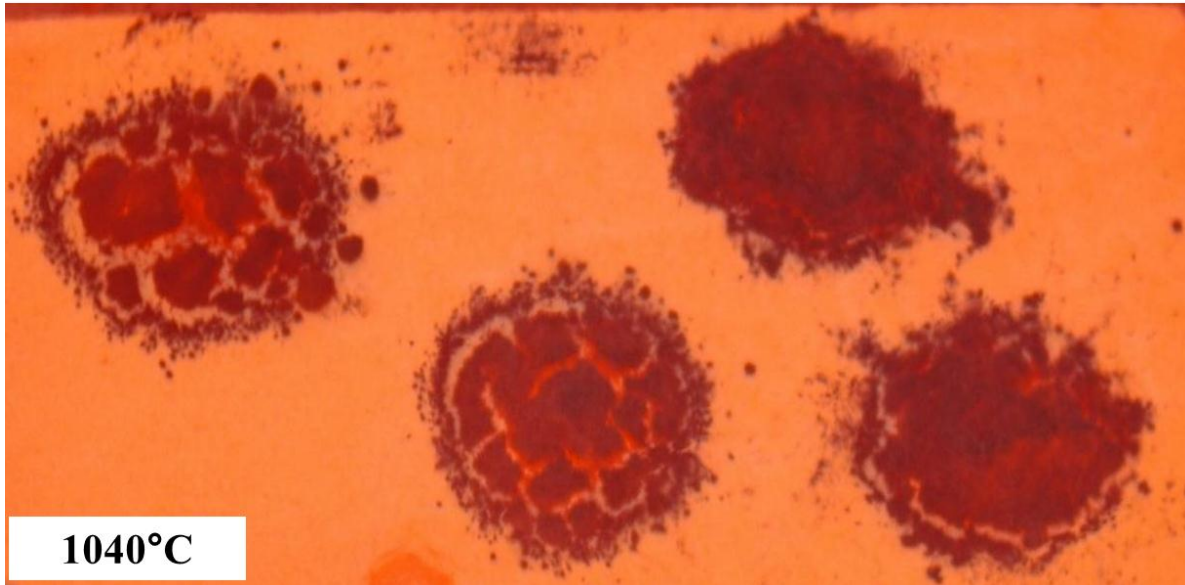


**Figure 3.4. Metal oxide particles shown while being heated in the kiln.**

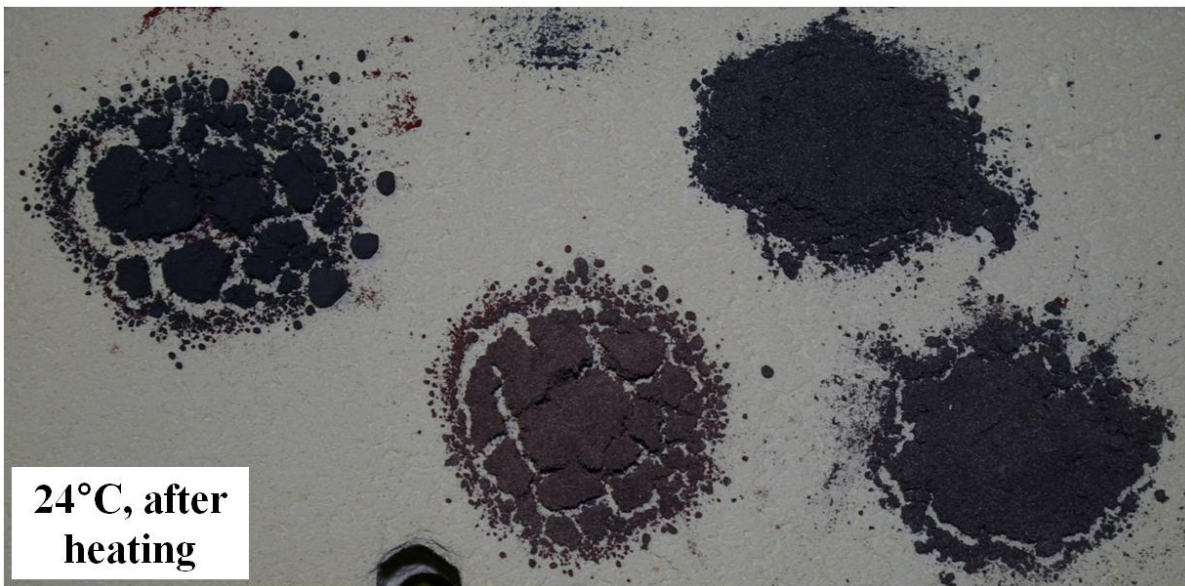


**Figure 3.5. Metal oxide particles shown after being heated in the kiln and cooling to room temperature (same samples as in Figure 3.4).**

### **3.3 Particle Centrifuge Tests and Procedures**

Shown in Table 3.5, a test matrix was created to investigate the effects of engine-representative centrifugal acceleration on particle samples. For the gas turbine considered, the first row platform radius, which is just above the axial seal pin slot, is 856 mm. Using this radius and the base load engine speed of 3600 rpm, the engine centrifugal acceleration was calculated using Equation 3.1 to be 12,400 times gravitational acceleration. The centrifugal acceleration in

rotating tests was defined relative to the engine by the parameter  $\Omega$ , defined in Equation 3.2, where  $a_{c,e}$  represents the engine centrifugal acceleration at 3600 rpm. Centrifugal accelerations selected for testing were 12,100 and 75,500 times gravitational acceleration, which correspond respectively with  $\Omega = 1$  and  $\Omega = 6.1$ . Samples of both pure red iron oxide and mixture 5 particles were included in the test matrix to check for any effects from the additional trace metal oxide compounds present in mixture 5. Finally, unheated and previously heated samples were included to check for any combined effects from heating and centrifuging.

**Table 3.5. Particle Centrifuging Test Matrix**

Sample	$\Omega$	$m_{\text{rust}}$ (g)	Prior Heat Treatment
100% $\text{Fe}_2\text{O}_3$	1	10	none, 150°C for 4 hr.
Mixture 5	1 – 6.1	5 - 30	none, 850°C for 0 - 120 min.

$$a_c = r \cdot \omega^2 \quad (3.1)$$

$$\Omega = \frac{a_c}{a_{c,e}} \quad (3.2)$$

Particle samples were spun at ambient temperature in a Beckman Coulter Avanti J-25 centrifuge using the JA-25.50 rotor. Capped clear plastic tubes, as shown in Figure 3.6, were used to contain the particles and fit into the centrifuge rotor at an angle 34° from the axis of rotation. The outer radius of a tube from the axis of rotation was 108 mm, so rotating speeds of 10,000 and 25,000 rpm were required to generate the relative centrifugal accelerations listed in Table 3.5. All centrifuged samples were spun for 20 minutes.

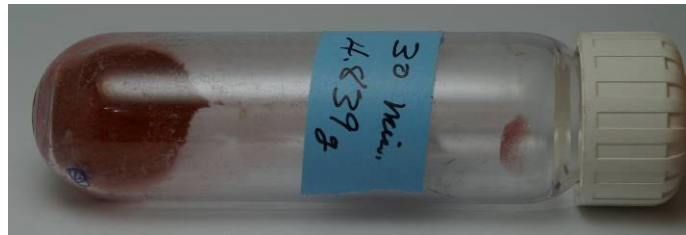


**Figure 3.6. Centrifuge tube containing a particle sample.**

### 3.4 Test Facilities

Two test facilities were used in this study, one static and one rotating. Shown schematically in Figure 3.7, the static test facility was designed to flow compressed air through engine hardware at laboratory ambient temperatures. This test facility also provided for injecting rust particles into the air upstream of the engine hardware. Main components of the static test facility included a compressed air supply, laminar flow element, upstream and downstream test chambers containing the engine hardware, a gravity-feed particle injection system, and upstream and downstream filters.

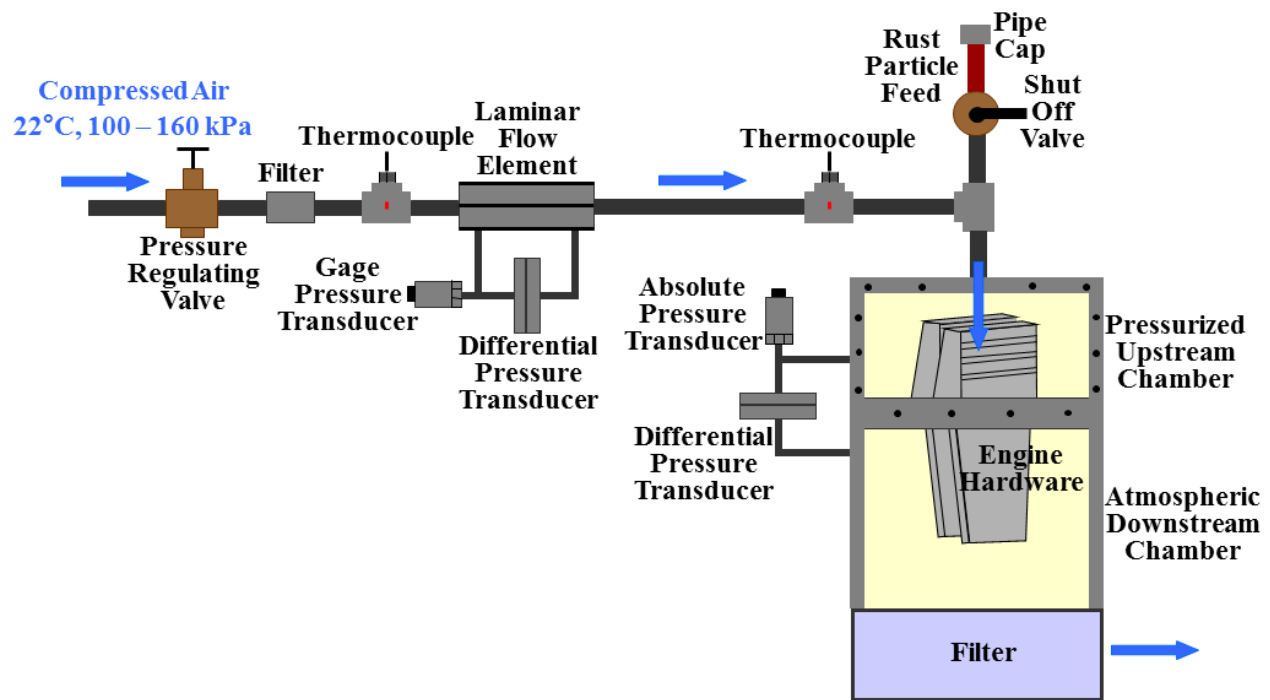


**Figure 3.7. A schematic of the static test facility used for rust injection studies.**

Compressed air from a remote compressor was supplied to the static test facility at approximately 410 kPa gage and 22°C. At the inlet to the test facility, a pressure regulating valve was used to set the upstream air pressure. A filter was installed just downstream of the valve to prevent dirt from entering the downstream instrumentation and engine hardware. A laminar flow element (LFE) with a maximum flow rate capacity of 750 cm<sup>3</sup>/s (for air at standard temperature and pressure of 21°C and 101 kPa, respectively) was used to measure the volume flow rate of air through the supply pipe. The flow rate required for the experiment varied from 60 cm<sup>3</sup>/s to 400 cm<sup>3</sup>/s at standard conditions. At least 10 pipe diameters of straight pipe length

were provided directly upstream and downstream of the LFE in accordance with the LFE manual. Gage pressure was measured at the LFE inlet, and temperature was measured upstream of the LFE with an E-type thermocouple inserted into the air supply piping through a tee fitting. In conjunction with the measured atmospheric pressure, these measurements were used to calculate the air density, which was multiplied by the actual volume flow rate to obtain the mass flow rate through the engine hardware.

Compressed air entered the top of the upstream chamber through a tee fitting. Also connected to the tee fitting and directly above the upstream test chamber was the particle feed supply. This supply consisted of an approximately 20 cm-long pipe sealed at the top with a pipe cap and connected at the bottom to a ball valve. The sealed cap was removed to load particles into the pipe and then subsequently replaced. When the valve was opened, particles were released into the flow due to gravity with no additional air leakage. Downstream of the tee fitting, air flowed into the upstream chamber, which as shown in Table 3.6, acted as a plenum due to its large cross-sectional area relative to the estimated seal pin flow area. Thus, the absolute pressure transducer connected to the upstream chamber measured the upstream total air pressure. Just upstream of the chamber a second E-type thermocouple was used to measure the air temperature. This temperature in conjunction with the air mass flow rate and upstream total pressure was used to calculate the flow function. A differential pressure transducer measured the pressure drop across the seal pin flow area, which allowed the pressure ratio across the engine hardware to be calculated. Air passed through the engine hardware and the downstream chamber before being exhausted to the laboratory atmosphere through a minimum efficiency reporting value (MERV) 11 filter, which captured rust particles during blockage tests. The downstream chamber was at approximately atmospheric conditions for all tests performed.

**Table 3.6. Static Test Facility Cross-sectional Flow Areas**

<b>Component Cross Sectional Area</b>	<b>Area (mm<sup>2</sup>)</b>	<b>Area Ratio (A/A<sub>sp</sub>)</b>
Seal Pin Gap, A <sub>sp</sub>	2.80*	
Air Inlet Pipe	200	71
Upstream Chamber Plenum	61800	22000

\*based on assumed seal pin clearance

A model of the static test chamber is shown in Figure 3.8 with the front panel removed for clarity. The outside of the test chamber was constructed of 12.7 mm thick type 304 stainless steel with 12.7 mm thick polycarbonate front and rear panels. The panels were fastened together with bolts and sealed at their joints with clear room temperature vulcanizing (RTV) silicone. Referred to as the blade support, a 25 mm thick stainless steel block with was machined to fit around the platforms of two blades installed side-by-side as they would be in the engine rotor. Attached to the front of the blade support was a rigid bar (front bar) used to exert a compressive force on the blade platforms and gasket material in the horizontal direction. Polycarbonate clamps (side clamps) on either side of the blades were used to exert a compressive force on the blades and gasket material in the vertical direction. Normally only the front panel, front bar, and side clamps were removed for disassembly and cleaning of the blades and test chamber.

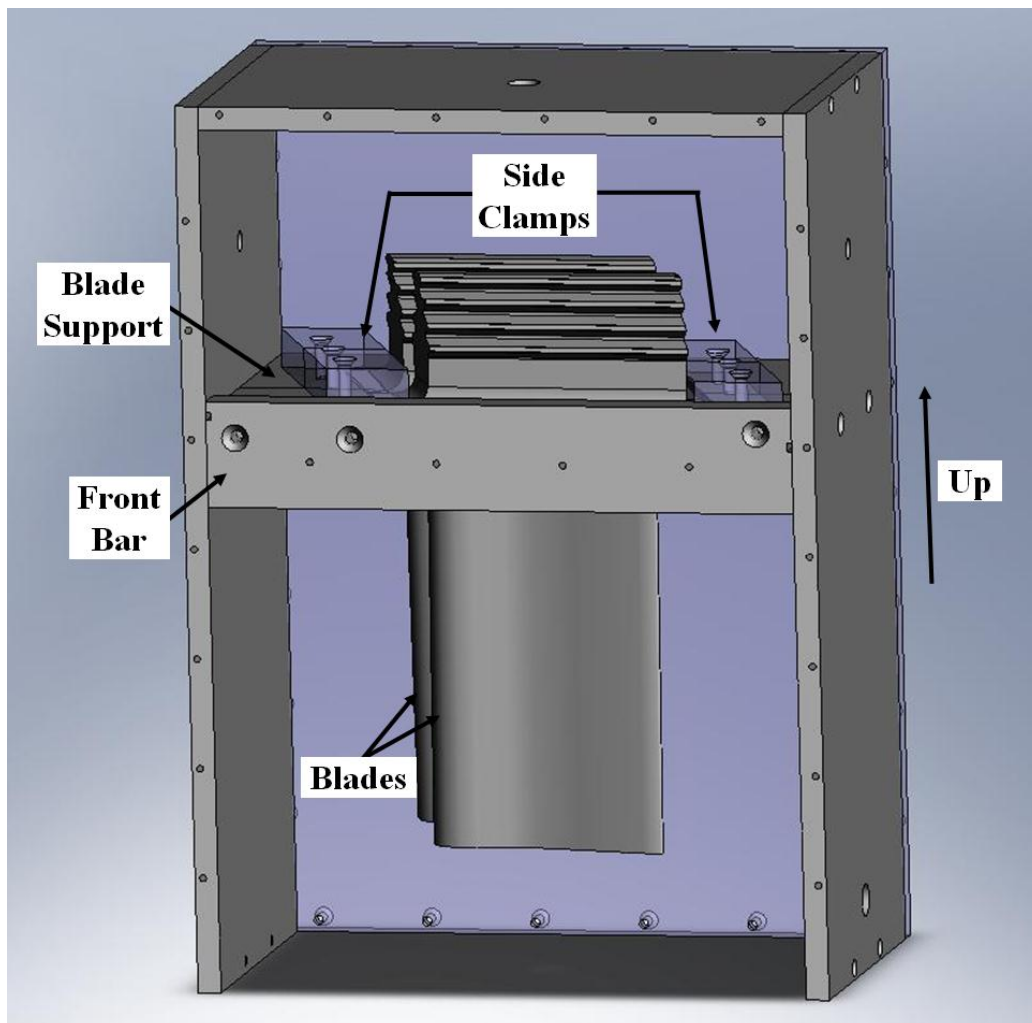


**Figure 3.8.** The static test chamber was designed to contain two turbine blades in a configuration representative of their positions in an engine rotor.

A constant effort was made to insure a hermetic seal throughout the upstream air supply piping, at the seams of the test chamber panels, and at the interface between the blade platforms and the blade support. RTV silicone was used to seal the front bar and the front panel. Leak checks at pipe unions, chamber panel seams, and the interface between the blades and blade support were regularly performed by brushing foamy soap and water solution and checking for bubbles. Further details of sealing at the interface between the blades and the blade support are provided in Section 3.5.

A second test facility, shown schematically in Figure 3.9, was designed to flow compressed air and rust particles through rotating test coupons representative of engine hardware. Components of the rotating test facility were similar to the static facility with the addition of a variable-speed centrifuge modified to spin the test coupons and a rotary coupling for the air supply. The rotating facility was capable of matching the centrifugal acceleration in a gas turbine, about 12,400 times gravitational acceleration. A comparison between the engine and rotating test facility is provided in Table 3.7, where the radii are for the distance to the radially-outermost face of the blade platform. In the rotating test facility, a speed of 10,300 rpm was required to match the engine centrifugal acceleration ( $\Omega = 1$ ).



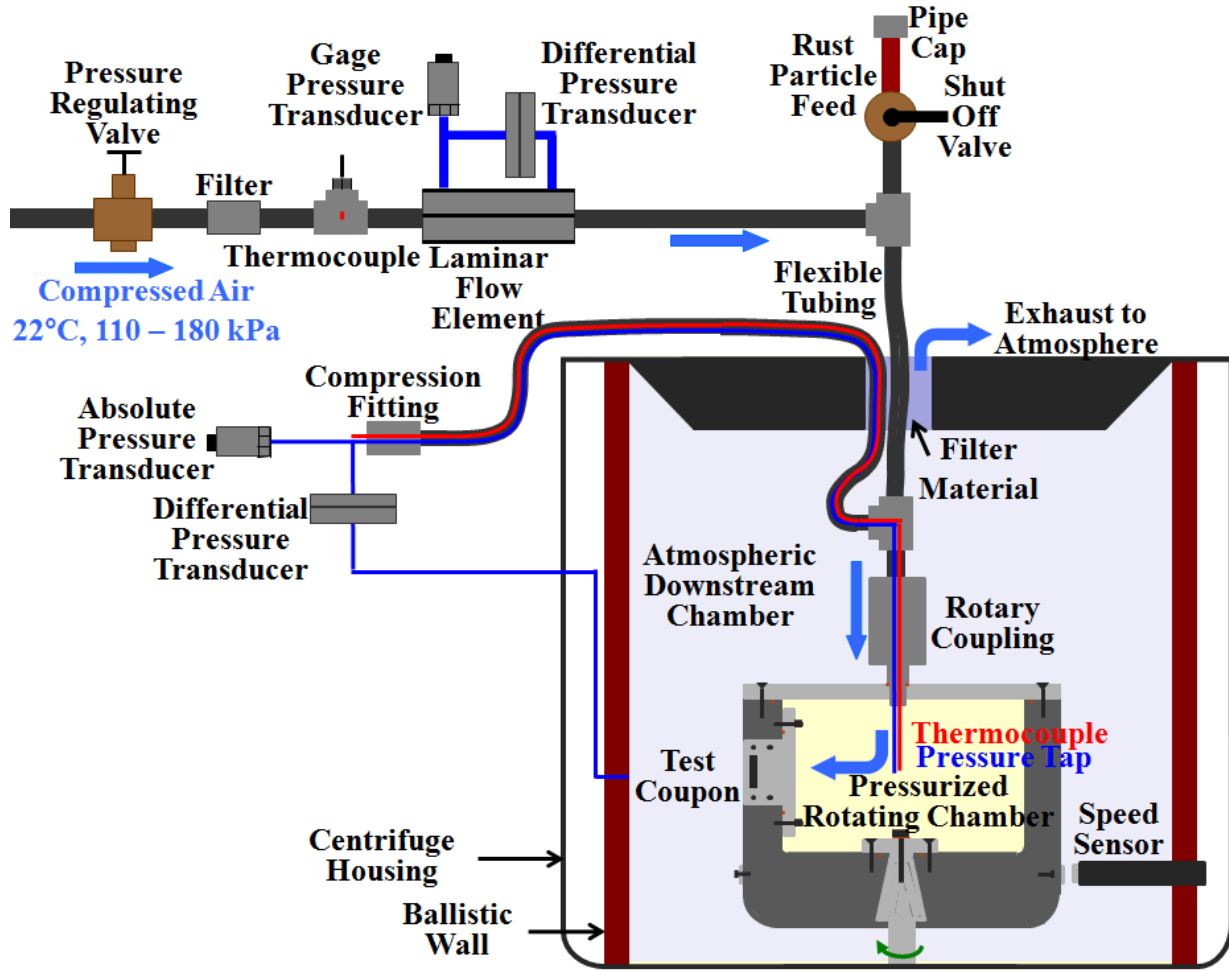


Figure 3.9. A schematic of the rotating test facility used for rust injection studies.

Table 3.7. Centrifugal Acceleration in Engine and Rotating Test Facility

	$\omega$ (rpm)	$r$ (mm)	$a_c$ (m/s <sup>2</sup> )	$\Omega$
Engine	3600	856	122000	1
Rotating Test Facility	500	105	287	0.002
	10300		122000	1

Only the pressurized chamber and test coupons rotated while all of the upstream piping and instrumentation remained static. A rotary coupling with a seal made of tungsten carbide and graphite was used to form a sealed union between the static components and the rotating chamber. The connection of the rotary coupling to the spinning container was varied depending on the rotating speed. A simplified installation was used for low speed tests, whereas for high speed tests some modifications were necessary to reduce vibration. For tests performed at  $\Omega =$

0.002, the rotary coupling was threaded into the chamber lid and sealed with an o-ring. The only support provided to the rotary coupling was that provided by the attached upstream piping. To reduce vibration for tests at  $\Omega = 1$ , an 83-mm long section of flexible tubing was used to connect between the rotary coupling and a modified chamber lid with a hose barb. The tube was made of Tygon material and had inner and outer diameters of 12.7 mm and 19 mm, respectively. Symmetric pinch-type tube clamps were used to connect the tubing to the rotary coupling and the hose barb on the lid. In this high speed configuration, the rotary coupling was rigidly mounted to the centrifuge lid such that it aligned with the axis of rotation of the spinning chamber.

Upstream of the rotary coupling, the air supply, particle feed system, and instrumentation were similar to the static test facility. The particle injection system consisted of a vertical 20 cm-long pipe with a sealed cap at the top and a ball valve at the bottom. The sealed pipe cap was later replaced with a second ball valve so particles could be more efficiently loaded into the feed pipe. Air and particles were initially combined in a tee fitting upstream of the rotary coupling. Later on for testing at  $\Omega = 1$ , the particle feed tube was extended inside the air supply pipe through the center of the rotary coupling, terminating inside the rotating chamber. This modification was necessary to prevent particles from damaging the mechanical seal in the rotary coupling and to more effectively deliver particles to the test coupons. A section of stainless steel tube with an outer diameter of 4.8 mm was used to extend the particle feed tube.

From the tee fitting for the air and particle supplies, air and particles passed through a 30 cm-long flexible nylon tube to the top of a second tee fitting, which was connected to the top of the rotary coupling. Through the side of the second tee fitting, two type-E thermocouples and two small stainless steel tubes for pressure measurement were inserted into the inside of the rotating chamber. The pressure measurement tubes and thermocouples were tied together with thread and bent at a right angle to pass through the center of the rotary coupling and the chamber lid without contacting rotating components. Upstream of the second tee fitting, the stainless steel tubes were connected to flexible tubing, which exited the pressurized piping system along with the thermocouples through a compression fitting. From this point the tubes were connected through a manifold to an absolute pressure transducer. As in the static test facility, the measured upstream total pressure was used in conjunction with the measured air mass flow rate and temperature to calculate the flow function. The use of flexible tubing for the air and particle supply pipe and the pressure taps was necessary to permit small horizontal displacement of the

rotary coupling during rotation. At  $\Omega = 1$ , excessive heating due to friction and the extension of the particle feed tube through the rotary coupling made it necessary to move the pressure taps and thermocouples inside the chamber further upstream. The pressure tap was moved to the tee fitting just above the rotary coupling, and the thermocouple at the inlet to the LFE was used as the upstream total temperature. Errors in the upstream total pressure measurement resulting from moving the pressure tap were determined to be negligible. The pressure drop through the upstream pipe nipple and rotary coupling was estimated to be about 0.1 in.  $H_2O$ , or about 0.04% of the differential pressure across the test coupons. Additionally, the dynamic pressure at the upstream measurement location was about 0.01% of the total pressure.

Inside the rotating chamber, a horizontal circular plate with curved vertical walls was installed to direct particles into the test coupons. Shown in Figure 3.10, two similar versions of the particle diffuser plate were created, one for low speed tests, and a second, more structurally robust version for high speed tests. As shown schematically in Figure 3.11, the bottom of the plate was at approximately the mid-height of the test coupons and extended from the center of the chamber out to the openings in the test coupons. Curved vertical walls 25 mm in height were attached to the top of the plate such that they directed particles into the openings in the test coupons. The top of the walls was just above the end of the extended particle feed tube to prevent particles from diffusing radially outward before reaching the parts.

To provide containment in the event of accidental liberation of rotating components, the rotating chamber was entirely contained inside the metal-encased centrifuge housing and a cylindrical ballistic shield made of 12.7 mm thick steel. A Hall effect sensor was mounted onto the ballistic shield to monitor the rotating speed. Also mounted flush with the inside of the ballistic shield were four downstream pressure taps, each spaced at  $90^\circ$  around the circumference and centered vertically with the test coupons. A differential pressure transducer was connected between these pressure taps and the upstream chamber pressure taps, and the differential pressure in conjunction with the upstream chamber pressure was used to calculate the pressure ratio across the test coupons. Since high rotating speeds generated a pressure gradient between these downstream pressure taps and the exits of the test coupons, a correction was applied when calculating the pressure ratio. Calculation details and nominal values for this correction are provided in Appendix B.

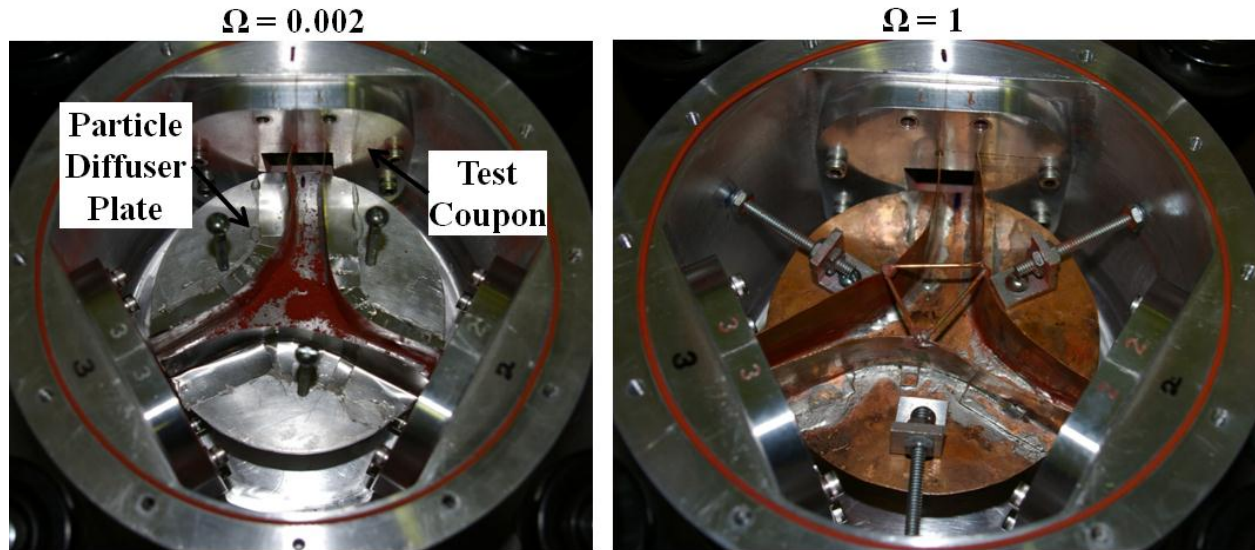


Figure 3.10. Top view of rotating chamber with lid removed.

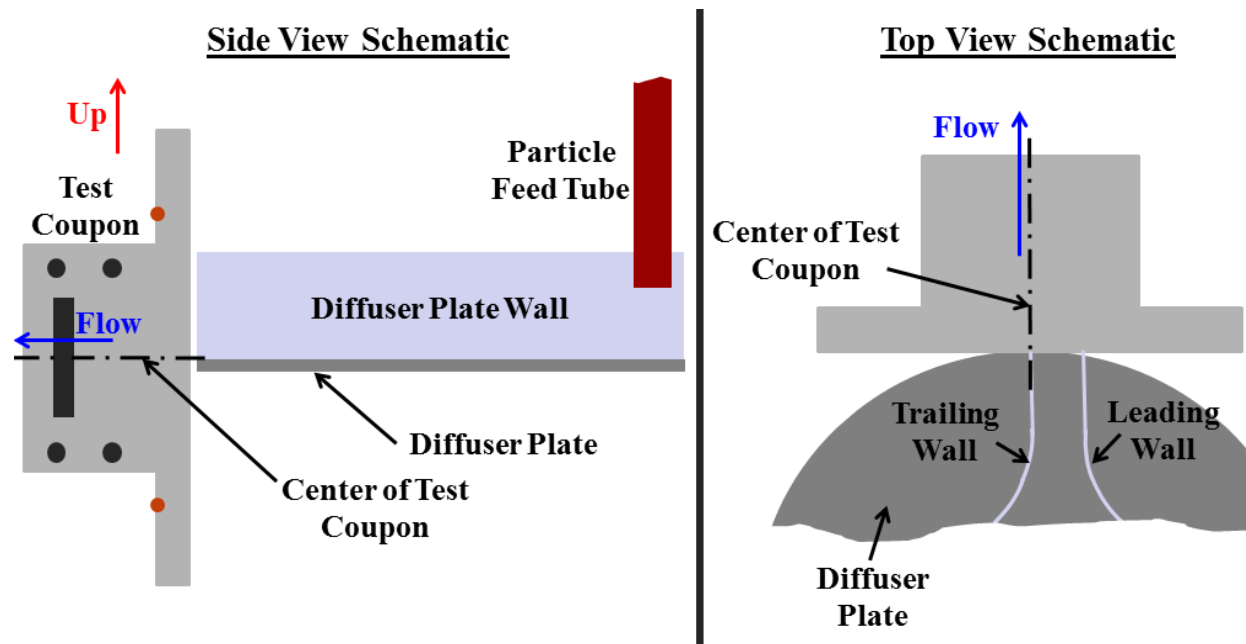


Figure 3.11. Particle diffuser plate position relative to test coupon.

As shown in Figure 3.10, the rotating chamber was designed to be symmetric about its axis of rotation with three ports through the side wall. To improve balance and increase testing efficiency, three identical test coupons were installed in these ports. Special care was taken to maintain symmetry during machining of the chamber so that dynamic balancing was unnecessary. The chamber, lid, and test coupons were all made of 7075 aluminum due to its machinability and high strength-to-weight ratio. O-ring seals were used at the interfaces of the

lid and test coupons with the chamber walls. Each set of three test coupons was made to close tolerances such that the masses of the test coupons in a given set were approximately equal.

Prior to flow testing, the test chamber was assembled with gasket material filling the simulated platform gaps in the test coupons. In this configuration, a pressure leak test showed the container was hermetically sealed. Periodic pressure leak tests were also performed on the rotary coupling under non-rotating conditions, and these tests showed the rotary coupling was also hermetically sealed. As in with the static test facility, leak checks with soap bubbles were periodically performed on upstream connectors and pipe fittings.

A Sorvall model RC2-B floor centrifuge was modified to provide the high-speed rotating drive and containment shroud for the rotating chamber. The centrifuge had a variable-speed drive with a maximum speed of 20,000 rpm. For the rotating test facility, the maximum rotating speed was about 10,300 rpm, corresponding with  $\Omega = 1$ . A hole was cut out in the centrifuge lid to permit the air and particle supply pipe and instrumentation to be connected to the rotating chamber and to provide an exhaust to the laboratory atmosphere. During particle injection tests, this hole was covered with fabric filter material to contain rust particles inside the centrifuge.

### **3.5 Description of Engine Hardware and Flow Area**

For the tests performed in the static test facility, two complete blades from the first row of a land-based gas turbine engine were used. Shown in Figure 3.12, the blades were identical in style, but one was new and the other was exposed to field service. Both blade platforms were in good condition with the exception of a small crack at the seal pin slot on the field service blade. This crack was sealed with silicone prior to testing. The platform style of the blades was similar to that of the failed blades in [1] and is referred to as the slotted design. Also used in this study was an axial seal pin, which measured 6.35 mm in diameter and 110 mm in length and was chamfered slightly on each end.

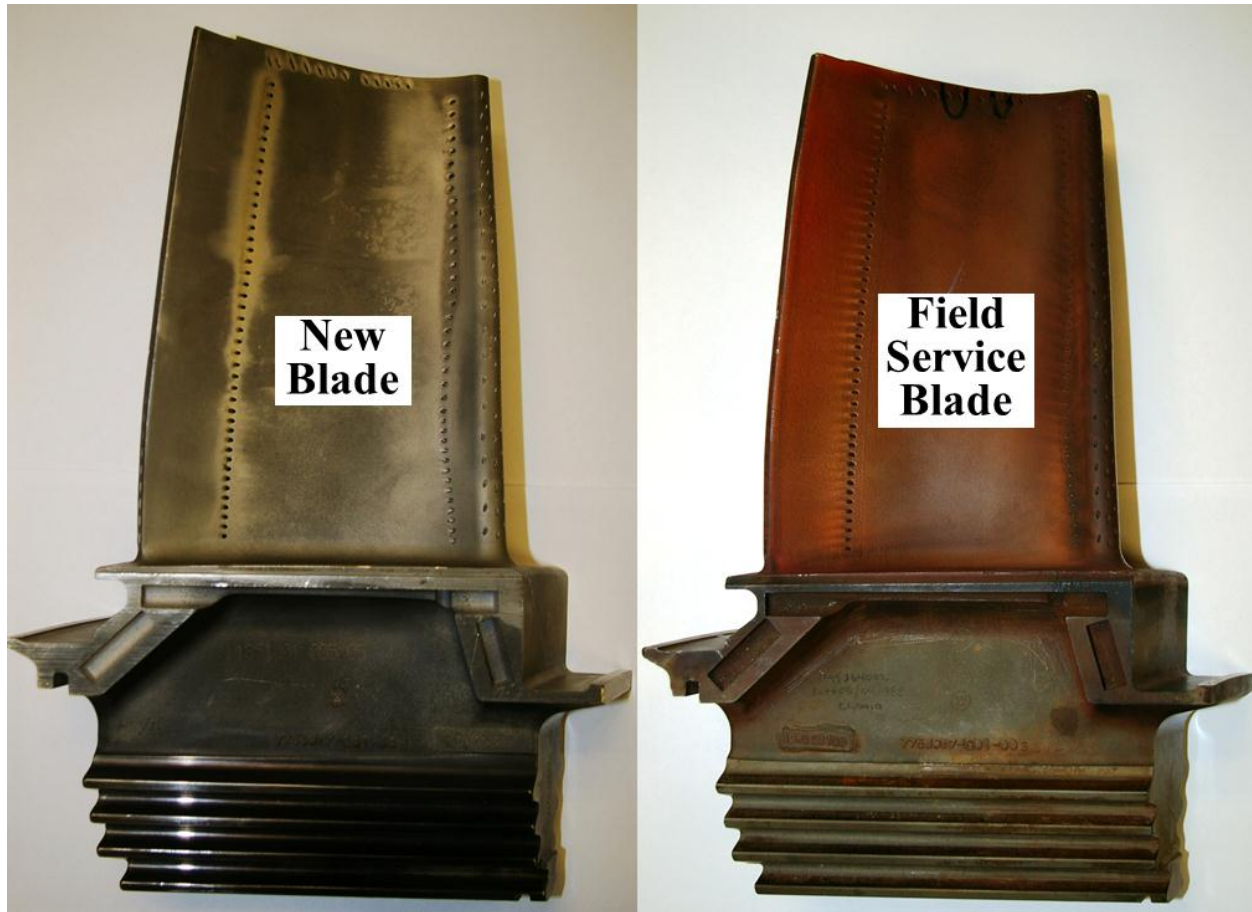


**Figure 3.12. Two blades from the first row of a land-based gas turbine engine.**

The two blades were installed side by side as shown in Figure 3.13, and a consistent platform gap of 1.27 mm was maintained with gage blocks placed at each end of the seal pin. This gap is representative of the engine cold-build gap as reported in [1]. The blades and test chamber were sealed with gasket material and silicone such that the flow was restricted to the area along the length of the axial seal pin. Epoxy was applied between the gage blocks and the rear blade to maintain their position and create a seal. For the majority of tests performed, the gage blocks were not sealed where they contacted the front blade platform. Later flow tests performed with silicone applied between the gage blocks and the front blade platform confirmed that flow leakage between the gage blocks and the front blade platform was negligible and did not influence the flow test results. Since the seal pin was slightly shorter than the length of the slot to allow for free movement of the pin, there was potential for flow to leak around the ends of the seal pin. As shown in Figure 3.14, gasket material and silicone were used to seal the areas



between the ends of the seal pin and the seal pin slot, thereby restricting flow to the contact areas along the length of the pin.

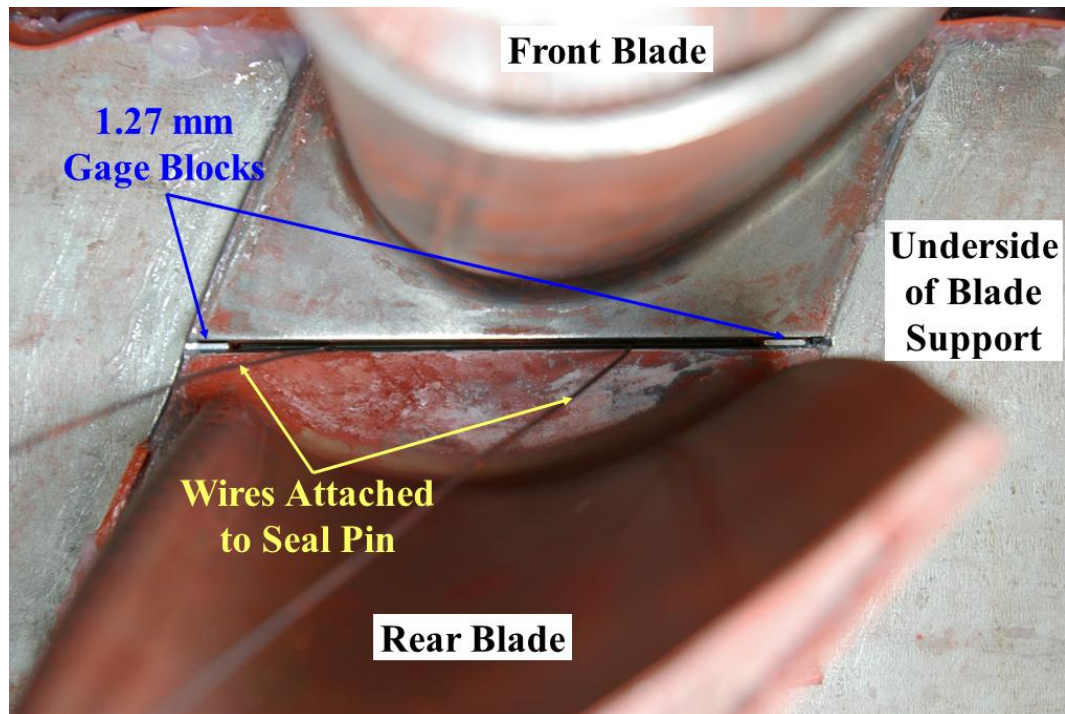


Figure 3.13. The installation of the blades as viewed from the underside of the test chamber.

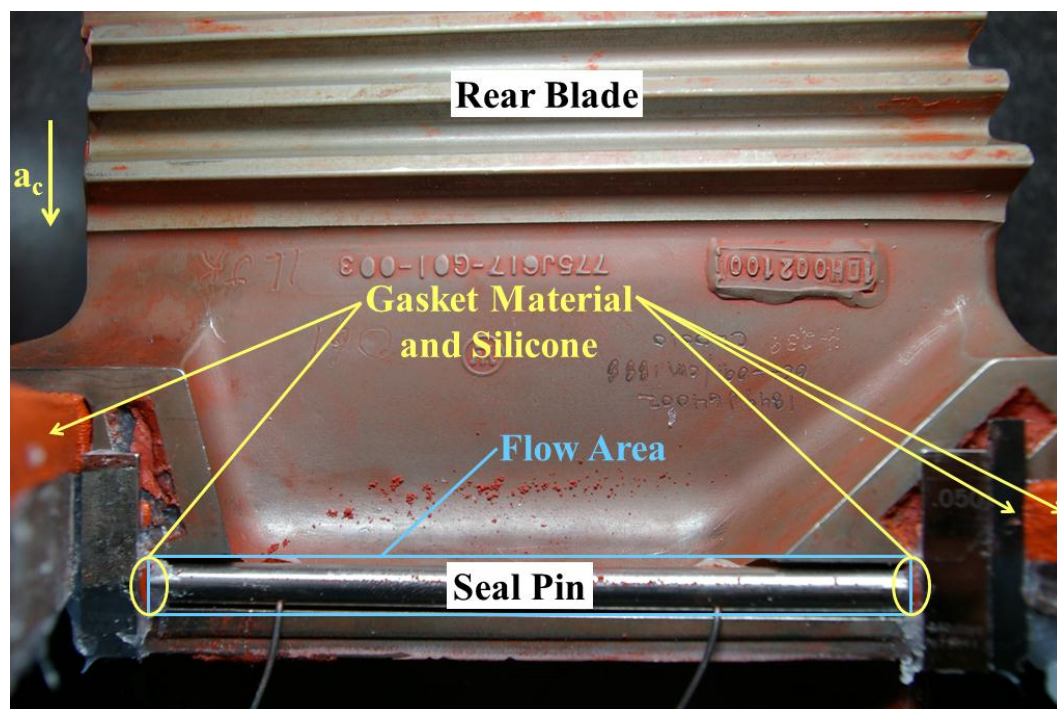
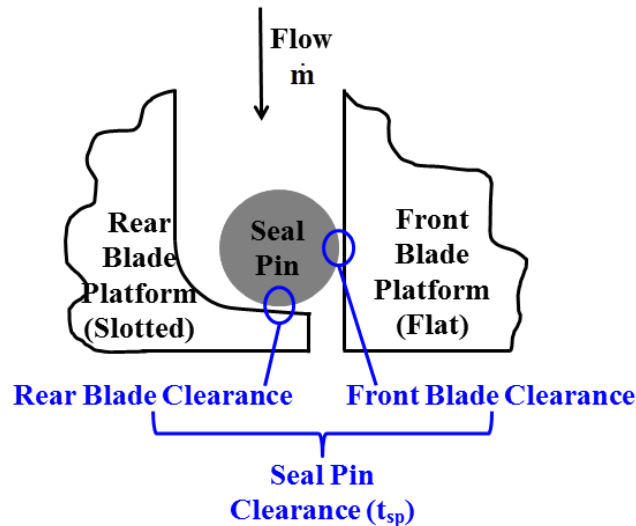


Figure 3.14. The flow area at the seal pin as viewed from the front of the test chamber (front panel, front bar, and front blade removed for clarity).

A cross-section of the seal pin and front and rear blade platforms is shown schematically in Figure 3.15. The flow area consisted of two clearances where the seal pin made imperfect contact with the slotted rear blade and flat front blade platform surfaces. Due to manufacturing techniques, each of these contacting surfaces had a rough surface finish, which created small gaps at the contact areas and allowed leakage of air along the length of the seal pin. The small sizes of these clearances made them impractical to measure, so their value was estimated. A one-dimensional analysis was performed using the two clearances lumped together into what is referred to as the seal pin clearance ( $t_{sp}$ ) for the purpose of estimating the seal pin flow area. A seal pin clearance of 0.0254 mm was assumed. Taken with the known seal pin length ( $L_{sp}$ ) of 110 mm, this clearance was used in Equation 3.3 to calculate an assumed flow area ( $A_{sp}$ ) of 2.80 mm<sup>2</sup>.

$$A_{sp} = t_{sp} \cdot L_{sp} \quad (3.3)$$



**Figure 3.15. The seal pin clearance consisted of two clearance gaps between the seal pin and rear and front blade platforms (side cross-sectional view).**

As it was previously shown in Figure 3.14, a combination of silicone rubber gasket material and RTV silicone was used to seal between the blade platforms and the test chamber blade support piece. Initially, the test chamber was assembled with a piece of gasket material installed between the two blade platforms and shown to be sealed by a pressure test. During testing, however, it was not possible to perform a pressure leak test due to the inherent leakage



area at the seal pin. A detailed multi-step procedure was followed throughout the disassembly and reassembly process to insure consistent installation of the blades, seal pin, gage blocks, and gasket material in the test chamber. As shown in Figure 3.16, repetition of the baseline flow function versus pressure ratio curve for multiple assemblies gave confidence that the assembly method was consistent and created a hermetic seal between the blade platforms and the blade support. A derivation of the flow function is provided in Section 3.7.

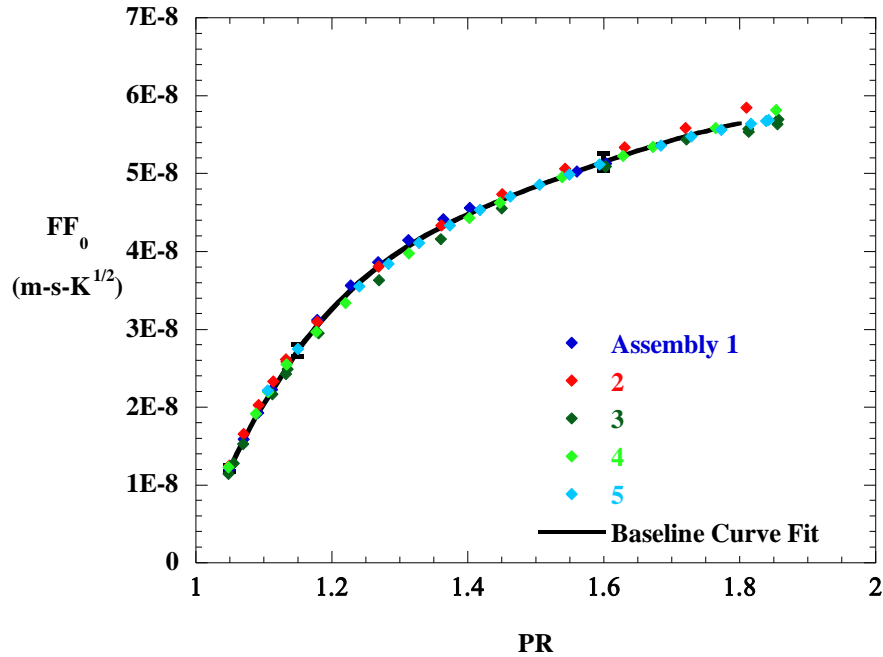


**Figure 3.16. Data from multiple test chamber assemblies were compared to show consistency in the flow area.**

During engine operation, rotation of the blades induces centrifugal acceleration acting in the outward radial direction, or downward as viewed in Figure 3.14. This acceleration would normally exert an outward radial force on the axial seal pin, causing it to contact the radial outermost edge of the seal pin slot. Since experiments were performed on static blades, it was necessary to replicate this force through other means in order to achieve an engine-representative leakage flow area. To preserve the original engine hardware, a smooth 6.35 mm diameter stainless steel rod was machined to length and chamfered on the ends similar to the axial seal pin. Two 1 mm diameter holes were drilled in the pin, and 0.98 mm wire was threaded through the holes and bent to secure the wire in the holes. Epoxy was applied to the upstream ends of the wires to prevent air leakage through the holes in the pin. The wires passed through the blade

platform gap, as shown in Figure 3.13, and were kept in tension with a clamp on the airfoil side of the blades.

### 3.6 Description of Rotating Test Coupons

To reduce the size and mass of the rotating components, test coupons were made to represent a section of the blade platform including the seal pin slot and some of the contoured surface between the seal pin slot and the root. Shown in Figure 3.17, the test coupon section was 27.9 mm wide, which is about one-fourth of the full-scale seal pin slot length. Each test coupon consisted of two separable halves representative of two adjacent blade platforms. Except for the area along the length of the seal pin, the coupon halves were sealed with silicone along their mating faces before being bolted together for installation in the rotating chamber. To represent the engine hardware cold-build conditions, the test coupons were designed to maintain a 1.27 mm platform gap between the two halves along the length of the seal pin [1].

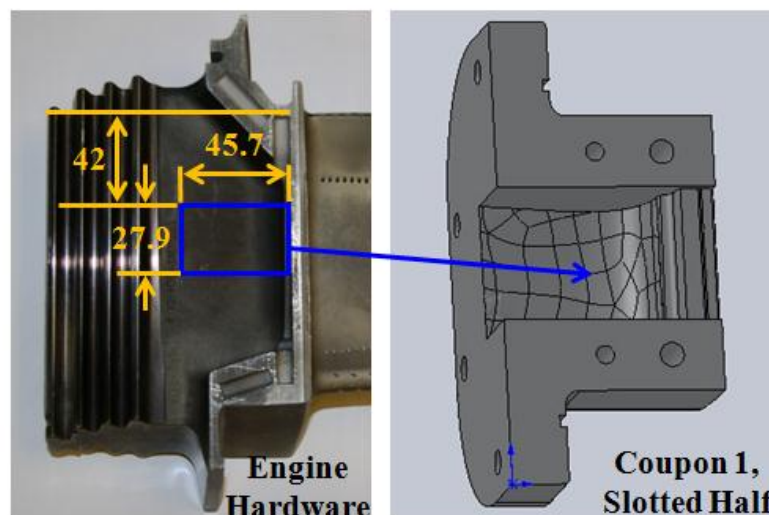


**Figure 3.17. The section of the engine hardware used to create the rotating test coupon (dimensions in mm).**

Shown in Figure 3.18, two test coupons were used in the rotating test facility and are hereafter referred to as coupon 1 and coupon 2. The direction of rotation was representative of engine conditions with the slotted half leading and the flat half following. Both coupons used the same design for the flat half, which was created from a coordinate-measuring machine (CMM) scan of the flat side of the engine hardware blade platform. The difference in the two coupons was confined to the slotted half. A CMM scan of the slotted side of the blade platform

was used to create the slotted half of coupon 1. Like the slotted engine hardware, coupon 1 included a lip upstream of the seal pin contact area. To create coupon 2, the lip in coupon 1 was removed, yielding a smooth surface transition upstream of the seal pin contact area. Detailed drawings of the two test coupons are provided in Appendix E.

As discussed in Section 3.5, the flow area in the engine hardware was created from imperfect contact between the smooth seal pin and the rough seal pin slot surfaces. It was therefore important to replicate in the test coupon the surface finish of the engine hardware at the seal pin slot. Based on a previous study, the plunge-electrical discharge machining (EDM) technique was determined to be best suited for creating a rough surface on the test coupon similar to that of the engine hardware [24]. Several different samples of test coupon material were machined by plunge-EDM and compared with the engine hardware. Three-dimensional surface profiles of the engine hardware and plunge-EDM samples were measured using a Wyko NT1100 optical profilometer. The surface profiles for the engine hardware and the most similar EDM sample are shown in Figure 3.19 and Figure 3.20, respectively. Comparison of the two surface plots shows that, while both the engine hardware and the EDM sample exhibited similar variation from the mean surface height, the peaks of the engine hardware slot surface were relatively more rounded and smooth. This difference was most likely caused by wear to the engine hardware surface during field service.

Results from the optical profilometry measurement also included numerical surface finish parameters, which are provided in Table 3.8. Parameter values are given on a 95% confidence interval based on multiple measurement locations on each surface. Area-averaged parameters represent the average over the lateral measurement area (227  $\mu\text{m}$  by 299  $\mu\text{m}$ ), while two-dimensional trace parameters represent the average from a series of linear cuts taken across the measured surface profile. Both parameters yielded the RMS surface roughness ( $R_q$ ), which represents the root-mean-square average surface height relative to the mean [25]. Peak-to-valley spacing was also determined from the two-dimensional trace data. For a particular two-dimensional trace, this parameter represents the lateral spacing from the highest peak to the lowest valley. The height above surface parameter was determined from the volume required to submerge the surface to its highest peak divided by the measurement surface area. As such, the height above surface represents the average distance between the surface and a plane contacting the highest peak and parallel to the plane of mean surface height.

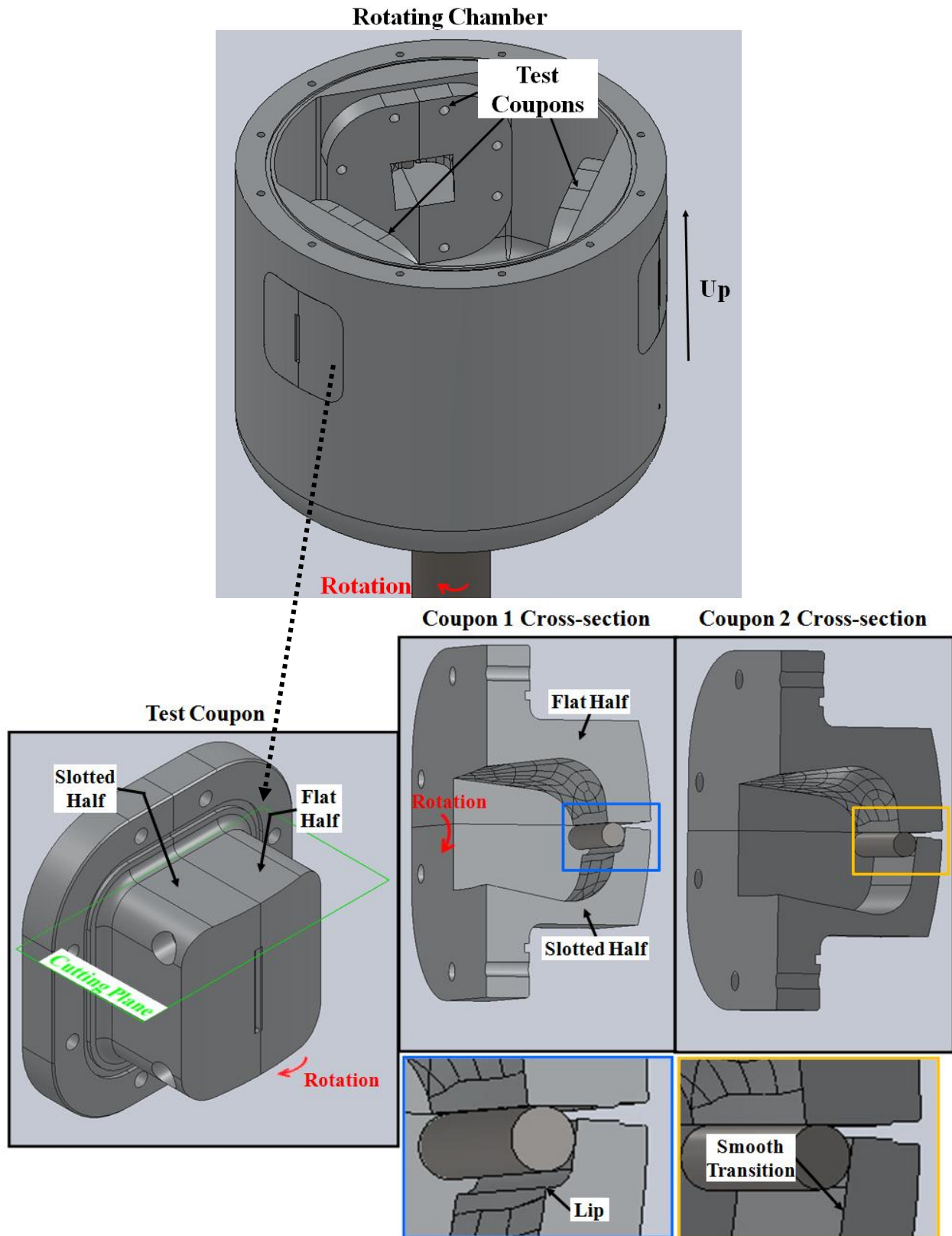


Figure 3.18. Coupon 1 had a lip near the seal pin contact area, while coupon 2 had the lip removed for a smooth transition.

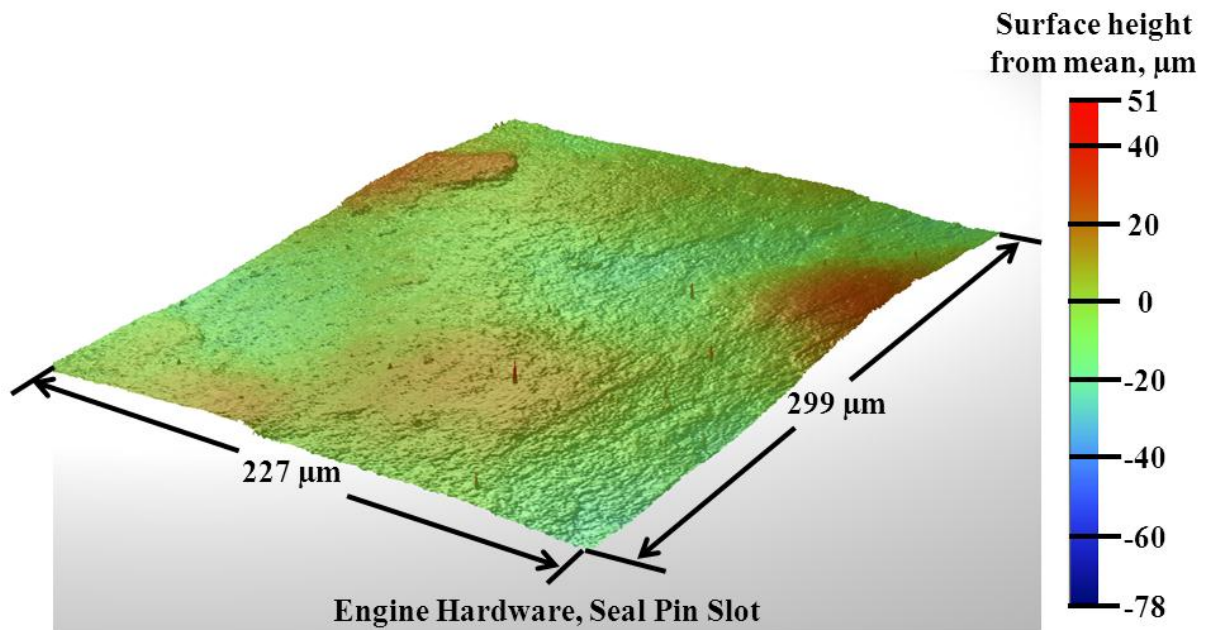


Figure 3.19. Three-dimensional optical profilometry surface plot for engine hardware.

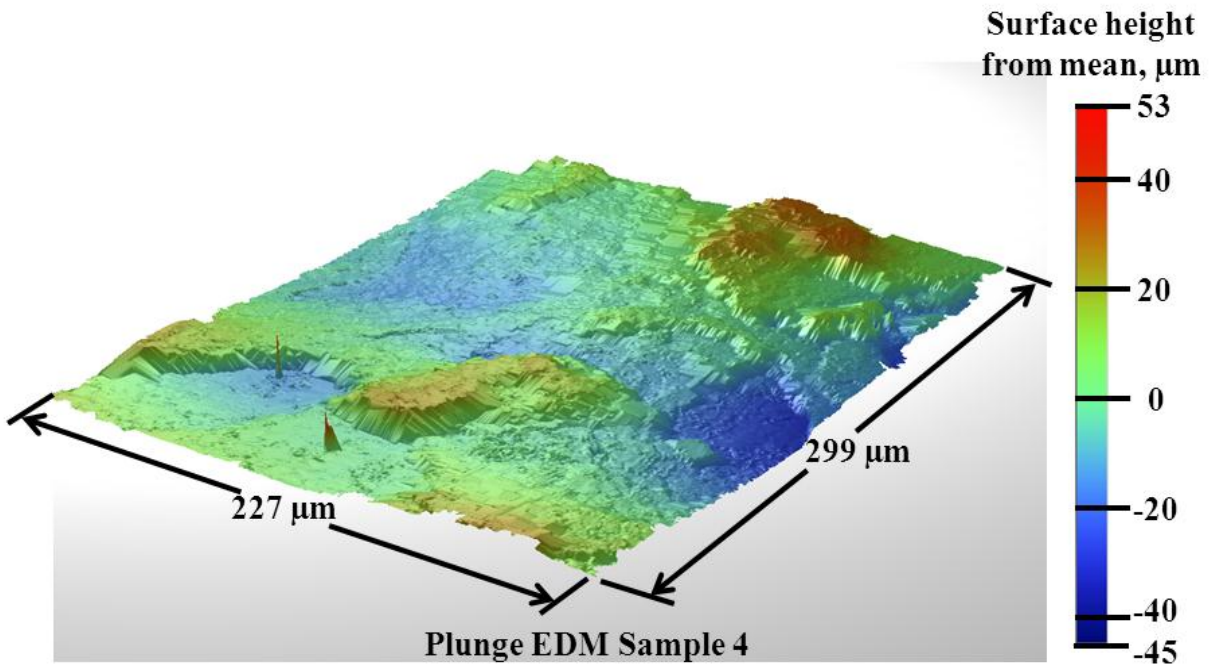


Figure 3.20. Three-dimensional optical profilometry surface plot for plunge-EDM sample 4.

**Table 3.8. Surface Finishes of Engine Hardware and Plunge-EDM Samples**

Surface	Analysis Type	Peak-to-Valley Spacing ( $\mu\text{m}$ )	$R_q$ ( $\mu\text{m}$ )	Height Above Surface ( $\mu\text{m}$ )
Engine Hardware, Seal Pin Slot	Area Average	N/A	$6.8 \pm 2.8$	$14.6 \pm 5.9$
	2-D Trace	$147 \pm 54$	$6.7 \pm 3.0$	N/A
Plunge-EDM Sample 1	Area Average	N/A	$10.1 \pm 1.1$	$20.8 \pm 2.6$
	2-D Trace	$126 \pm 16$	$9.4 \pm 1.0$	N/A
Plunge-EDM Sample 2	Area Average	N/A	$7.8 \pm 0.6$	$14.3 \pm 1.6$
	2-D Trace	$116 \pm 19$	$7.8 \pm 0.5$	N/A
Plunge-EDM Sample 3	Area Average	N/A	$16.8 \pm 3.7$	$32.4 \pm 10.6$
	2-D Trace	$118 \pm 14$	$15.0 \pm 2.2$	N/A
Plunge-EDM Sample 4	Area Average	N/A	$16.0 \pm 2.4$	$33.6 \pm 7.7$
	2-D Trace	$132 \pm 11$	$14.1 \pm 2.6$	N/A

Surface profilometry parameters and visual inspection of magnified areas larger than those sampled during optical profilometry measurements were used to compare the EDM surfaces to the engine hardware. All of the plunge-EDM samples lacked the wear that was evident on the engine hardware, so their surface finishes were all somewhat different from the engine hardware. The surface finish of sample 4 was selected for replication in the rotating test coupons as a balance between matching the surface roughness height and the lateral spacing of surface roughness elements to the engine hardware. While other EDM samples were better matches of the engine hardware in terms of the  $R_q$  and height above surface parameters, they exhibited closer lateral spacing of surface roughness elements.

In order to match the forces at the seal pin contact area due to the centrifugal force, it was important to match the seal pin density to that of the engine hardware. Seal pins for the test coupons were machined from Inconel X-750, the same material used for the engine hardware. The test coupon seal pins were machined and ground to a smooth finish. They measured 6.35 mm diameter by 27.9 mm long, about one-fourth of the engine hardware seal pin length.

### 3.7 Data Analysis

Flow of gas through a nozzle or diffuser can be approximated as one-dimensional, isentropic flow of an ideal gas, which permits definition of a non-dimensional flow parameter that can be used to predict the flow through a nozzle or diffuser if the upstream total to downstream static pressure ratio ( $P_0/p_b$ ) is known. For the tests under consideration in this study,

the experimental setup consisted of a relatively large upstream plenum followed by a narrow flow area at the seal pin, which in a simplified sense, are analogous to the upstream reservoir and nozzle shown in Figure 3.21. Following is a derivation of the non-dimensional flow parameter for the case of one-dimensional isentropic flow of an ideal gas through a nozzle with a large upstream reservoir. Nomenclature corresponds with that shown in Figure 3.21.

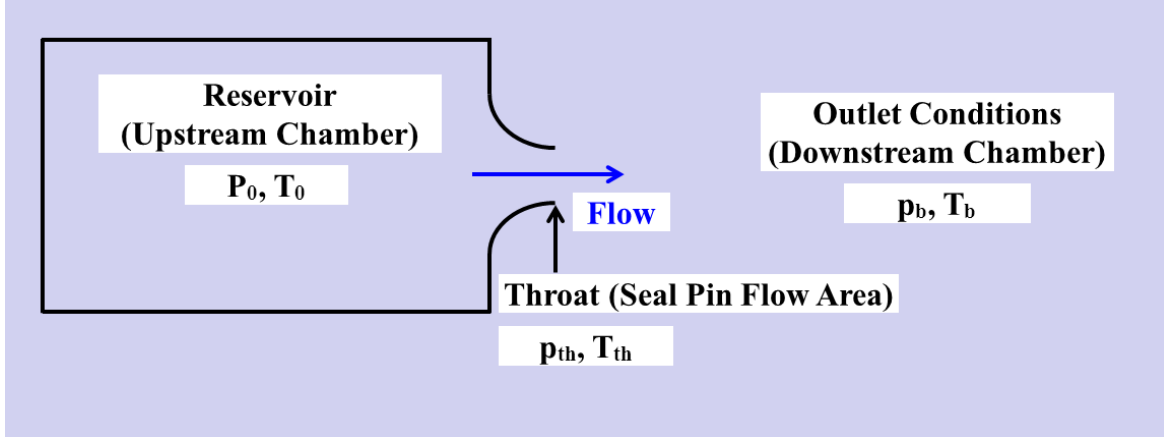


**Figure 3.21. The seal pin flow area may be approximated as a nozzle downstream of a large reservoir.**

The mass flow rate through the nozzle is defined in Equation 3.4, where the density  $\rho$ , speed of sound  $c$ , Mach number  $Ma$ , and cross sectional area  $A$  are all evaluated at the throat, the narrowest cross-sectional area of the nozzle.

$$\dot{m} = \rho_{th} \cdot c_{th} \cdot Ma_{th} \cdot A_{th} \quad (3.4)$$

For isentropic flow of an ideal gas, the relationship between Mach number and downstream static to upstream total pressure ratio ( $p_{th}/P_0$ ) is given by Equation 3.5.

$$\frac{p_{th}}{P_0} = \left[ \frac{1}{1 + \left( \frac{\gamma - 1}{2} \right) \cdot Ma_{th}^2} \right]^{\frac{\gamma}{\gamma - 1}} \quad (3.5)$$

Rearranging Equation 3.5 yields Equation 3.6, a more convenient expression for the Mach number as a function of pressure ratio.

$$Ma_{th} = \left\{ \left[ \left( \frac{P_0}{p_{th}} \right)^{\frac{\gamma - 1}{\gamma}} - 1 \right] \cdot \frac{2}{\gamma - 1} \right\}^{\frac{1}{2}} \quad (3.6)$$

In addition, the relationship between Mach number and static to total temperature ratio ( $T_{th}/T_0$ ) is given by Equation 3.7.

$$\frac{T_{th}}{T_0} = \frac{1}{1 + \left(\frac{\gamma - 1}{2}\right) \cdot Ma_{th}^2} \quad (3.7)$$

Equation 3.8 holds for isentropic flow of an ideal gas.

$$\frac{p}{\rho^\gamma} = \text{constant} \quad (3.8)$$

Using Equation 3.8 and the ideal gas equation of state, the throat density may be written as in Equation 3.9. Because the upstream chamber is a reservoir with large cross-sectional area relative to the throat area, the gas velocity in the upstream chamber is negligible, and static and total conditions are approximately equivalent.

$$\rho_{th} = \left(\frac{p_{th}}{P_0}\right)^{\frac{1}{\gamma}} \cdot \frac{P_0}{R \cdot T_0} \quad (3.9)$$

Making use of Equation 3.7, the speed of sound at the throat may be written as in Equation 3.10.

$$c_{th} = \left[ \frac{\gamma \cdot R \cdot T_0}{1 + \left(\frac{\gamma - 1}{2}\right) \cdot Ma_{th}^2} \right]^{\frac{1}{2}} \quad (3.10)$$

With some intermediate algebra, Equation 3.4 may now be manipulated to yield the non-dimensional flow parameter FP, given in Equation 3.11.

$$FP = \frac{\dot{m} \sqrt{R \cdot T_0}}{P_0 \cdot A_{th}} = \left\{ \left[ \left(\frac{p_{th}}{P_0}\right)^{\frac{2}{\gamma}} - \left(\frac{p_{th}}{P_0}\right)^{\frac{\gamma+1}{\gamma}} \right] \frac{2\gamma}{(\gamma-1)} \right\}^{\frac{1}{2}} \quad (3.11)$$

For subsonic conditions at the nozzle throat, the throat pressure  $p_{th}$  is equal to the outlet back pressure  $p_b$ . Consider the nozzle operating with a constant upstream total pressure and a variable static back pressure. As the back pressure is decreased, the mass flow rate and throat Mach number increase up to the point of choking, when the throat Mach number is one and the



back pressure is at the critical value  $p_b^*$ . From Equation 3.5, the choked condition can be shown to occur at the critical pressure ratio of 0.528, as shown in Equation 3.12.

$$\frac{p_b^*}{P_0} = 0.528 \quad (3.12)$$

For the present study, the pressure ratio is defined as the upstream total pressure divided by the downstream back pressure, which is the inverse of Equation 3.12. The critical pressure ratio ( $PR^*$ ) then becomes 1.89, as shown in Equation 3.13.

$$PR^* = \frac{P_0}{p_b^*} = 1.89 \quad (3.13)$$

For an upstream total to downstream back pressure ratio less than or equal to the critical value given in Equation 3.13, the throat Mach number is less than or equal to one, which means the fluid velocity at the throat is at most equal to the speed of sound. Pressure waves are therefore able to propagate throughout the flow, so there are no discontinuities in pressure and the throat pressure ( $p_{th}$ ) is equal to the back pressure ( $p_b$ ). Thus, for subsonic flow, the flow parameter may be rewritten in terms of the downstream back to upstream total pressure ratio, as shown in Equation 3.14.

$$FP = \frac{\dot{m}\sqrt{R \cdot T_0}}{P_0 \cdot A_{th}} = \left\{ \left[ \left( \frac{p_b}{P_0} \right)^{\frac{2}{\gamma}} - \left( \frac{p_b}{P_0} \right)^{\frac{\gamma+1}{\gamma}} \right] \frac{2\gamma}{(\gamma-1)} \right\}^{\frac{1}{2}} \quad (3.14)$$

Continuing to hold the upstream total pressure constant, further reduction of the back pressure below what is required to achieve the critical pressure ratio results in choked nozzle operation, when the fluid speed is sonic in the throat ( $Ma_{th} = 1$ ). At or above the critical pressure ratio, pressure waves are unable to propagate upstream against the sonic throat velocity. The throat static pressure remains at  $p_b^*$  and is greater than the back pressure  $p_b$ , resulting in a pressure discontinuity at the nozzle exit. The upstream conditions are therefore insensitive to further reduction in back pressure, and the mass flow rate reaches its maximum at the critical pressure ratio. For the present study, the pressure ratio was such that throat conditions were always subsonic.

The expression in Equation 3.14 shows the mass flow rate is dependent on the gas total temperature, upstream total pressure, pressure ratio, and flow area. Various forms of this flow parameter are commonly used, and often the area and gas constant terms are excluded from the

left-hand side. A dimensional form of the flow parameter is given in Equation 3.15 and hereafter referred to as the flow function to distinguish it from the non-dimensional form. The units used for the flow function are  $\text{m} \cdot \text{s} \cdot \text{K}^{1/2}$ .

$$\text{FF} = \frac{\dot{m} \sqrt{T_0}}{P_0} = A_{\text{th}} \cdot \left\{ \left[ \left( \frac{P_b}{P_0} \right)^{\frac{2}{\gamma}} - \left( \frac{P_b}{P_0} \right)^{\frac{\gamma+1}{\gamma}} \right] \frac{2\gamma}{R(\gamma-1)} \right\}^{\frac{1}{2}} \quad (\text{m} \cdot \text{s} \cdot \text{K}^{1/2}) \quad (3.15)$$

Flow through the static engine hardware was characterized in terms of the flow function, defined as the mass flow rate times the square root of the upstream total temperature divided by the upstream total pressure. The flow function is specific to a particular flow area since the area term has been excluded from the left-hand side. Thus, a change in area such as that resulting from particle blockage results in a change in flow function.

For a particular flow area, it is possible to generate a theoretical curve of isentropic flow function versus pressure ratio. To predict nozzle flow behavior, the discharge coefficient ( $C_D$ ) is needed to account for non-isentropic effects, multi-dimensional flow effects, and the effective reduction in flow area due to the boundary layer thickness. The discharge coefficient is less than unity and is multiplied by the isentropic flow function. A constant discharge coefficient of 0.816 was assumed based on a one-dimensional engine analysis [26]. The assumed values for discharge coefficient and seal pin flow area were used in Equation 3.16 to generate a curve of predicted flow function versus pressure ratio, shown in Figure 3.22. As the pressure ratio increases, the predicted flow function initially increases and reaches a maximum value at the critical pressure ratio of 1.89 due to choking.

$$\text{FF}_p = C_D \cdot A_{\text{sp}} \cdot \left\{ \left[ \left( \frac{P_b}{P_0} \right)^{\frac{2}{\gamma}} - \left( \frac{P_b}{P_0} \right)^{\frac{\gamma+1}{\gamma}} \right] \frac{2\gamma}{R(\gamma-1)} \right\}^{\frac{1}{2}} \quad (3.16)$$

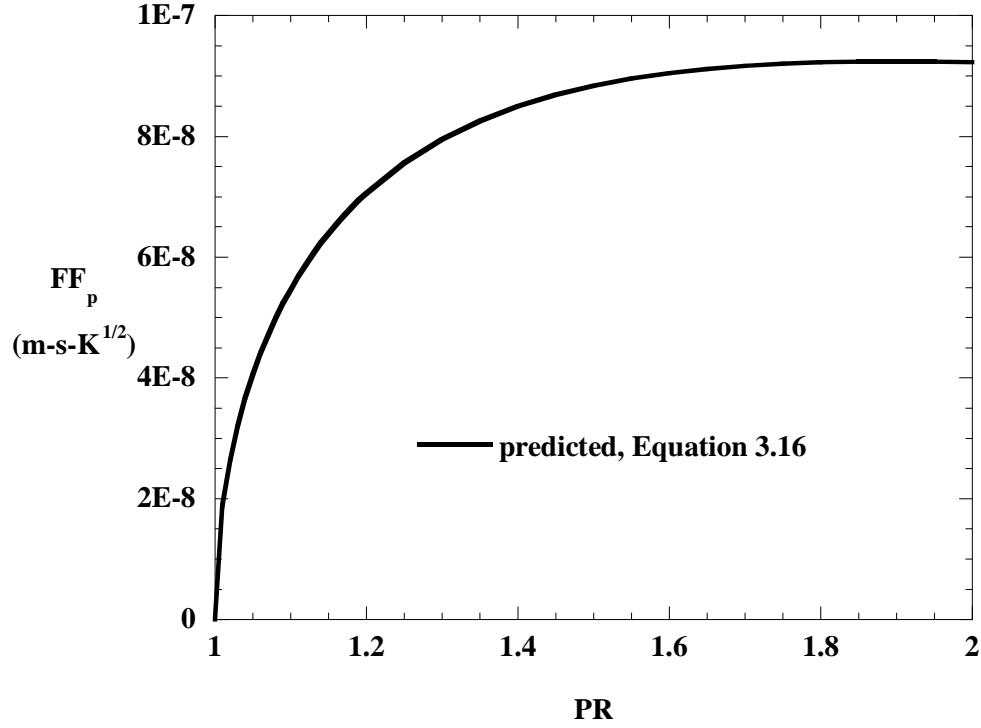


**Figure 3.22. The predicted flow function versus pressure ratio curve for the assumed seal pin flow area and discharge coefficient.**

The flow function given in Equation 3.15 was derived for a static orifice or nozzle. For the case of a rotating nozzle, Maeng et al. [27] have shown experimentally there is additional energy imparted to the flow through transfer of angular momentum from the nozzle. An energy balance performed on a control volume including a rotating nozzle and its surroundings yields Equation 3.17, where the left-hand side represents the work done on the fluid element due to rotation,  $r$  is radius of the nozzle about the axis of rotation, and  $v_{th}$  is the fluid velocity at the throat of the nozzle.

$$\frac{(r \cdot \omega)^2}{2} = c_p T_b + \frac{v_{th}^2}{2} - c_p T_0 \quad (3.17)$$

Recognizing that the fluid velocity has both radial and circumferential components, Equation 3.17 can be rewritten in terms of the radial throat velocity component ( $v_{th,r}$ ) as Equation 3.18. In the present rotating study, the seal pin flow area was oriented such that its axis was in the radial direction, so the radial component of the nozzle throat velocity represents the fluid velocity at the nozzle throat in the rotating reference frame.

$$v_{th,r}^2 = (r \cdot \omega)^2 + 2c_p (T_0 - T_{th}) \quad (3.18)$$

It is convenient to define a rotational temperature ( $T_{\text{rot}}$ ) as in Equation 3.19.

$$T_{\text{rot}} = \frac{(\mathbf{r} \cdot \boldsymbol{\omega})^2}{2c_p} \quad (3.19)$$

Using Equation 3.19, expressions for rotational total temperature ( $T_{0,\text{rot}}$ ) rotational total pressure ( $P_{0,\text{rot}}$ ) may be written as in Equations 3.20 and 3.21, respectively.

$$T_{0,\text{rot}} = T_0 + T_{\text{rot}} \quad (3.20)$$

$$P_{0,\text{rot}} = P_0 \left( 1 + \frac{T_{\text{rot}}}{T_0} \right)^{\frac{\gamma}{\gamma-1}} \quad (3.21)$$

With the assumption of isentropic flow, a more general form of the flow function suitable for both rotating and static conditions can be derived from Equations 3.20 and 3.21 and is given in Equation 3.22. This expression is hereafter referred to as the rotational flow function and denoted  $FF_{\text{rot}}$ . Comparing Equation 3.20 with Equation 3.15, it is evident that the rotational flow function reduces to the static flow function for the non-rotating case ( $\omega = 0$ ).

$$FF_{\text{rot}} = \frac{\dot{m} \sqrt{T_{0,\text{rot}}}}{P_{0,\text{rot}}} = A_{\text{th}} \left\{ \left[ \left( \frac{P_b}{P_0} \right)^{\frac{2}{\gamma}} \left( 1 + \frac{T_{\text{rot}}}{T_0} \right) - \left( \frac{P_b}{P_0} \right)^{\frac{\gamma+1}{\gamma}} \left( 1 + \frac{T_{\text{rot}}}{T_0} \right)^{\frac{-\gamma-1}{\gamma-1}} \right] \frac{2\gamma}{R(\gamma-1)} \right\}^{\frac{1}{2}} \quad (\text{m} \cdot \text{s} \cdot \text{K}^{1/2}) \quad (3.22)$$

It is also convenient to define a rotational pressure ratio ( $PR_{\text{rot}}$ ) as in Equation 3.23, which reduces to the pressure ratio used in the static analysis for the non-rotating case.

$$PR_{\text{rot}} = \left( \frac{P_0}{P_b} \right) \left( 1 + \frac{T_{\text{rot}}}{T_0} \right)^{\frac{\gamma}{\gamma-1}} \quad (3.23)$$

Making use of Equation 3.23, the rotational flow function given in Equation 3.22 can be written in a more compact form as in Equation 3.24. Flow through the rotating test coupons was characterized in terms of this rotational flow function and the rotational pressure ratio given in Equation 3.23. Details of the flow function and pressure ratio calculations are provided in Appendices A and B.

$$FF_{\text{rot}} = \frac{\dot{m} \sqrt{T_{0,\text{rot}}}}{P_{0,\text{rot}}} = A_{\text{th}} \left\{ \left[ \left( \frac{1}{PR_{\text{rot}}} \right)^{\frac{2}{\gamma}} - \left( \frac{1}{PR_{\text{rot}}} \right)^{\frac{\gamma+1}{\gamma}} \right] \frac{2\gamma}{R(\gamma-1)} \right\}^{\frac{1}{2}} \quad (\text{m} \cdot \text{s} \cdot \text{K}^{1/2}) \quad (3.24)$$

### 3.8 Procedure for Static Tests

The previously described static test facility was used to measure air flow through the seal pin flow area for clean engine hardware and after particle injection. All tests were performed at laboratory ambient temperatures. Shown in Figure 3.23, a curve fit of flow function versus pressure ratio was generated for clean engine hardware for two purposes: 1) to experimentally characterize flow through the seal pin flow area, and 2) to establish a baseline flow function for checking the assembly and measuring flow reduction. This flow function is subsequently referred to as the baseline flow function and denoted by  $FF_0$ . The test chamber and engine hardware were assembled and disassembled several times, and the experimental flow function data were averaged to generate the baseline flow function curve. Original experimental data are for test chamber assemblies performed with no silicone applied between the gage blocks and front blade platform, while retest experimental data are for assemblies performed 8 months later with silicone applied between the gage blocks and front blade platform. The baseline curve fit was generated from the original experimental data. Since the retest data matches well with the baseline flow function curve, the absence of silicone between the gage blocks and the front blade platform did not have a significant effect on the results. In other words, any flow leakage between the gage blocks and front blade platform was negligible. The curve fit equation used for the static baseline flow function is provided in Appendix A.

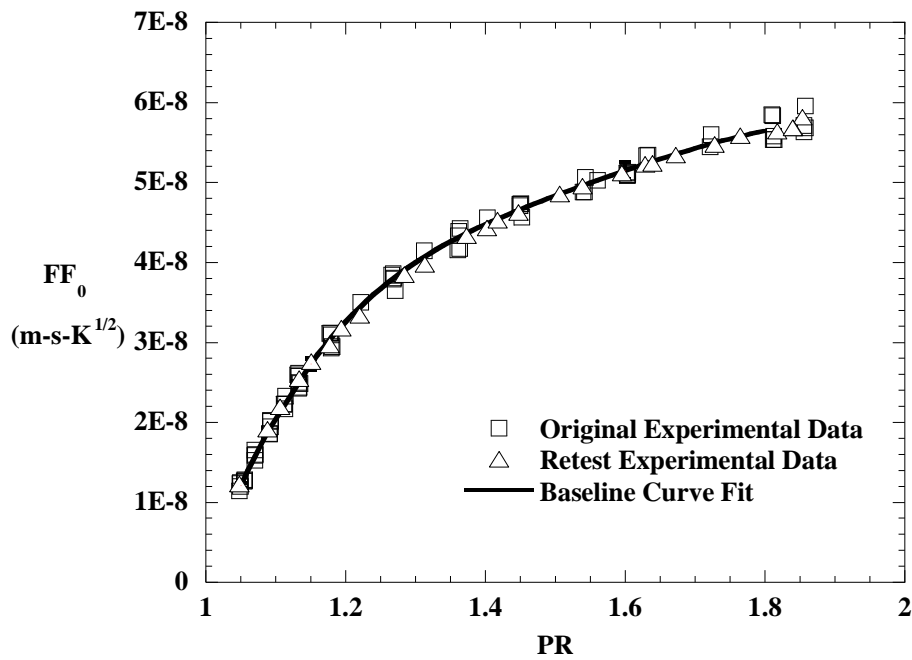
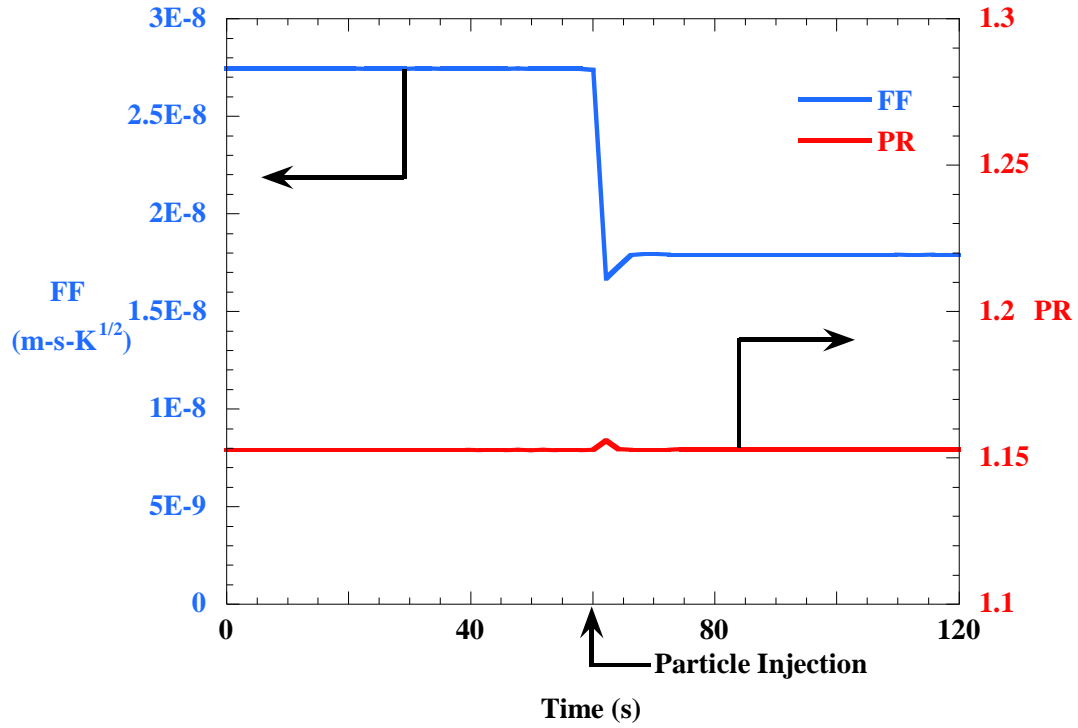


Figure 3.23. Baseline flow function for clean engine hardware.

Before each test, the flow area around the seal pin was thoroughly cleaned using a combination of blowing with compressed air, brushing, and cleaning with liquid solution. Additionally, the flow function was measured at one or more pressure ratios and was required to match the clean baseline curve to insure a consistent and leak-free assembly. If the measured flow function did not match the baseline curve, there were three likely causes: 1) variation in assembly of the blades and seal pin, 2) a leak in the test chamber or piping, or 3) deposited rust particles remaining at the seal pin flow area from a previous test.

After matching the baseline flow function, a particle injection test proceeded as follows. The particles were heated in an oven at 200°C for at least 2 hours to insure they were dry and of consistent moisture content. Particles were then removed from the oven and allowed to cool to ambient conditions. Recalling Figure 3.7, the desired mass of particles was measured and poured into the particle feed piping with the ball valve in the closed position, and the feed pipe cap was reinstalled and sealed with pipe thread tape. After setting the desired pressure ratio and allowing the air flow through the test chamber to reach steady conditions, the ball valve was opened, releasing particles into the flow. As shown in Figure 3.24, releasing a given mass of particles into the flow yielded a step decrease in flow function and a slight change in pressure ratio, both of which remained constant with time several seconds after particle injection.



**Figure 3.24. Blocked flow conditions reached steady values shortly after injecting rust particles (shown for rust mass of 0.23 g).**

After particle injection, most of the rust particles were entrained in the flow and either passed through the seal pin gap or deposited on the seal pin and blade platform surfaces. Very few particles were found on the upstream chamber surfaces upon disassembly. Blockage due to particle deposition at the seal pin flow area was measured as a percent reduction in flow function (RFF) following the method described in [15]. The terms clean and blocked refer to pre- and post-particle injection conditions, respectively. The reduction in flow function is defined in Equation 3.25 and was measured as the difference between the blocked flow function and the baseline flow function ( $FF_0$ ) evaluated at the blocked pressure ratio. The reduction in flow function is shown schematically in Figure 3.25 for a particular blockage test. See Appendix A for details of the flow function and blockage calculations from experimentally measured parameters.

$$RFF = 1 - \frac{FF}{FF_0} \bigg|_{PR} \quad (3.25)$$

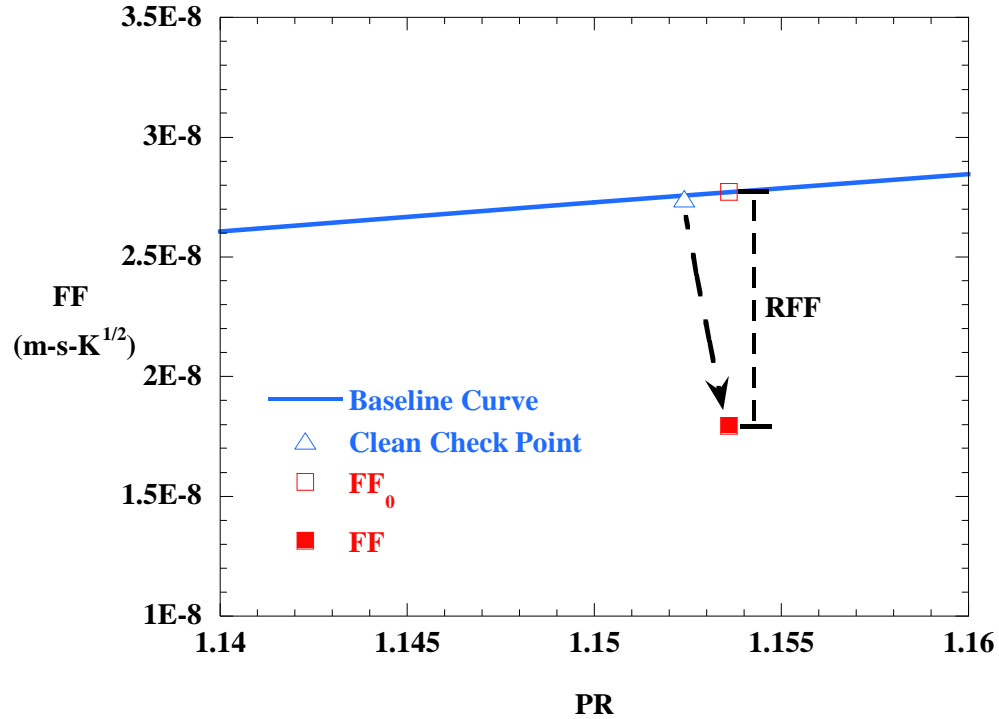


**Figure 3.25. Blockage was measured in terms of a reduction in flow function evaluated at the blocked pressure ratio (zoomed view shown).**

### 3.9 Procedure for Rotating Tests

Rust injection tests in the rotating test facility were performed with three identical test coupons open to flow and particle deposition; therefore flow blockage measured in each test was considered an average of the blockage in three parts. For coupon 1, the clean flow function was measured over a range of pressure ratios at  $\Omega = 0.002$ , first for each coupon individually and then for all three coupons open to flow simultaneously. Multiple assemblies of the test coupons and seal pins were performed to show the baseline flow function was repeatable. As shown in Figure 3.26, the baseline flow function for each coupon was similar and matched the one-third-scale flow function for flow through all three coupons. It was necessary to scale the data for all three coupons open to flow because the flow function was not normalized by the flow area.



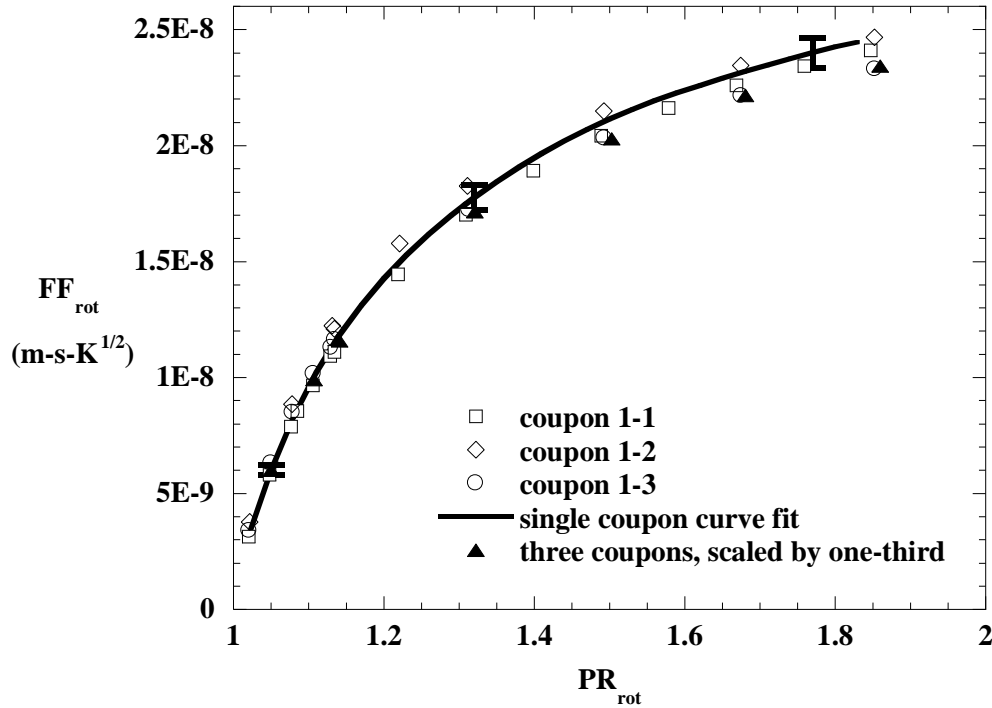


**Figure 3.26. Flow function for flow through a single coupon 1 at  $\Omega = 0.002$ .**

Shown in Figure 3.27, baseline flow function curves were generated for coupons 1 and 2 at  $\Omega = 0.002$  and  $\Omega = 1$  with all three coupons open to flow. As in the static tests, these baseline curves were used to measure the reduction in flow function after injecting rust particles. Equations for the rotating baseline flow functions are provided in Appendix B. The baseline for the two coupons matched at  $\Omega = 0.002$ , which was anticipated since the controlling flow area was similar for the two coupons. At  $\Omega = 1$ , the flow area was reduced due to the increased outward radial force pressing the seal pins more closely against the test coupons. The resulting smaller flow area was responsible for the decrease in flow function at  $\Omega = 1$  relative to the  $\Omega = 0.002$  baseline. Coupons 1 and 2 had unique flow functions at  $\Omega = 1$  because of the difference in the shape of the contoured surface on the leading side of the seal pin. Recalling Figure 3.18, the smooth transition in coupon 2 guided the flow such that it passed more easily through the gap between the seal pin and the rough slot surface, resulting in an increased flow function compared with coupon 1 at  $\Omega = 1$ . In coupon 1, the lip on the leading side of the seal pin diverted flow away from the seal pin flow area. These effects were noticeable at  $\Omega = 1$  due to the increase in centrifugal and coriolis accelerations compared with the  $\Omega = 0.002$  case.

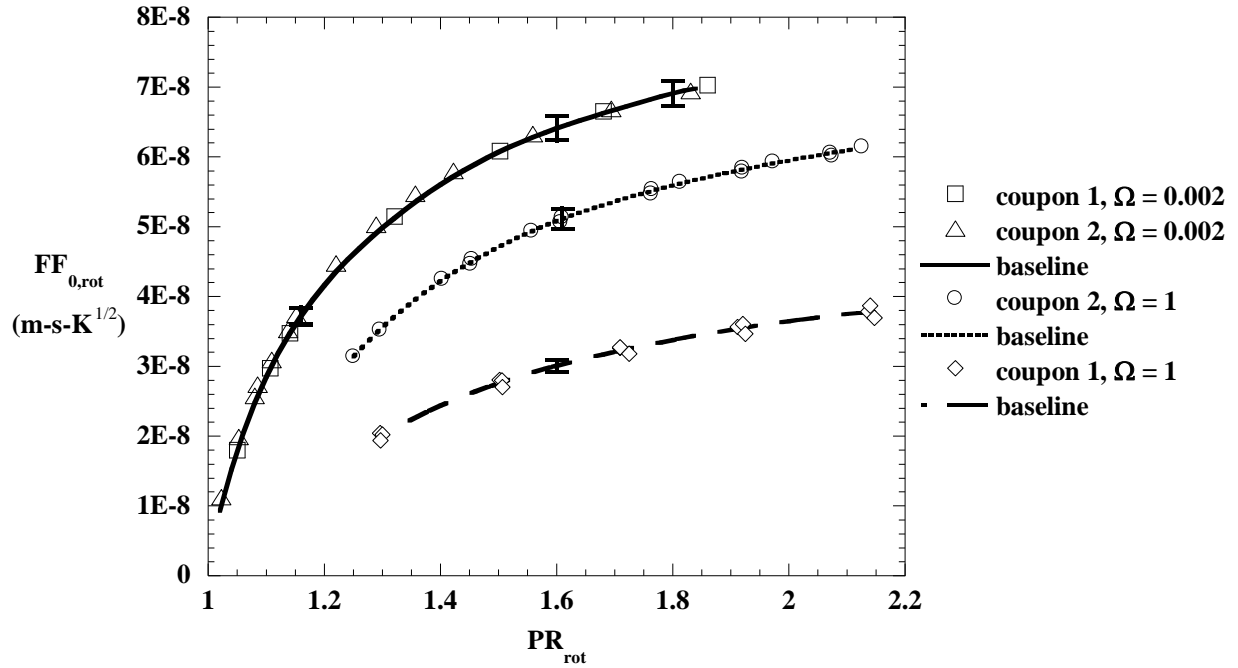


**Figure 3.27. Baseline flow functions for coupons 1 and 2 at  $\Omega = 0.002$  and  $\Omega = 1$  with three identical coupons open to flow.**

### 3.10 Comparison of Static Baseline and Predicted Flow Functions

As may be observed in Figure 3.28, the baseline and predicted flow function curves for static engine hardware do not match. One reason for the discrepancy is that the predicted flow function is based on assumed values for the flow area and discharge coefficient, as shown in Equation 3.16. If the assumed constant values for flow area and discharge coefficient were incorrect, the ratio of baseline to predicted flow function would be expected to be a constant value other than unity for all pressure ratios. Figure 3.29 illustrates the ratio of baseline to predicted flow function increases with pressure ratio from about 0.3 to 0.6 for pressure ratios ranging from 1.05 to 1.8, which implies either the flow area or the discharge coefficient varied with pressure ratio in the experiment. Since the flow area was fixed at a constant value regardless of pressure ratio, the increase in the ratio of flow functions with pressure ratio is attributed to variation in loss mechanisms with pressure ratio.

Recall that the discharge coefficient is used to account for losses due to non-isentropic effects, multi-dimensional flow effects, and reduction of the effective flow area due to boundary layer thickness; therefore variation in the discharge coefficient corresponds with variation in the relative magnitude of these physical loss mechanisms. For a typical nozzle with a well-designed

entrance, gradients in the radial direction outside the boundary layer are generally small and the assumption of one-dimensional flow holds. Additionally, the magnitude of the reduction in effective flow area due to boundary layer thickness is small relative to the large core of inviscid flow outside the boundary layer, so a typical nozzle operating at Reynolds numbers greater than  $10^5$  has a relatively constant discharge coefficient slightly less than unity over a range of flow conditions. The seal pin flow area is different from a typical nozzle in two key ways: 1) the entrance condition to the seal pin flow area varies from that of a well-designed nozzle; and 2) the seal pin flow area is much smaller than that of a typical nozzle. A closer look at the flow physics is necessary to understand why these differences cause the discharge coefficient to increase with pressure ratio.

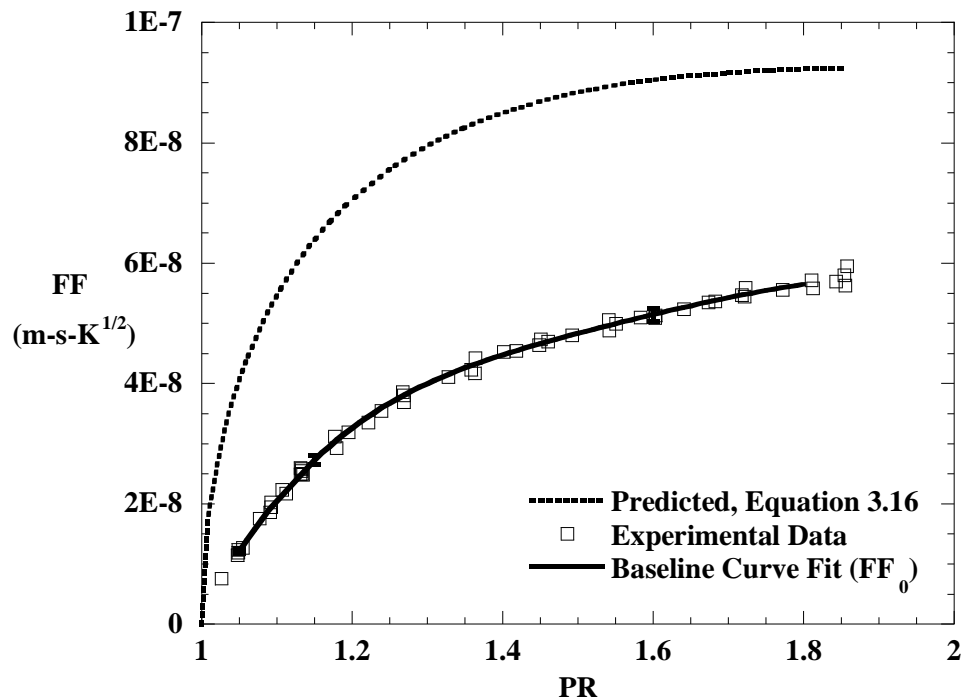


**Figure 3.28. Predicted flow function and experimental curve fit flow function for clean engine hardware, static tests.**

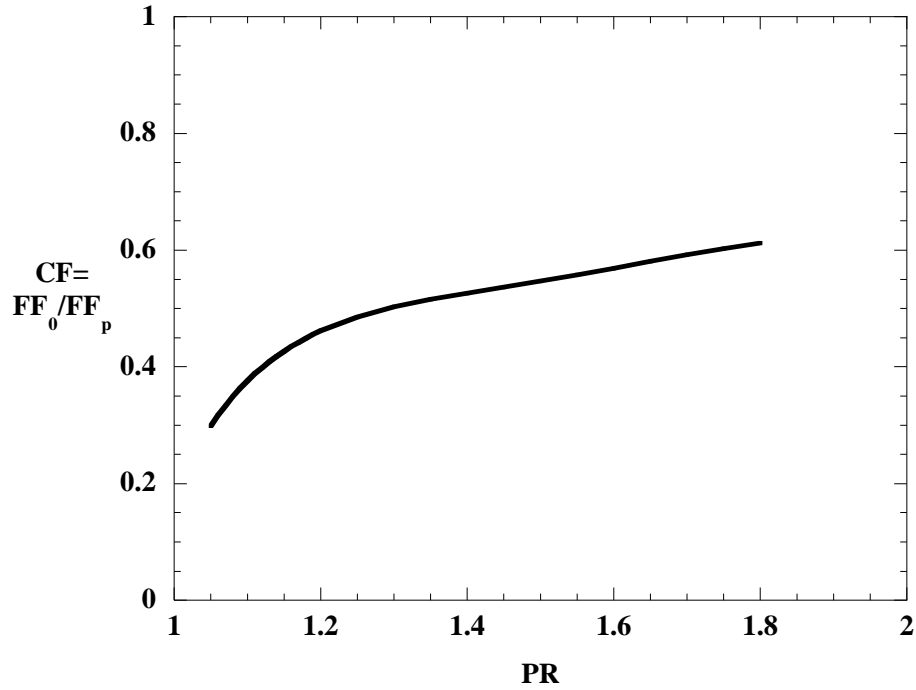


**Figure 3.29. The ratio of experimental to predicted flow functions varied with pressure ratio for the static tests.**

The effect of a non-ideal nozzle entrance condition is illustrated on the left-hand side of Figure 3.30. If the inlet angle  $\theta$  becomes too large, the flow gains momentum in the y-direction, resulting in multi-dimensional flow that narrows at some point beyond the exit plane of the nozzle. This narrowest flow area is called the vena contracta and may be considerably smaller than the throat area depending on the entrance condition. The vena contracta acts as an aerodynamic throat and reduces the flow rate from the anticipated value for isentropic flow based on the nozzle throat area, resulting in a larger than anticipated discharge coefficient. Furthermore, as discussed in [28-30], the area of the vena contracta increases with pressure ratio. This effect can be seen in Figure 3.30 by comparing the left and right schematics, which correspond to the low and high pressure ratio cases, respectively. Experimental results presented in [28] show that the area of the vena contracta increases most dramatically up to the critical pressure ratio and continues to increase until a pressure ratio of about  $P_0/p_b = 4.0$  is reached. A nozzle with a non-ideal entrance condition is therefore not fully choked at the critical pressure ratio  $P_0/p_b^* = 1.89$ .

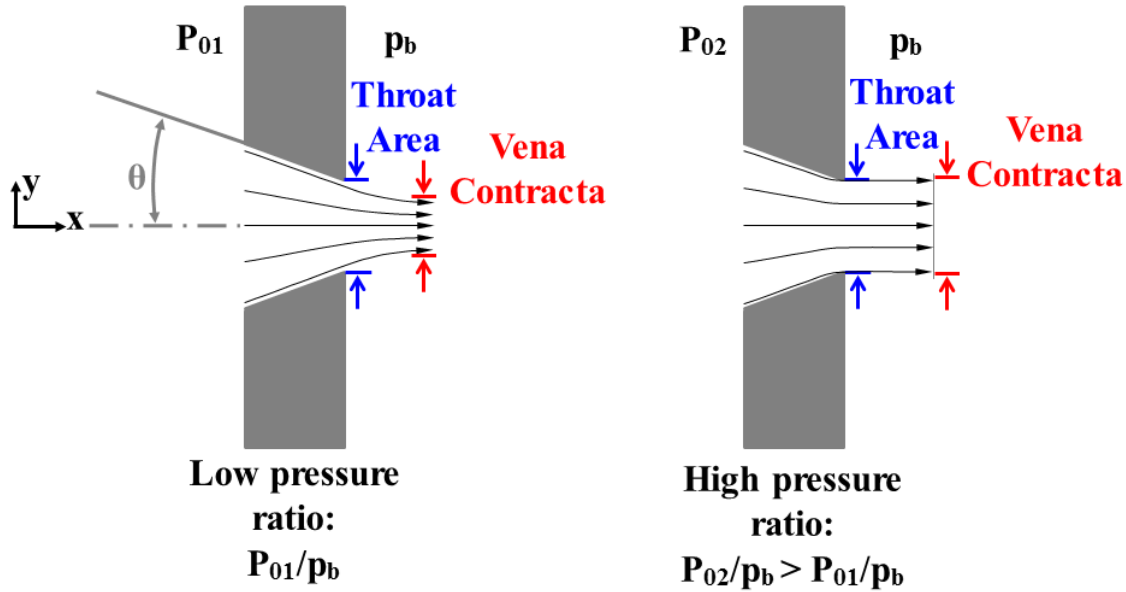


**Figure 3.30. Flow of gas through a nozzle with a non-ideal entrance condition; low and high pressure ratio cases [28].**

Recalling Figure 3.15, the seal pin leakage flow area was not designed with a particular focus on aerodynamics and may be considered as a nozzle with a non-ideal entrance condition. Though the simple explanation of the effects of sharp nozzle entrance angle presented in Figure 3.30 may not apply directly, flow through the seal pin area is likely to exhibit multi-dimensional flow effects such as the formation of a vena contracta. The experimentally observed increase in discharge coefficient with pressure ratio may be partially attributed to an increase in the size of the vena contracta. Additionally, consistent with the experimental results for nozzles with non-ideal entrance angles, the experimental baseline flow function shown in Figure 3.28 does not exhibit the fully choked condition as the critical pressure ratio of 1.89 is approached.

The small size of the seal pin flow area also contributed to the increase in discharge coefficient with pressure ratio. Consider that, as nozzle size decreases, the proportion of total flow area taken up by the boundary layer increases, making the reduction in effective flow area due to boundary layer displacement thickness more significant. The reduction in effective flow area results in a smaller discharge coefficient and increased sensitivity of the discharge coefficient to changes in boundary layer thickness. A smaller nozzle tends to have a lower throat Reynolds number and therefore a laminar boundary layer. From the Blasius solution for laminar boundary layer flow over a flat plate, the laminar boundary layer thickness is inversely proportional to the square root of the Reynolds number. This proportionality implies the

boundary layer thickness in a small nozzle must decrease with increasing Reynolds number, resulting in an increase in discharge coefficient to reflect the larger effective flow area outside the boundary layer.

Several experimental studies of small-diameter nozzles and orifices also reported variation of the discharge coefficient with either Reynolds number based on throat diameter or pressure ratio. An early study of compressible flow by Voss et al. [31] captured the variation in discharge coefficient for nozzle diameters less than 6.35 mm. They found the discharge coefficient decreased with Reynolds number, with the steepest decrease occurring for  $Re < 10^5$ , but it was evident that the Reynolds number was not the only controlling parameter. Previously discussed multi-dimensional effects that are dependent on pressure ratio also contributed to the decrease in discharge coefficient. Later studies further investigated compressible flow through even smaller diameter nozzles and orifices. For nozzles ranging from 0.259 mm to 2.39 mm diameter with a critical throat Mach number, Tang and Fenn [32] showed that the discharge coefficient decreased strongly with the throat Reynolds number, particularly for  $Re < 10^4$ . Kayser and Shambaugh [33] investigated subsonic compressible flow through orifices and converging nozzles ranging from 0.9 to 1.9 mm diameter. They found the discharge coefficient may correlate well with either the throat Reynolds number or the upstream total to downstream static pressure ratio depending on the design of the nozzle or orifice. For rounded or elliptical entry nozzles, they found the discharge coefficient dropped off sharply with Reynolds number for  $Re < 20,000$ .

For the present experiment, both the throat Reynolds number and Mach number varied with pressure ratio. The throat Mach number was calculated using Equation 2.4. Recalling Figure 3.15, the throat Reynolds number based on hydraulic diameter was calculated from Equation 3.26 for one of the two gaps between the seal pin and adjacent blade platforms. This calculation assumed the clearance gap was negligible compared to the seal pin length when calculating the wetted perimeter. Additionally, the assumption was made that the mass flow rate divided evenly between the two seal pin contact areas shown in Figure 3.15.

$$Re = \frac{\dot{m}}{L_{sp} \cdot \mu} \quad (3.26)$$

Over the range of pressure ratios from 1.05 to 1.8, the throat Reynolds number and Mach number varied from 30 to 300 and from 0.26 to 0.96, respectively. Since this Reynolds number

range is within the laminar flow regime, the trend of rapidly decreasing discharge coefficient with Reynolds number that was observed in [32] and [33] was expected. Recalling Figure 3.29, this trend is consistent with the observed decrease in the ratio of experimental to predicted flow function with pressure ratio.

At a particular pressure ratio, the ratio of flow functions given in Figure 3.29 may be used as a correction factor (CF) and multiplied by the predicted flow function as in Equation 3.27 to yield the flow function based on the experimental data. Furthermore, for a given upstream total temperature and total pressure, the mass flow rate through the seal pin flow area may be determined from the corrected flow function as shown in Equation 3.28.

$$FF = CF \cdot FF_p \quad (3.27)$$

$$\dot{m} = FF \cdot \frac{P_0}{\sqrt{T_0}} \quad (3.28)$$

Alternatively, it is possible to back-calculate from experimental data the value of the discharge coefficient multiplied by the area ( $C_D \cdot A$ ), commonly referred to as the effective flow area, using Equation 3.29. The discharge coefficient and area cannot be isolated from one another in the experimental data analysis since the small size of the seal pin flow area did not permit its independent measurement. The resulting curve of effective flow area versus pressure ratio is given in Figure 3.31.

$$C_D \cdot A = \frac{FF}{FP} \sqrt{R} \quad (3.29)$$

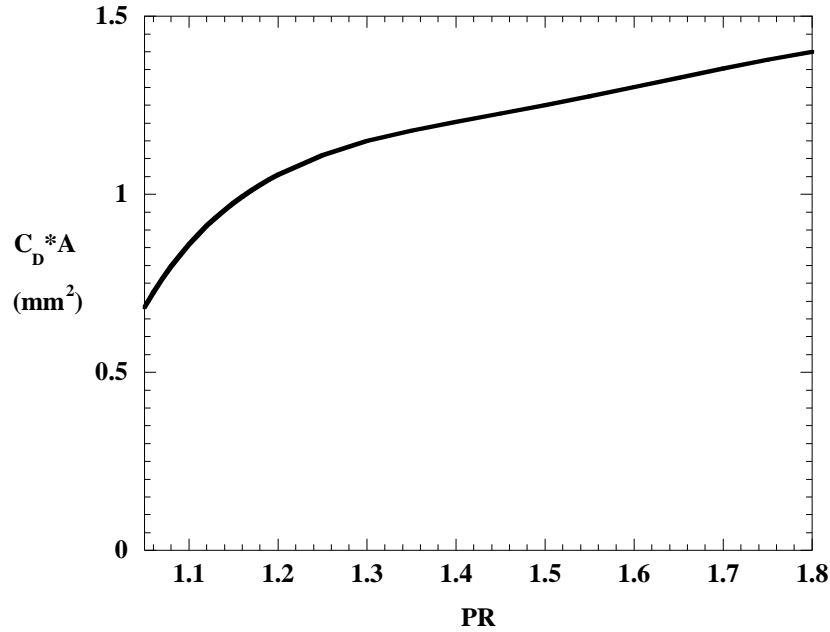


**Figure 3.31. Effective seal pin flow area as a function of pressure ratio for engine hardware.**

### 3.11 Comparison of Static and Rotating Baseline Flow Functions

The experimentally measured flow functions from the static and rotating tests are compared in Figure 3.32. Since the seal pin length in each test coupon part was nominally one-fourth of the engine hardware seal pin length, the baseline flow function curve for flow through three identical test coupons was scaled by a factor of four-thirds to correct for the smaller flow area. It is appropriate to compare the  $\Omega = 0.002$  data with the static data since the effect of rotation for the  $\Omega = 0.002$  case was relatively small. Recalling Table 3.8, the rotating coupons had seal pin slots machined similarly to plunge-EDM sample 4, which exhibited increased surface roughness compared with the engine hardware seal pin slot. The increased surface roughness widened the flow area between the slot and the seal pin, resulting in an increased flow function for the  $\Omega = 0.002$  tests relative to the static tests.

Also included in Figure 3.32 is a prediction based on one-dimensional analysis for flow through the coupons. Recalling Equation 3.3, the seal pin clearance  $t_{sp}$  was approximated as  $33.6 \mu\text{m}$ , which was the height above surface parameter given in Table 3.8 for plunge-EDM sample 4. The engine hardware seal pin length of 110 mm was used, yielding a seal pin flow area  $A_{sp} = 3.70 \text{ mm}^2$ . A discharge coefficient of 0.6 was used since the seal pin flow area was previously shown to exhibit multi-dimensional flow effects similar to a sharp-edged orifice [34]. As with



the static tests, the one-dimensional approximation did not exactly match the experimental data. This discrepancy was largely due to losses resulting from the small size of the flow area and multi-dimensional flow effects, neither of which was accounted for in the one-dimensional approximation. In addition, the height above surface parameter used to calculate the flow area for the predicted curve was only an approximation. Recalling Figure 3.15, this parameter did not account for the gap between the seal pin and the trailing (flat) half of the test coupon, and the parameter was measured on a sample machined similarly to the test coupon slot surface but not on the actual test coupon.

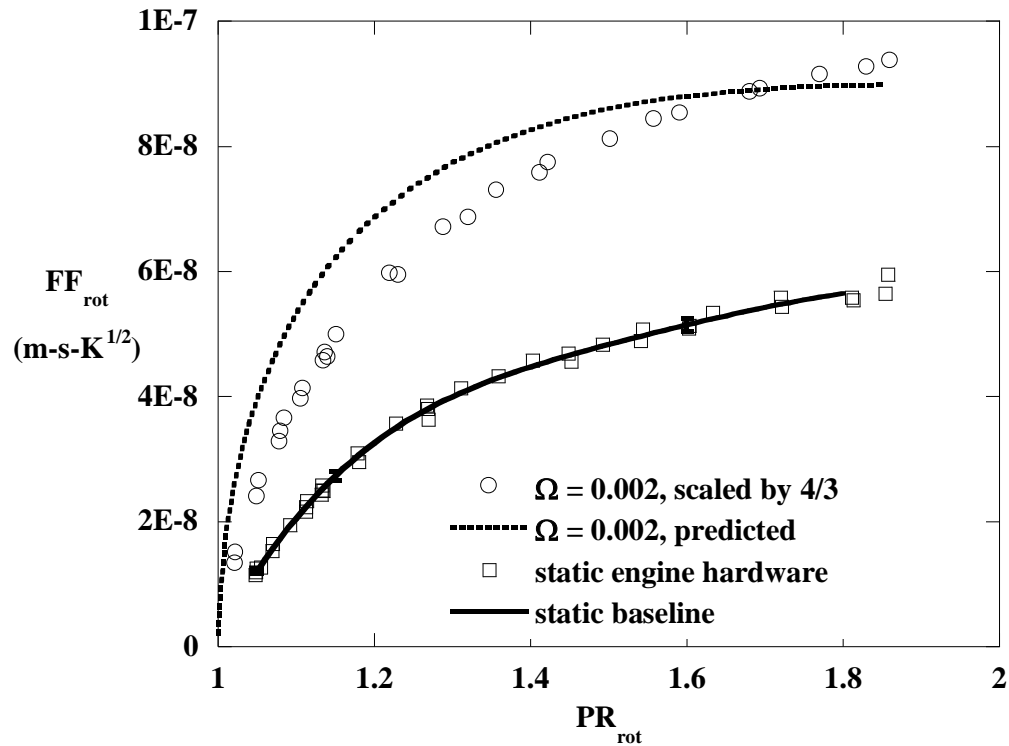


**Figure 3.32. Comparison of scaled rotating coupon flow function with full-scale static engine hardware.**

### 3.12 Derivation of Test Matrices

A test matrix for the static engine hardware tests, shown in Table 3.9, was developed to investigate the effects of injecting various amounts of rust at pressure ratios representative of engine conditions. Based on engine coolant and main gas flow pressures typical for gas turbine blades, the pressure ratio across the axial seal pin is expected to vary between 1.05 and 1.6 along the length of the pin. Three pressure ratios spanning this range, namely 1.05, 1.15, and 1.6, were selected for testing.

Rust amounts for each pressure ratio were chosen around mean mass loading ratio (rust mass divided by air mass flow rate) of 0.50 s based on the mass loading ratio of sand (sand mass divided by air mass flow rate) found in [15] through particle injection experiments to yield blockages similar to what was observed in field-run jet engine hardware. Though there is no expected direct correlation between sand ingestion in jet engines and rust ingestion in land-based engines, the data from sand testing with jet engine hardware was referenced as a base for the current test matrix since no quantitative information regarding rust particle ingestion in land-based turbines was available. While a concentration ratio such as the rust mass flow to air mass flow rate would have been preferable due to its dimensionless form, the method of near instantaneous injection of a mass of rust particles made defining the particle flow rate impractical.

**Table 3.9. Test Matrix for Static Tests**

PR	$m_{\text{rust}}$ (g)	$\text{MLR} = m_{\text{rust}} / \dot{m}_{\text{air}}$ (s)
1.05	0.018	0.25
	0.039	0.54
	0.054	0.75
	0.13	1.8
	0.23	3.2
1.15	0.039	0.22
	0.089	0.5
	0.13	0.72
	0.23	1.3
	5.3	N/A
1.6	0.039	0.08
	0.13	0.27
	0.23	0.5
	0.35	0.75

An additional static rust injection test was performed in which a total of 5.3 g of rust was cumulatively injected in several smaller quantities. The purpose of this test was twofold: 1) to attempt a complete blockage of the seal pin flow area; and 2) to compare the blockage effects for a given rust mass injected as a single amount with those for the same mass injected cumulatively in several smaller amounts.

Shown in Table 3.10, a second test matrix was developed for the rotating study to investigate the effects of rotating speed and flow geometry on rust deposition and flow blockage.  $\Omega = 1$  corresponds with matching the centrifugal acceleration in the engine. Tests were performed at pressure ratios of 1.15, 1.6, and 1.8. Injecting rust amounts with a mass loading ratio of about 0.5 s resulted in negligible flow blockage, so the rust amounts were increased to yield flow blockage similar to what was observed in the static tests. The mass loading ratio for the rotating tests ranged from 0.6 to 28 s at  $\Omega = 0.002$ . At  $\Omega = 1$ , the mass loading ratio varied from 6.1 to 26 s for coupon 1 and from 3.5 to 15 s for coupon 2.

**Table 3.10. Test Matrix for Rotating Tests**

Coupon	$\Omega$	$PR_{rot}$	$m_{rust}$ (g)
1	0.002 (500 rpm)	1.15	8.0
		1.6	8.0
		1.8	8.0
	1 (10,300 rpm)	1.6	8.0
2	0.002 (500 rpm)	1.6	8.0
	1 (10,300 rpm)		8.0

Each particle injection test for a given pressure ratio and injected rust mass was repeated a minimum of three times to insure repeatability of the blockage. After performing a 25-test repeatability study, Walsh et al. [15] concluded three repetitions of each test optimized testing efficiency and yielded repeatable reductions in flow function to within 7%. For the static tests, a 15-case repeatability study performed for  $PR = 1.15$  and  $m_{rust} = 0.089$  g showed three repetitions of each test yielded reductions in flow function to within 9%. In the rotating facility, each rust injection test measured the flow blockage through three identical test coupons. For statistical analysis, the flow blockage from each test in the rotating facility was considered to be an average of three tests. Analysis of 9 rotating tests (3 tests of 3 parts each) indicated the reduction in flow function was repeatable to within 7%. The rotating tests analyzed were for coupon 2 at  $\Omega = 0.002$ , with 8.0 g total injected rust at  $PR_{rot} = 1.6$ . All repeatability results are reported for a 95% confidence interval.

### 3.13 Uncertainty Analysis

Uncertainty analysis of experimentally measured parameters was performed using the partial derivative method as described by Beckwith et al. [35]. Results shown in Table 3.11 give nominal parameter values and their respective uncertainties for the static tests. Uncertainty in flow function was 2.1% to 3.1% and was mainly driven by bias uncertainties in the pressure and temperature measurements at the LFE. For pressure ratios of 1.05, 1.15, and 1.6, uncertainties in the reduction in flow function were 23%, 10%, and 3.9%, respectively. Both the flow function and reduction in flow function uncertainties increased as pressure ratio decreased due to the constant instrument bias uncertainties relative to the smaller nominal values of FF and RFF. For  $PR = 1.15$ , the measurement uncertainty of 10% was greater than the previously discussed 9% uncertainty due to measurement repeatability, so therefore performing three repetitions of each test was sufficient to minimize uncertainty for the given measurement equipment. Further details of the static uncertainty calculations are provided in Appendix C.

**Table 3.11. Parameter Nominal Values and Uncertainties for Static Tests**

	Range	% of Measured Value	Range	% of Measured Value	Range	% of Measured Value
<b>PR</b>	$1.05 \pm 0.001$	0.09	$1.15 \pm 0.003$	0.25	$1.59 \pm 0.011$	0.69
<b><math>\dot{m}</math> (kg/s)</b>	$7.15\text{E-}05 \pm 1.70\text{E-}06$	2.4	$1.77\text{E-}04 \pm 3.42\text{E-}06$	1.9	$4.63\text{E-}04 \pm 7.02\text{E-}06$	1.5
<b>FF (m-s-K<sup>1/2</sup>)</b>	$1.21\text{E-}08 \pm 3.74\text{E-}10$	3.1	$2.74\text{E-}08 \pm 7.28\text{E-}10$	2.7	$5.19\text{E-}08 \pm 1.09\text{E-}09$	2.1
<b>RFF</b>	$13\% \pm 3.1\%$	23	$22\% \pm 2.3\%$	10	$37\% \pm 1.4\%$	3.9
<b><math>m_{\text{rust}}</math> (g)</b>	$0.039 \pm 0.001$	2.6	$0.089 \pm 0.001$	1.1	$0.232 \pm 0.001$	0.43

Uncertainties of parameters in the rotating study are provided for  $\Omega = 0.002$  and  $\Omega = 1$  tests in Table 3.12 and Table 3.13, respectively. At  $\Omega = 0.002$ , the parameter nominal values for coupons 1 and 2 were similar since both the baseline flow function and the reduction in flow function were similar for both coupons. Uncertainty in the flow function was 2.6% to 3.2% and was driven primarily by the bias uncertainty in the temperature measurement at the LFE. Uncertainty for the reduction in flow function varied from 6.1% to 32% and decreased with increasing flow blockage. For tests performed at  $\Omega = 0.002$  and  $PR_{\text{rot}} = 1.6$ , the measurement uncertainty for the reduction in flow function was 9%. Compared with the repeatability of 7%, this uncertainty indicates performing three tests with three identical test coupons each was

sufficient to minimize uncertainty within the limitations of the equipment. Further details of the uncertainty analysis for the rotating tests are provided in Appendix D.

**Table 3.12. Parameter Nominal Values and Uncertainties for Tests at  $\Omega = 0.002$**

	Range	% of Measured Value	Range	% of Measured Value	Range	% of Measured Value
$\omega$ (rpm)	$514 \pm 3$	0.5	$518 \pm 3$	0.5	$501 \pm 3$	0.6
$PR_{rot}$	$1.14 \pm 0.02$	1.6	$1.60 \pm 0.02$	1.1	$1.80 \pm 0.02$	1.0
$FF_{rot}$ (m-s-K <sup>1/2</sup> )	$3.64E-08 \pm 1.18E-09$	3.2	$6.48E-08 \pm 1.78E-09$	2.8	$6.94E-08 \pm 1.81E-09$	2.6
RFF	$21\% \pm 6.6\%$	32	$24\% \pm 2.2\%$	9.2	$17\% \pm 2.2\%$	13
$m_{rust}$ (g)	$8.034 \pm 0.003$	0.04	$8.014 \pm 0.002$	0.03	$8.013 \pm 0.002$	0.03

**Table 3.13. Parameter Nominal Values and Uncertainties for Tests at  $\Omega = 1$**

	Coupon 1		Coupon 2	
	Range	% of Measured Value	Range	% of Measured Value
$\omega$ (rpm)	$10342 \pm 2$	0.02	$10302 \pm 2$	0.02
$PR_{rot}$	$1.61 \pm 0.02$	1.3	$1.61 \pm 0.02$	1.3
$FF_{rot}$ (m-s-K <sup>1/2</sup> )	$3.20E-08 \pm 9.48E-10$	3.0	$5.22E-08 \pm 1.53E-09$	2.9
RFF	$22\% \pm 2.6\%$	12	$35\% \pm 2.1\%$	6.1
$m_{rust}$ (g)	$8.017 \pm 0.002$	0.02	$8.009 \pm 0.002$	0.02

## **Chapter 4. RESULTS FROM STATIC TESTS**

This chapter includes results from the particle characterization study and from tests performed using the static test facility. From the particle characterization study, the effects of separate particle heating and centrifuging experiments are presented. Results from the static test facility include tests with clean air flow and tests with rust particle-laden flow. An assessment of the sensitivity to the rust injection method is included along with a general description of observed rust deposition. Results from particle injection tests are presented, and the effects of rust mass, mass loading ratio, and pressure ratio are discussed. An additional particle injection test designed to achieve the maximum possible blockage is also discussed.

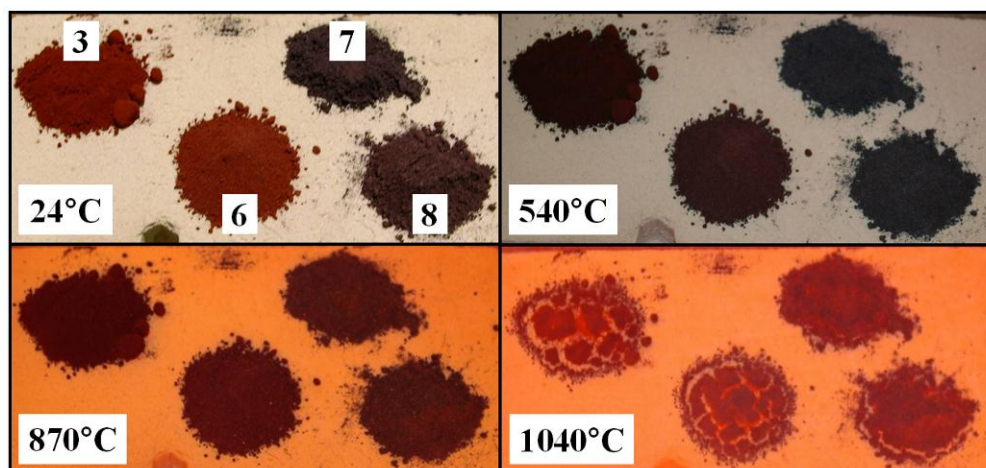
### **4.1 Effect of Heating**

Particles of various compositions were heated in a kiln to observe the influence of turbine representative temperatures, and the effects of particle composition and temperature were assessed. Summarized in Table 4.1, a first series of heated tests was performed on oxide compounds comprised of sand ( $\text{SiO}_2$ ), black iron oxide ( $\text{Fe}_2\text{O}_3$ ), red iron oxide ( $\text{Fe}_2\text{O}_3$ ), and aluminum oxide ( $\text{Al}_2\text{O}_3$ ).

Independent of composition, particles conglomerated and began turning darker in color at approximately  $950^\circ\text{C}$ . Red iron oxide particles turned black between  $954^\circ\text{C}$  and  $1093^\circ\text{C}$ , which indicated a phase change. As noted in tests 2e and 3e, both red and black iron oxide became brittle above  $954^\circ\text{C}$ , probably as a result of particles beginning to melt. Figure 4.1 illustrates the observed changes to particles of various mixtures including red and black iron oxide. The most noticeable changes occurred for red iron oxide, which tended to form the largest clumps and underwent a color change from bright red to brown/grey after being heated to  $1040^\circ\text{C}$ . When particles conglomerated during heating, it was possible to break up the agglomerations after the particles cooled to room temperature.

**Table 4.1. Particle Heating Tests for Samples of Various Compositions**

Sample Composition	Test	Kiln Temperature (°C)	Exposure Time (min.)	Observations
100% Sand	1	1010	0	Conglomerated, darker
100% Black Fe <sub>2</sub> O <sub>3</sub>	2a	538	30	Unchanged
	2b	816	0	Unchanged
	2c	816	30	Did not cling to surface, darker
	2d	954	30	Began forming clumps, darker
	2e	1093	30	Conglomerated, completely black, brittle
100% Red Fe <sub>2</sub> O <sub>3</sub>	3a	538	30	Unchanged
	3b	816	30	Unchanged
	3c	954	30	Began forming clumps, slightly darker, did not cling to surface
	3d	1093	30	Black
	3e	1052	0	Conglomerated, dull black, brittle
100% Al <sub>2</sub> O <sub>3</sub>	4	816	0	Unchanged
50% Red Fe <sub>2</sub> O <sub>3</sub> , 50% Black Fe <sub>2</sub> O <sub>3</sub>	5a	538	30	Unchanged
	5b	816	30	Clings less to surface
	5c	954	30	Began forming clumps, darker, did not cling to surface
	5d	1093	30	Sample contaminated
90% Red Fe <sub>2</sub> O <sub>3</sub> , 10% Al <sub>2</sub> O <sub>3</sub>	6a	538	30	Unchanged
	6b	816	30	Unchanged
	6c	954	30	Darker, clings less to surface
	6d	1052	0	Conglomerated, somewhat red, brittle, more dense
	6e	1093	30	Turned dark red
90% Black Fe <sub>2</sub> O <sub>3</sub> , 10% Al <sub>2</sub> O <sub>3</sub>	7	1052	0	Conglomerated, black, speckled
45% Red Fe <sub>2</sub> O <sub>3</sub> , 45% Black Fe <sub>2</sub> O <sub>3</sub> , 10% Al <sub>2</sub> O <sub>3</sub>	8	1052	0	Conglomerated, dull black, speckled

**Figure 4.1. Metal oxide particles shown initially and at various temperatures during heating (Sample numbers correspond to test numbers in Table 4.1.).**

A second series of heated tests, summarized in Table 4.2, was performed on metal oxide mixtures that were representative of particle compositions found in field-run turbines (recall Table 3.1). These tests investigated the effects of particle composition, temperature, and exposure time. For mixtures 1 and 2, conglomeration and color change were observed at temperatures above 816°C and 850°C, respectively, however, mixtures 3, 4, and 5 exhibited negligible changes in appearance when heated to 850°C and exposed for various time periods. Mixture 5 particles are shown in Figure 4.2 before and after heating to 850°C.

**Table 4.2. Particle Heating Tests for Engine Representative Compositions**

Sample	Test	Kiln Temperature (°C)	Exposure Time (min.)	Observations
Mixture 1	9a	Ambient	N/A	Red powder, clingy
	9b	954	0	Datum
	9c	954	30	Increased clumping
	9d	954	60	Increased clumping
	9e	954	120	Increased clumping
	9f	816	0	Datum
	9g	816	30	Orange/red
	9h	816	60	Unchanged from 9g
	9i	816	120	Unchanged from 9g
	9j	1093	0	Minor conglomeration, brown/red
	9k	1093	30	Increased conglomeration, dark brown
	9m	1093	60	Increased conglomeration, dark brown/black
	9n	1093	120	Increased conglomeration, black
Mixture 2	10a	Ambient	N/A	Red powder, clingy
	10b	850	0	Orange/red
	10c	850	30	Increased conglomeration, orange/red
	10d	850	60	Increased conglomeration, orange/red
	10e	850	120	Increased conglomeration, orange/red
Mixture 3	11a	Ambient	N/A	Pink powder, clingy
	11b	850	0	Slightly increased conglomeration, light brown
	11c	850	30	Unchanged from 11b
	11d	850	60	Unchanged from 11b
	11e	850	120	Unchanged from 11b
Mixture 4	12a	Ambient	N/A	Pink powder, clingy
	12b	850	0	Light brown
	12c	850	30	Unchanged from 12b
	12d	850	60	Unchanged from 12b
	12e	850	120	Unchanged from 12b
Mixture 5	13a	Ambient	N/A	Very red (iron oxide predominates the colors)
	13b	850	0	Slightly deeper red
	13c	850	30	Unchanged from 13b
	13d	850	60	Unchanged from 13b
	13e	850	120	Unchanged from 13b



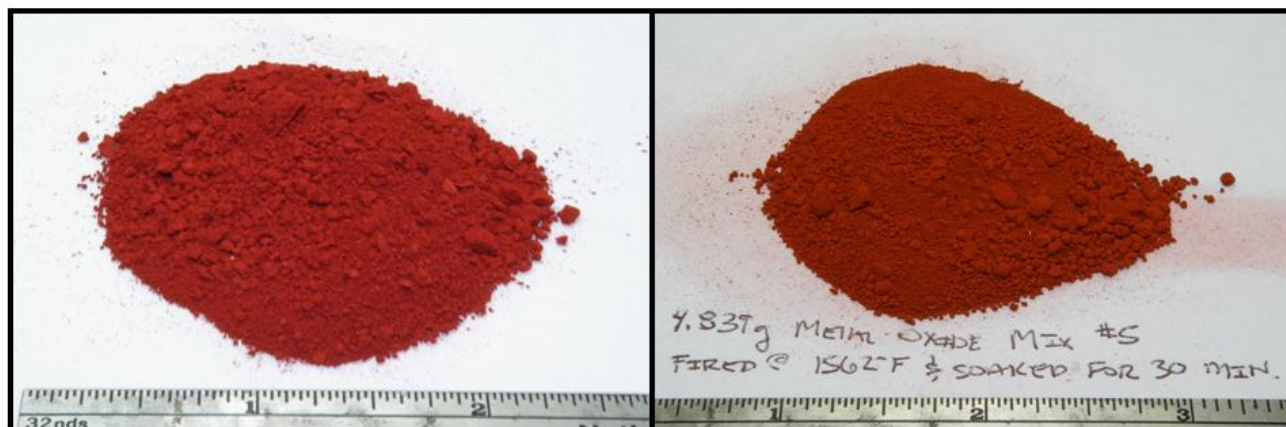


**Figure 4.2. Visual comparison of unheated mixture 5 particles (left) with particles heated to 850°C (right), scale in inches.**

To investigate the effects of temperature and exposure time on a micro scale, particle size analysis by laser diffraction was performed on unheated and heated samples of mixture 5 particles. Shown in Figure 4.3, particle size was found to increase considerably with heating temperature, particularly from 850°C to 950°C. While the unheated particle size distribution contained particles ranging from submicron to nearly 1000  $\mu\text{m}$ , the volume percentage of particles larger than 100  $\mu\text{m}$  was greatly increased for the sample heated to 950°C. Particle size was also found to increase slightly with heating time. In mixture 5 samples heated to 850°C, varying the heating time from 0 to 120 minutes yielded a small right-ward shift in the particle size distribution, shown in Figure 4.4. Particles located at the center of the sample required more time to heat to the kiln temperature and thus only experienced the effects of increased temperature after a longer heating time.

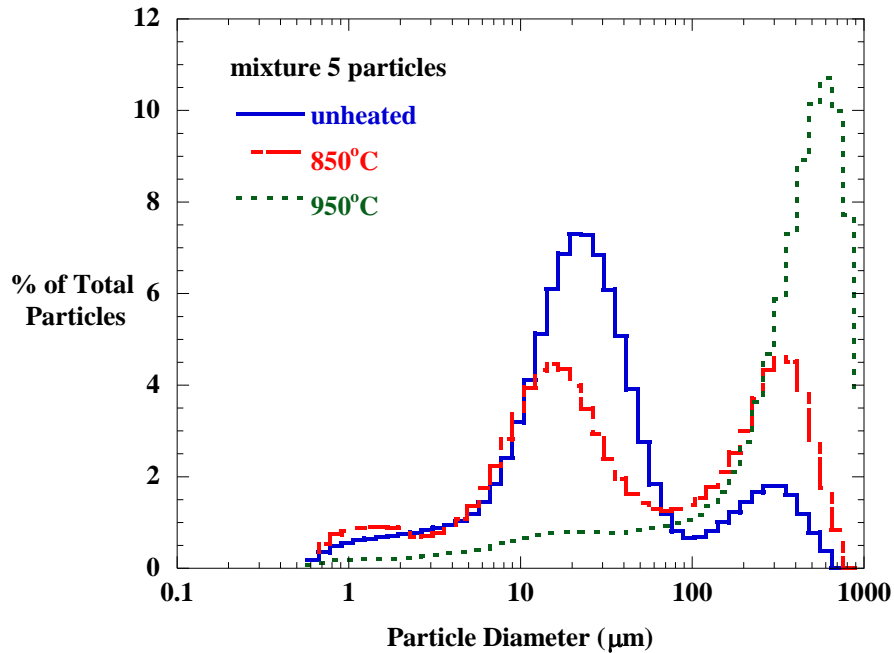


**Figure 4.3. Size distributions for unheated and heated particles. Particle size tests were performed at ambient conditions following heating.**

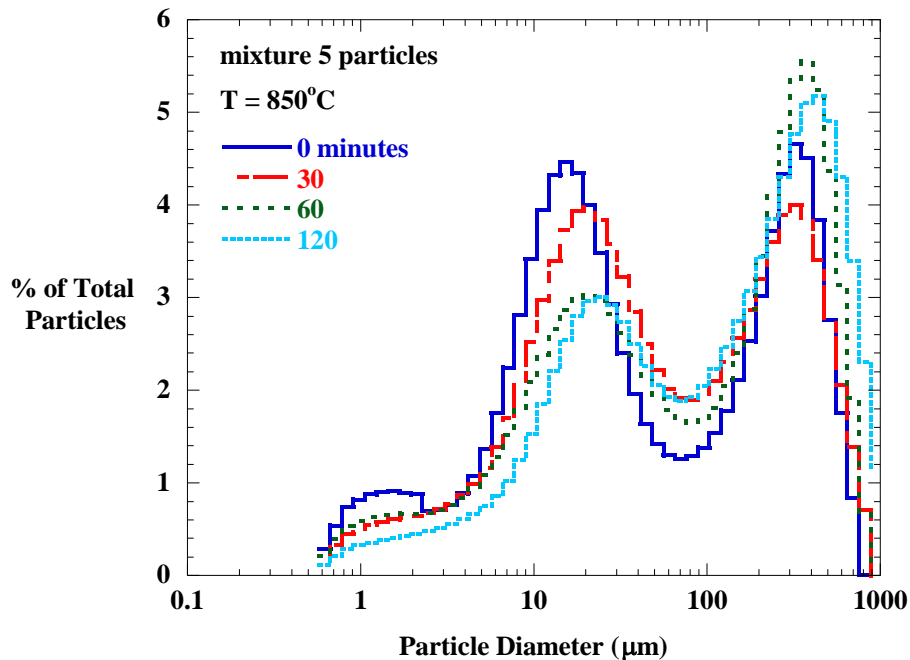


**Figure 4.4. Size distributions for particles heated for varying lengths of time.**

## 4.2 Effect of Centrifugal Forces

A summary of the centrifuge tests is provided in Table 4.3. The major finding from the centrifuge tests was that particles conglomerated into a lumped mass and adhered to the outer

side of the centrifuge sample tube. After centrifuging, it was possible to turn the tube in all positions without the compacted mass of particles coming loose from the side of the tube wall. To remove particles from the sample tube, it was necessary to vigorously strike the tube on a solid surface in order to break the compacted mass of particles into smaller pieces. Figure 4.5 shows particles before and after removal from the sample tube. Large pieces of compacted particles were present even after removal from the tube. Sample bulk density was used to characterize the degree of compaction. The volume occupied by a sample of known mass was measured before and after centrifuging to determine the loose and compacted bulk densities,  $\rho_l$  and  $\rho_c$ , respectively. Irrespective of particle composition, sample mass, and prior heat treatment, the density ratio ( $\rho_c/\rho_l$ ) was determined to be about 2 for all tests in which particle bulk density was measured.

**Table 4.3. Particle Centrifuging Tests**

Sample	$\Omega$	Test	Mass (g)	Density Ratio ( $\rho_c/\rho_l$ )	Prior Heat Treatment
Mixture 5	6.1 (25,000 rpm)	1	4.84	2.2	Heated to 850°C for 0 min.
		2	4.84		Heated at 850°C for 30 min.
		3	4.87		Heated at 850°C for 60 min.
		4	4.64		Heated at 850°C for 120 min.
		5	4.80		None
		6	4.79		None
		7	9.98		None
		8	9.97		None
		9	20.0		None
		10	20.0		None
		11	30.0		None
		12	30.0		None
100% Fe <sub>2</sub> O <sub>3</sub>	1 (10,000 rpm)	13	10.0	2.2	Heated at 150°C for 4 hours
		14	10.0	2.2	Heated at 150°C for 4 hours
		15	10.0		None
		16	10.0		None
Mixture 5	1 (10,000 rpm)	17	10.0	2.2	Heated at 150°C for 4 hours
		18	10.0	2.2	Heated at 150°C for 4 hours
		19	10.0		None
		20	9.90		None

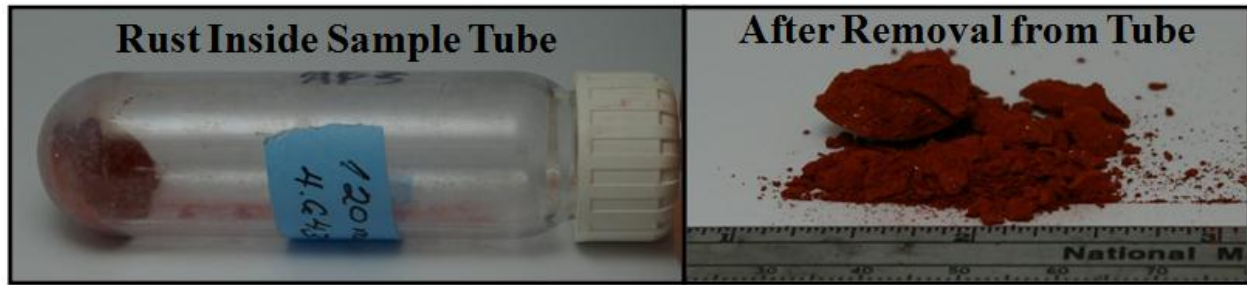


**Figure 4.5. Centrifuged particles shown before and after removal from the centrifuge tube.**

### **4.3 Effect of Rust Injection on Engine Hardware**

Substantial quantities of injected rust particles were deposited in the blade platform area upstream of and at the seal pin slot, as shown in Figure 4.6 and Figure 4.7. After performing a particle injection test, it was possible to reclaim deposited rust particles by brushing them from the seal pin area and upstream blade platform surfaces. Comparing the mass of the reclaimed particles with the injected mass showed that about 80% of the injected rust mass was deposited at the seal pin area and the upstream blade platform surfaces. The percentage of reclaimed rust was relatively insensitive to the pressure ratio at which the rust was injected. For a rust mass of 0.23 g, increasing the pressure ratio from 1.05 to 1.6 yielded only a small decrease in the percent of reclaimed particles, from 81% to 76%.

Two factors resulted in a large percentage of injected particles being deposited on the blade platform and seal pin surfaces. First, the geometric size of the seal pin clearance gap did not permit the largest particles to pass through the seal pin area. Though shown in experimental results to be somewhat large, the assumed value of 25.4  $\mu\text{m}$  for the seal pin clearance gap is appropriate for a scale comparison with the particle size. Recalling Figure 3.1, the sizes of injected rust particles ranged from submicron to nearly 1000  $\mu\text{m}$ , so therefore the largest injected rust particles were an order of magnitude larger than the seal pin gap and were unable to pass through the gap. The second factor influencing deposition was ballistic behavior of particles, which is subsequently discussed.

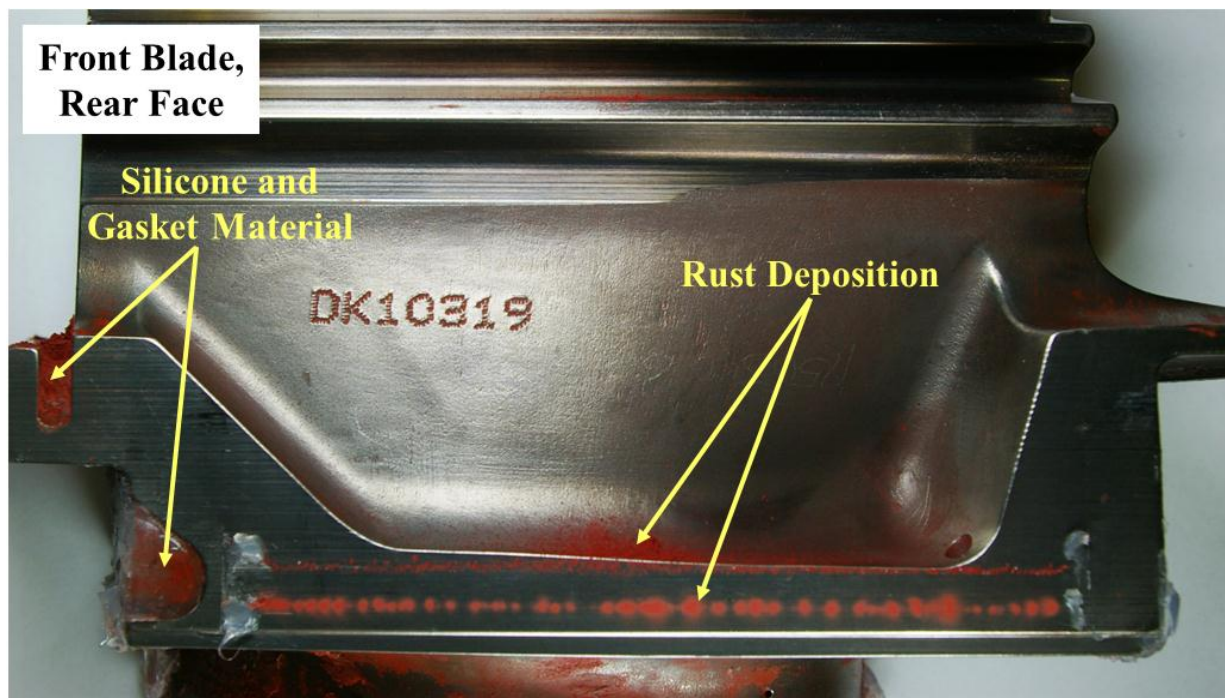


Figure 4.6. Rust deposits on the rear face of the front blade after injecting 0.23 g of rust.

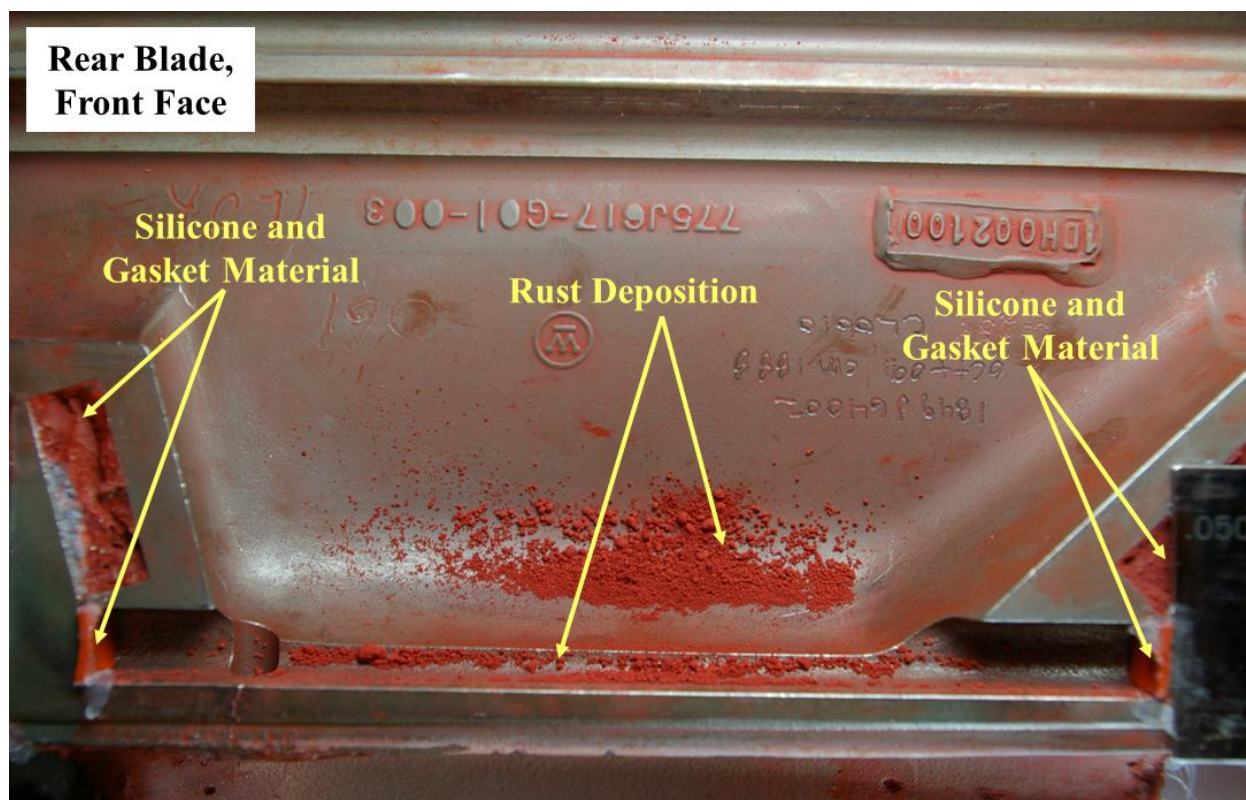
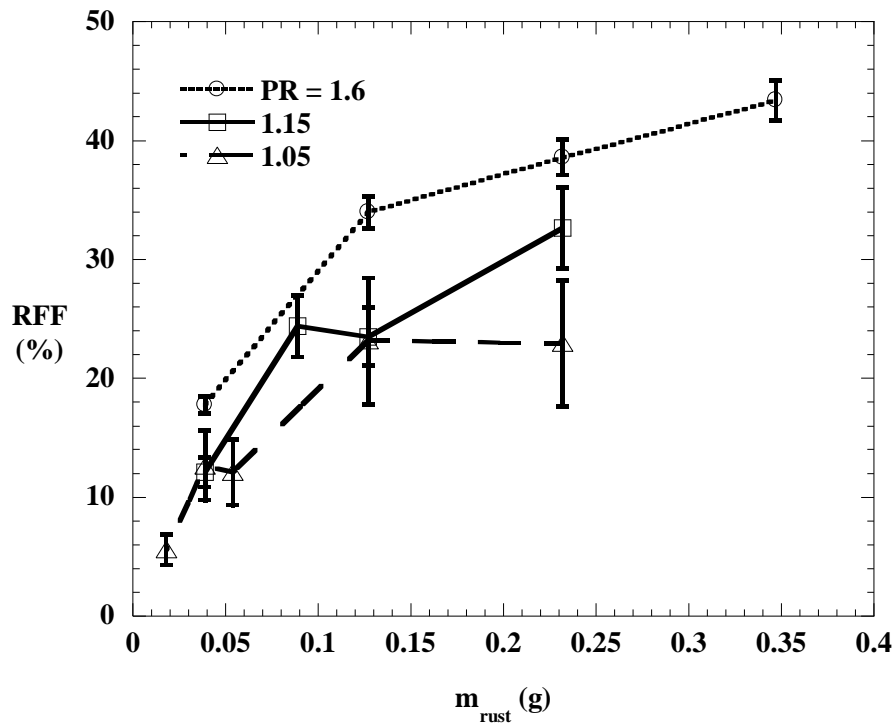


Figure 4.7. Rust deposits on the front face of the rear blade after injecting 0.23 g of rust; shown after removing the seal pin.



Results from particle injection experiments were analyzed in several different ways to examine the effects of rust amount, mass loading ratio, and pressure ratio on flow blockage. The effects of rust amount and mass loading ratio for three pressure ratios are shown in Figure 4.8 and Figure 4.9, respectively. Blockage ranged from 5% to 43% RFF and increased with total injected rust mass and with mass loading ratio for injected rust masses ranging from 0.018 g to 0.35 g and mass loading ratios ranging from 0.08 s to 3.2 s. As the injected rust mass was increased, more particles were available for inertial impaction and deposition in the seal pin area, resulting in greater reduction in the flow area and increased blockage.



**Figure 4.8. Blockage versus injected rust mass for three pressure ratios.**

Recall that the mass loading ratio is defined as the ratio of injected rust mass to air mass flow rate and as such is proportional to the particle concentration. Since the air mass flow rate was constant for clean conditions at a given pressure ratio, an increase in mass loading ratio corresponded directly to an increase in rust mass. It was therefore not possible to completely isolate the effect of increasing rust mass from that of increasing mass loading ratio, and the similarity in the trends shown in Figure 4.8 with those in Figure 4.9 was anticipated.

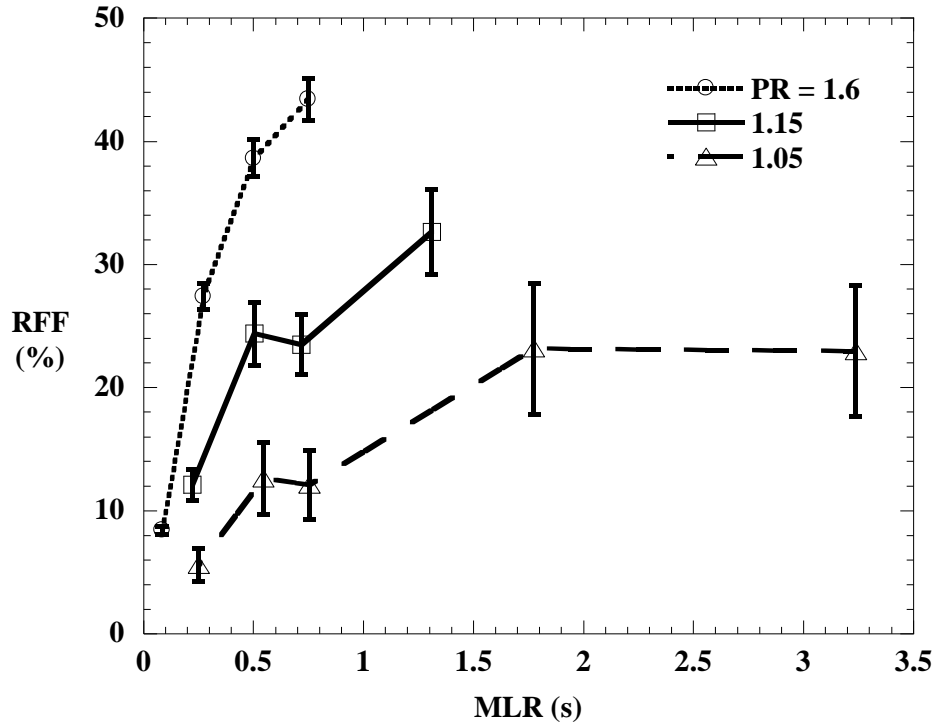


**Figure 4.9. Blockage versus rust mass to air mass flow rate ratio for three pressure ratios.**

As noted in Chapter 1, rust deposition in an engine typically occurs over a short period of time after engine startup. Upon engine startup, the concentration of rust is initially a maximum and gradually decreases with time as rust particles are removed from the cooling air flow and deposited in the engine or in filters [5]. The experiments considered here all involved injecting a quantity of rust particles almost instantaneously into air flow through the seal pin area and thus were not exactly representative of the decaying particle concentration experienced in an engine.

To determine whether blockage at the seal pin area is sensitive to the rust delivery method, two types of tests were performed for comparison of rust delivery methods. In the first type of test, several rust amounts totaling a given mass were injected cumulatively, and blockage was measured after each successive rust injection. The second type of test involved injecting the same given rust mass as a single quantity and subsequently measuring the blockage. Figure 4.10 shows the comparison between these two types of tests. When uncertainty is taken into account, cumulative and single-quantity rust injection yielded similar blockages for the same total injected rust mass. This finding indicates blockage was strongly dependent on the total injected particle mass, and therefore the deposition and blockage observed in experiments is representative of that

occurring in an engine even though the means of particle ingestion were different. Previous deposition studies by Kim et al. [10] and Cardwell et al. [17] also reported blockage was dependent on the total mass of particles injected.

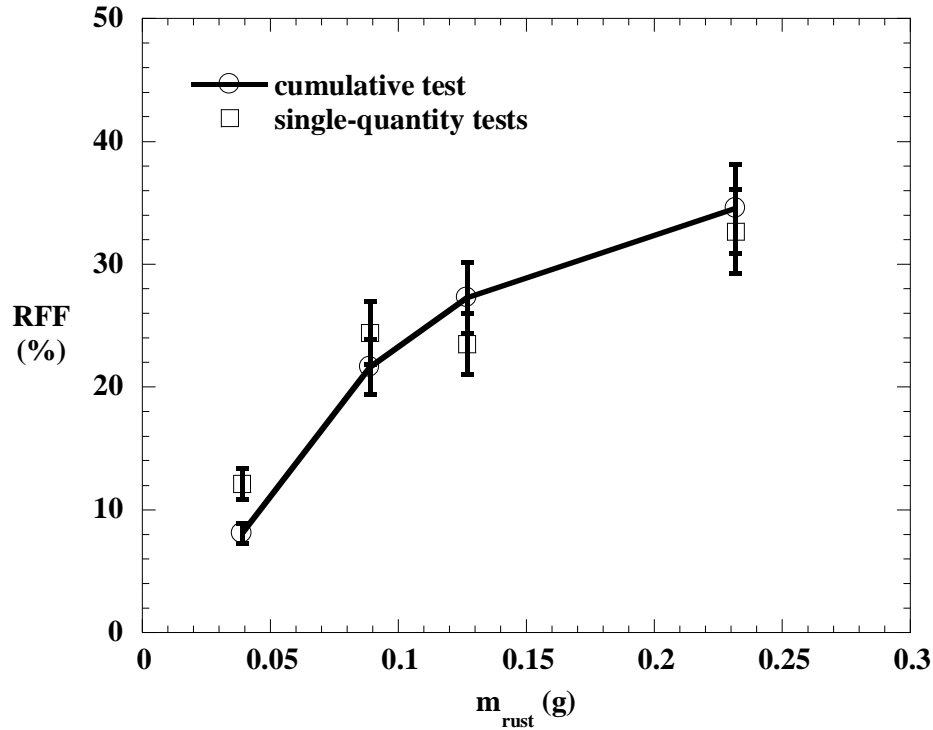


**Figure 4.10. Comparison of single-quantity and cumulative rust injection tests performed at a pressure ratio of 1.15.**

As shown in Figure 4.11, blockage increased with pressure ratio for a given rust amount. It was previously noted that inertial effects dominate the motion of particles larger than about 1  $\mu\text{m}$ . The increased fluid velocities associated with higher pressure ratios inhibited the particles' ability to follow the flow streamlines, resulting in more impacts with the engine hardware which lead to increased deposition and greater flow blockage. Following is a discussion on interactions between disperse particles moving in a continuous fluid medium that gives further insight into the effect of increasing the pressure ratio.



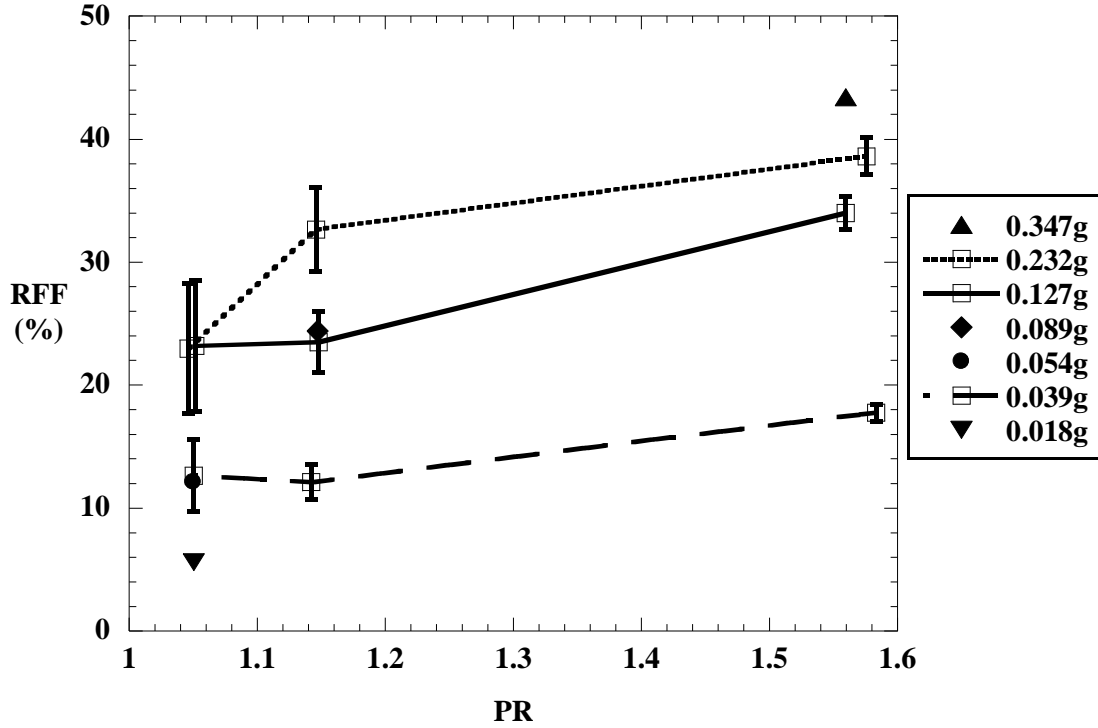


**Figure 4.11. Blockage versus pressure ratio for various injected rust masses.**

To understand why blockage increased with pressure ratio, it is useful to consider the non-dimensional Stokes number (Stk). The Stokes number is defined in Equation 4.1 as the particle time scale ( $\tau_p$ ) divided by the fluid time scale ( $\tau_f$ ).

$$\text{Stk} = \frac{\tau_p}{\tau_f} \quad (4.1)$$

As described in [36], the Stokes number is a measure of a particle's responsiveness to changes in direction of the fluid motion. In this sense, a small Stokes number ( $\text{Stk} < 1$ ) implies a relatively small particle time scale, which means particles will tend to follow flow streamlines around bends. On the other hand, a large Stokes number ( $\text{Stk} > 1$ ) implies a relatively large particle time scale. Particles with large Stokes numbers will tend to be insensitive to major changes in the flow direction, and their behavior is ballistic.

The particle time scale and fluid time scale are defined by Equations 4.2 and 4.3, respectively. It may be observed from Equation 4.2 that, for a given particle size, the particle time scale remains constant. Since the present set of experiments utilized a single particle size distribution, the particle time scale was constant in an average sense.

$$\tau_p = \frac{\rho_p \cdot d_p^2}{18 \cdot \mu_f} \quad (4.2)$$

$$\tau_f = \frac{L_c}{v_f} \quad (4.3)$$

The present set of experiments also was performed on a single coupon, so the characteristic length scale ( $L_c$ ) in Equation 4.3 was constant for a given cross section of the blade platform area. As the pressure ratio and air mass flow rate were increased, the average air velocity increased, resulting in a smaller fluid time scale. Since the particle time scale was constant, increasing the pressure ratio had the effect of increasing the Stokes number, causing particles to exhibit ballistic behavior and deviate from following bends in the flow. As the pressure ratio was increased, particles were more prone to inertial impaction with the blade platform and seal pin surfaces, which lead to increased likelihood of deposition and flow blockage. In addition, moving from the root towards the seal pin, the flow area narrowed causing a decrease in characteristic length scale and an increase in the fluid velocity in the streamwise direction. Thus, even for a given pressure ratio, the Stokes number increased in the streamwise direction, with the highest Stokes number occurring at the seal pin flow area.

To theoretically predict the particle behavior, particle Stokes numbers could be defined for the spectrum of particle sizes and fluid velocities tested in the current experiment. As the narrowest region in the flow area, one of the clearances between the seal pin and the blade platforms could be taken as the characteristic length scale ( $L_c$ ), but the clearance is unknown and is difficult to calculate from the experimental results due to the impossibility of separately distilling the discharge coefficient ( $C_D$ ) and the seal pin flow area ( $A_{sp}$ ) from the results. It was therefore not possible to accurately determine numerical values of Stokes numbers for this set of experiments.

Moving through the blade platform area in the direction of coolant flow, the flow area narrowed from a maximum near the root to the minimum area at the seal pin; therefore, even for particle injection at a constant pressure ratio, particle behavior was anticipated to become progressively more ballistic as particles moved towards the seal pin flow area and the fluid velocity increased. The existence of ballistic particle behavior was confirmed through visual observation of particle deposition and analysis of deposition samples using an environmental scanning electronic microscope (ESEM). Figure 4.12 and Figure 4.13 show rust particle

deposition on the rear blade and front blade (as labeled in Figure 3.13), respectively, as they were disassembled after performing a particle injection test. By visual inspection, it was observed that the largest particles were only present at the larger flow area between the seal pin and the root. Furthermore, the smallest particles, appearing as a finely ground powder, were only present at the narrowest flow area where the seal pin contacted the front blade platform.

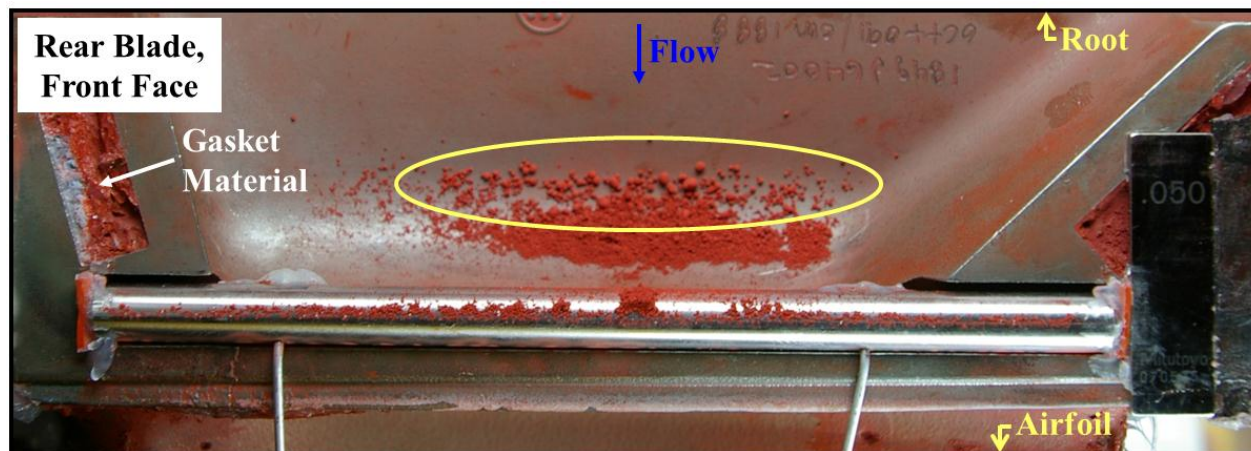


**Figure 4.12. Larger particles deposited upstream of the seal pin in the large flow area between the seal pin and the root.**

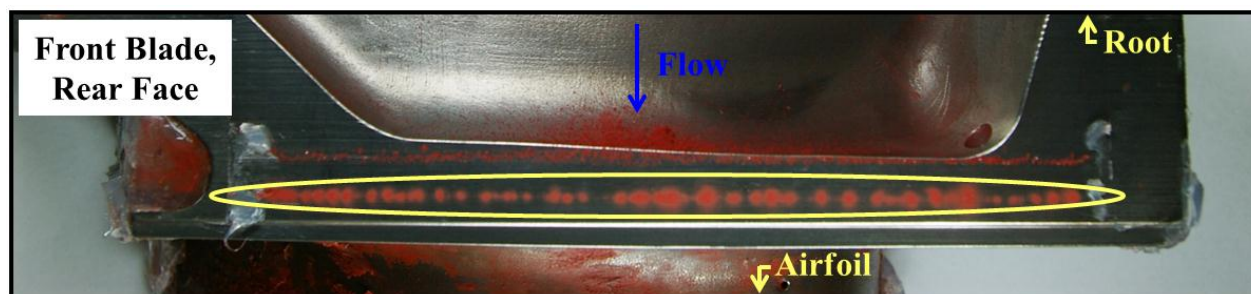


**Figure 4.13. Very small particles deposited at the narrowest flow area where the seal pin contacted the front blade.**

Particle size analysis was performed on ESEM particle images to further investigate the visually observed variation in particle size with deposition location. To obtain statistical particle size information such as the particle size distribution, analysis using a method such as laser diffraction is preferred over ESEM; however, the small quantities of deposited particles in many locations were insufficient for analysis with laser diffraction, so the ESEM technique was selected because it allows for analysis of very small sample sizes. As shown in Figure 4.14,

deposition samples were taken from various locations on the front blade, rear blade, and seal pin for ESEM analysis.

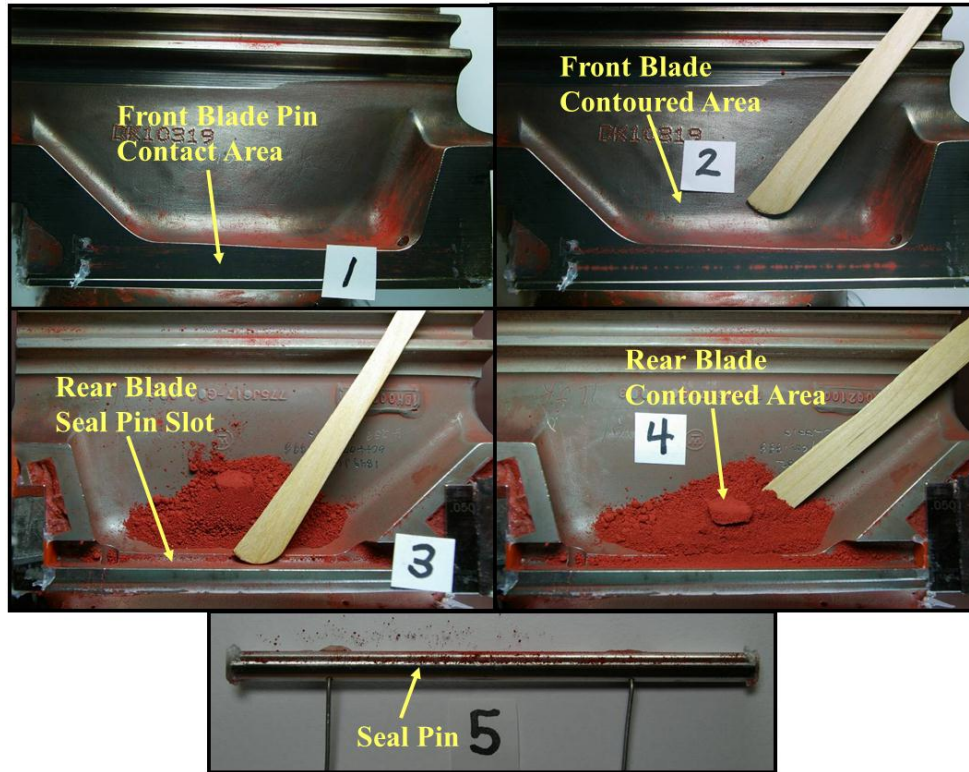


**Figure 4.14. Deposition sample locations for ESEM particle size analysis.**

Several observations can be made from visual comparisons of the magnified particle images shown in Figure 4.15. Moving from left to right, top to bottom, the images in Figure 4.15 are ordered approximately with the flow path from the larger flow area near the root to the narrowest flow area at the seal pin. It is evident that particle sizes and shapes in sample 4 most closely resemble the pre-injection mixture 5 particles, and samples 2 and 3 have intermediately-sized particles. Particles in samples 5 and 1 are not only smaller, but have relatively smooth, rounded edges compared with the sharp, jagged edges of particles in the upstream and pre-injection samples. This shape difference indicates significant particle erosion occurred as particles moved through the blade platform area and thus supports the hypothesis that particles were ballistic and tended to impact surfaces at bends in the flow path.

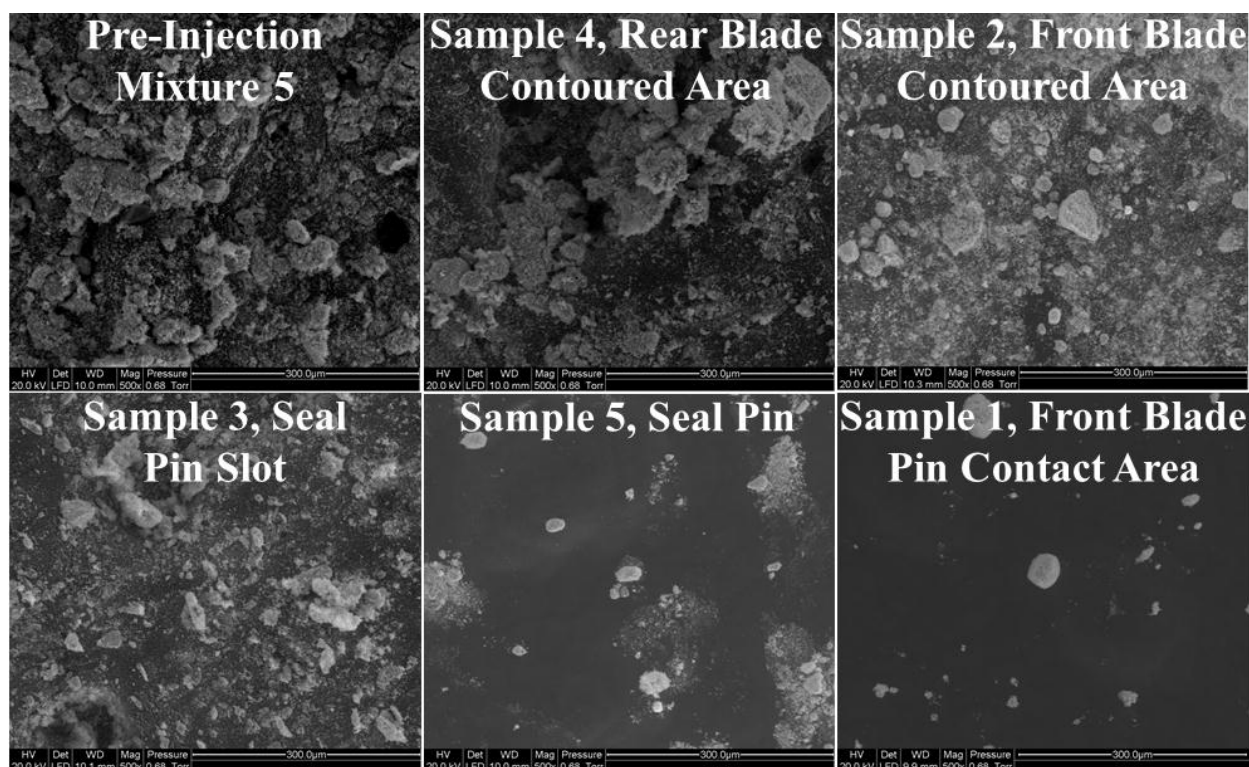


**Figure 4.15. ESEM images of rust particles at 500x magnification; sample numbers correspond with labels in Figure 4.14.**

A semi-quantitative analysis of particle size was performed using the ESEM images shown in Figure 4.15. Each image was divided into an evenly spaced 3 by 3 grid for a total of 9 cells. From each cell, the most clearly defined particle was encircled, and the particle size was determined from the diameter of the circle using the image scale. An example of the particle sizing method is shown in Figure 4.16.



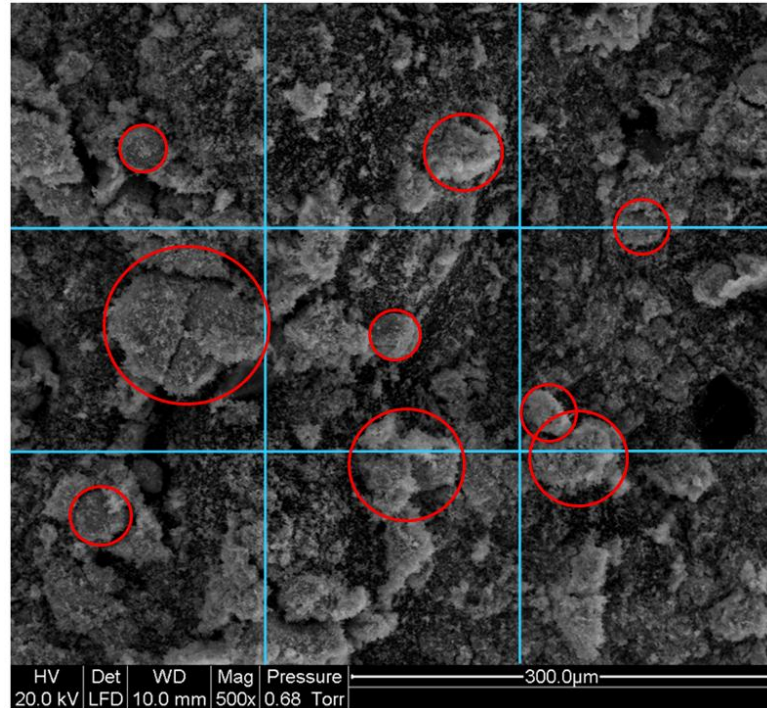


**Figure 4.16. An ESEM image divided into 9 cells with particles encircled for size analysis.**

As shown in Figure 4.17, the resulting particle sizes were plotted in histograms for each deposition sample. The largest particles ( $> 100 \mu\text{m}$ ) were present only in the pre-injection particles and in sample 4 from the rear blade contour. Downstream samples from the seal pin slot, seal pin, and seal pin contact area (samples 3, 5, and 1, respectively) had no particles larger than  $100 \mu\text{m}$ . Absence of large particles in the downstream samples from the narrowest flow areas suggests that large particles impacted with upstream surfaces and either were deposited or rebounded. Particle erosion and breakage occurred for the rebounding particles so that, progressing from the root towards the seal pin, sizes of suspended particles became increasingly smaller.

Recalling Figure 4.14, samples 4 and 2 were from similar locations on the rear and front blades, respectively. One might expect, then, that particle sizes for these samples would have been relatively similar. As shown in Figure 4.17, sample 2 from the front blade did not contain particle sizes larger than  $100 \mu\text{m}$ , which were present in sample 4 from the rear blade. The absence of larger particles in the front blade sample was a result of the method used to disassemble the test chamber. As shown in Figure 4.18, during disassembly the test chamber

was turned 90 degrees from its orientation during rust injection testing such that the rear face of the front blade platform faced downwards. Turning the chamber resulted in the largest particles falling from the rear face of the front blade onto the front face of the rear blade, which skewed the particle size distribution for sample 2 towards smaller size particles.

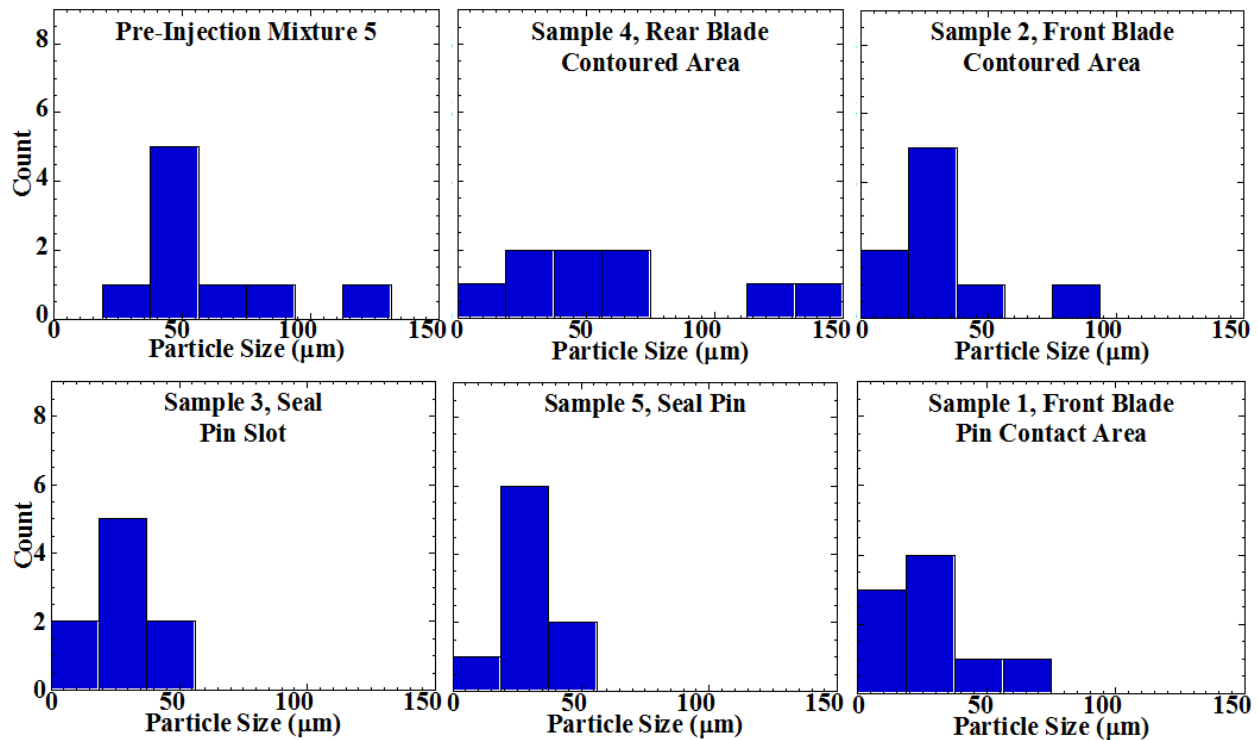


**Figure 4.17. Histograms of particle sizes from deposition samples; sample numbers correspond with locations given in Figure 4.14.**

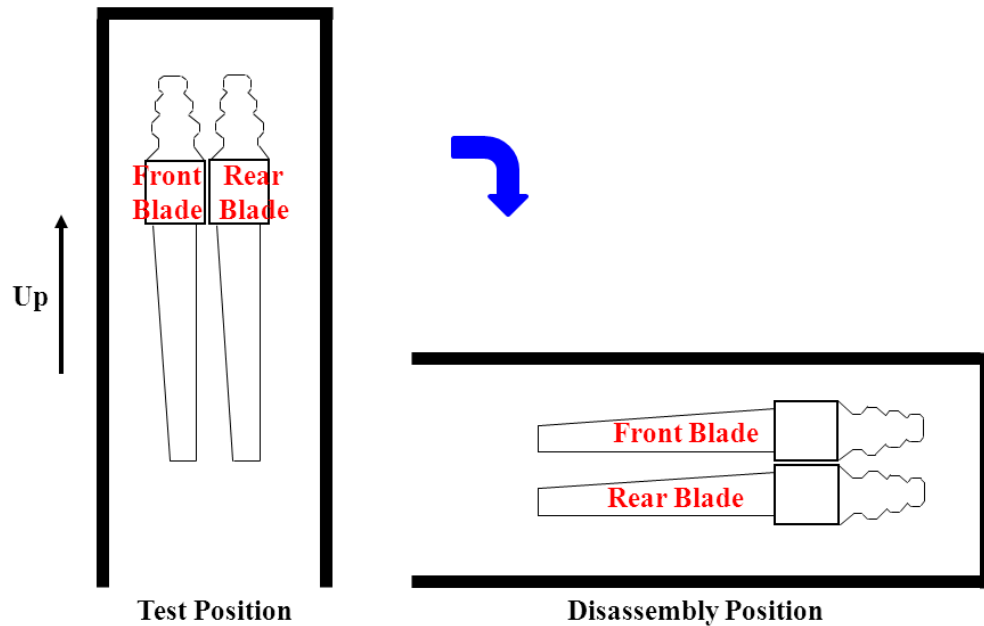


**Figure 4.18. Test chamber positions for rust injection testing and disassembly.**

The observed increase in blockage with pressure ratio is opposite to the trends found in previous studies [15-17]. For pressure ratios greater than about 1.1, these studies found that blockage decreased with increasing pressure ratio. The explanation for their results was that the increased flow velocities at higher pressure ratios caused particle erosion and breakage and helped to force particles through the cooling hole geometries. Though particle erosion and breakage occurred in the present study and increased with pressure ratio, the size of the flow area was much smaller, so many of the broken and eroded particles were still too large to pass through the seal pin flow area and thus were deposited, causing blockage. The variation in blockage trends with pressure ratio suggests that the shape and size of the flow geometry play a significant role in determining the blockage characteristics. A particle blockage trend for a particular flow geometry may be applicable to other flow geometries provided the geometries are similar in size and shape and the particulate matter is of similar size.

Rust amounts for particle injection tests were selected based on the sand mass loading ratio found to yield blockages representative of field-run conditions in jet engine hardware. It is possible that actual quantities of rust flowing through land-based engine hardware are greater than those specified in the test matrix. To investigate effects of injecting larger amounts of rust, an additional blockage test was performed in which quantities of rust particles were cumulatively



injected into engine hardware until a maximum blockage was achieved. This test was performed at a pressure ratio of 1.15, and the results are shown in Figure 4.19. Ultimately a maximum blockage of 74% was achieved for a total injected rust mass of 5.3 g (MLR = 30 s).

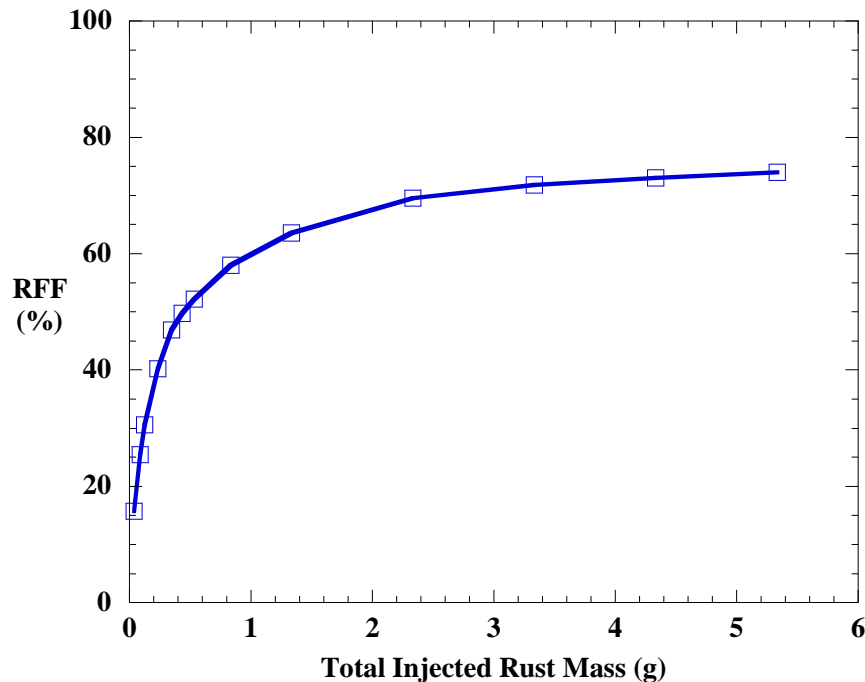


**Figure 4.19. Maximum blockage test for cumulative total rust injection of 5.3 g at a pressure ratio of 1.15.**

Similar to the blockage curves shown in Figure 4.8 and Figure 4.9, the blockage curve from this experiment clearly exhibits the trend of diminishing blockage with each additional rust injection. To understand why blockage diminished with each successive rust injection, consider the effects of blockage on the air and particle flow. As blockage of the flow area increases, the mass flow rate of air is reduced, decreasing the fluid velocity everywhere in the blade platform area. Lower fluid velocities correspond to an increase in the fluid time scale and thus a decrease in the Stokes number, so particles are better able to follow the flow and less likely to deposit on surfaces and cause additional blockage. In summary, as blockage of the flow area increases, suspended particles are less likely to impact surfaces and cause further blockage, which results in diminishing blockage with each successive rust amount injected. It has also been noted that a significant percentage (about 80%) of injected particles remained trapped at or upstream of the seal pin gap area. The presence of particles lying upstream of the seal pin effectively altered the geometric shape of the blade platform area and the surface conditions to which subsequently

injected particles were exposed, which also played a role in diminishing the blockage with successive rust mass injections. Finally, a 100% blockage was not achievable simply from rust injection, which is understandable since conglomerations of rust particles are porous.

## Chapter 5. RESULTS FROM ROTATING TESTS

Results from rust injection tests performed in the rotating test facility are presented in this chapter. Tests were performed on a rotating coupon, called coupon 1, made to represent a section of the full-scale engine hardware tested in the static test facility. A second rotating coupon was also tested. Called coupon 2, this coupon was also representative of the full-scale hardware but incorporated a different shape on the surface leading into the seal pin slot. Recall Figure 3.18 for a schematic of the rotating test coupons. The effects of pressure ratio and rotation were investigated, with some tests performed at a low rotating speed ( $\Omega = 0.002$ ) and others performed at conditions matching the engine centrifugal acceleration ( $\Omega = 1$ ).

### 5.1 Rust Deposition

Significant quantities of rust particles deposited in the test coupons. In contrast with the static test facility, a measurable amount of rust also deposited in the particle feed pipe and on surfaces upstream of the test coupons. See Figure 5.1 for locations of the rust deposition inside the chamber. After each rust injection test, rust particles were removed from the test facility by tapping, brushing, and blowing with compressed air. The mass and location of collected particles was recorded. Generally more than 95% of the total injected rust mass was collected from the particle feed pipe, diffuser plate, chamber walls and coupon flanges, and from inside the test coupons. Deposition inside the test coupons included all rust deposited on the contoured surfaces leading into the seal pin slot and rust surrounding the seal pin. Very little rust passed through the test coupons to the atmospheric downstream chamber.

For coupon 1, the distribution of rust is given for multiple tests at  $PR_{rot} = 1.6$  in Figure 5.2 and Figure 5.3, for  $\Omega = 0.002$  and  $\Omega = 1$ , respectively. For tests at  $\Omega = 0.002$ , rust particles depositing in the test coupons divided nearly evenly among the three coupons. This result was expected since the flow through each coupon was similar and the particle diffuser plate was relatively symmetric. A similar fraction of the total injected rust entered the test coupons at  $\Omega = 1$ , however, the rust deposited predominantly in one or two of the coupons. This trend indicated that, at high rotating speeds, particles were more sensitive to slight asymmetry in the diffuser plate or variation in installation of the diffuser plate.

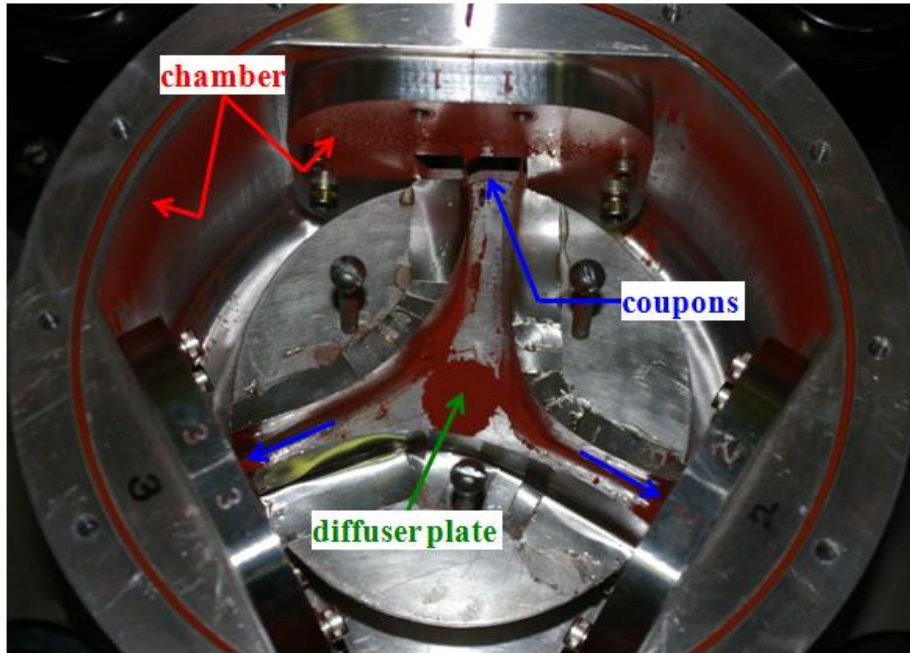


Figure 5.1. Rust deposition locations inside the rotating chamber.

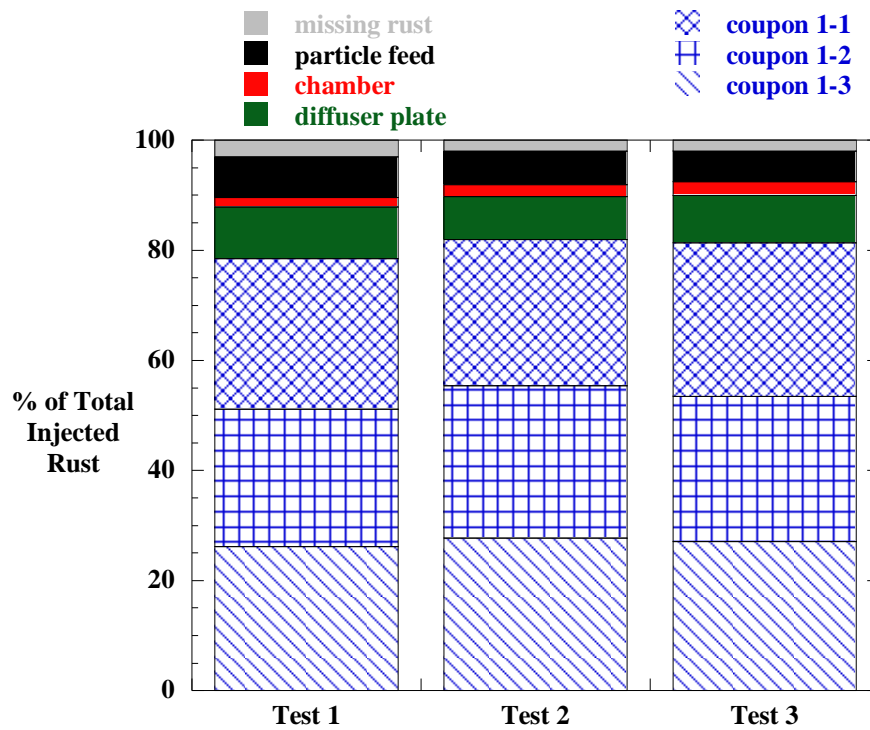


Figure 5.2. Rust deposition by location for coupon 1,  $PR_{rot} = 1.6$ ,  $\Omega = 0.002$ .



**Coupon 1-3  
(0.86 g)**

**Rust**

**Seal Pin**

**Rotation** →

**Coupon 1-1  
(4.8 g)**

**Rust**

**Seal Pin**

81

Comparison of Figure 5.5 with Figure 5.6 illustrates similarity in the pattern of the rust deposition for both coupons at  $\Omega = 0.002$  and  $\Omega = 1$ , however certain aspects of the deposition were affected by the increased centrifugal acceleration at  $\Omega = 1$ . In both coupons, surfaces leading the seal pin were relatively clean at  $\Omega = 0.002$  but were coated with a thin layer of very fine rust particles at  $\Omega = 1$ . Inside the spinning chamber, the motion of the air was similar to that of a solid body rotating at the speed of the chamber. Particles entering this air were subjected to forces due to centrifugal and coriolis accelerations. The rotation accelerated larger, more massive particles radially outward so rapidly that the coriolis acceleration had little effect in increasing their circumferential velocity. Smaller particles, on the other hand, were less-rapidly accelerated in the outward radial direction such that there was more time for the coriolis acceleration to increase their circumferential velocity towards that of the fluid. In addition, smaller particles tended to follow the flow more readily since the time scale for their momentum change was much shorter. For these reasons, only the smaller particles deposited on the leading surfaces while the larger particles formed the bulk of the deposition on the trailing surfaces.

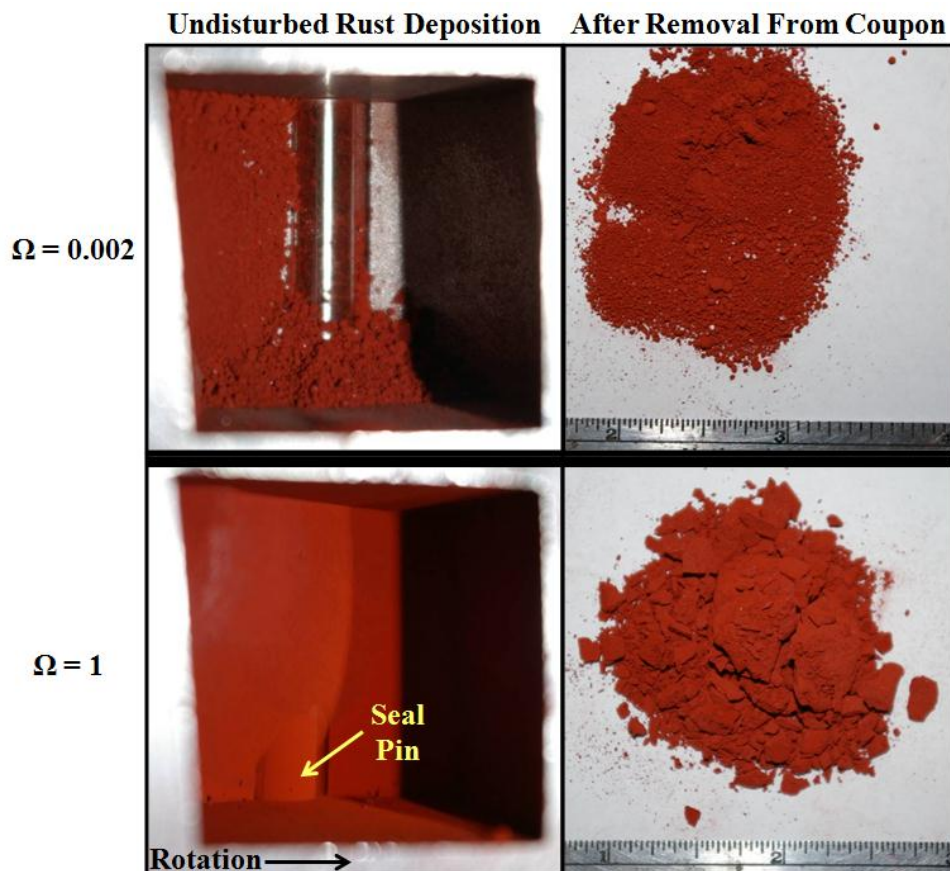
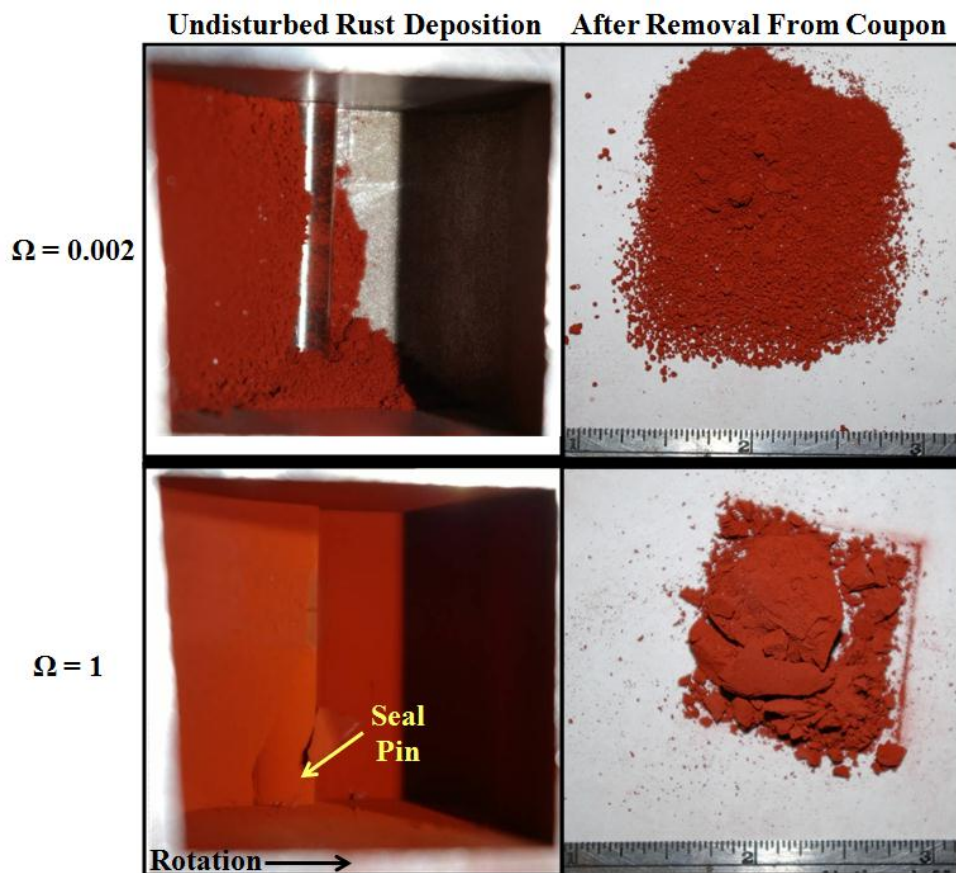


Figure 5.5. Rust deposition in coupon 1 after tests performed at  $PR_{rot} = 1.6$  (scale in inches).

Due to the increased centrifugal acceleration at  $\Omega = 1$ , the particles compacted to form hardened conglomerations as large as 12 mm, which is illustrated in on the right-hand side of Figure 5.5 and Figure 5.6. After tests at  $\Omega = 0.002$ , deposited particles were relatively loose and could be easily removed from the parts by gentle tapping and brushing. At  $\Omega = 1$ , vigorous tapping and brushing was required to remove particles from the parts, and large conglomerations of particles remained even after being removed. Recalling Figure 4.5, this effect was similar to what was observed in initial experiments where particles were spun in a sample tube at  $\Omega = 1$ .



**Figure 5.6. Rust deposition in coupon 2 after tests performed at  $PR_{rot} = 1.6$  (scaled in inches).**

Though it was difficult to remove the seal pin without disturbing deposition on the rough slot surface, at  $\Omega = 1$  particles were sufficiently compacted so that some of the rust remained on the slot surface after removing the seal pin. Deposition on the rough slot surface of coupon 1 appeared similar to what was observed on a blade removed from field service, as shown in



Figure 5.7. The similarity of deposition on coupon 1 and the field service hardware was anticipated since coupon 1 was similar in shape to the engine hardware.

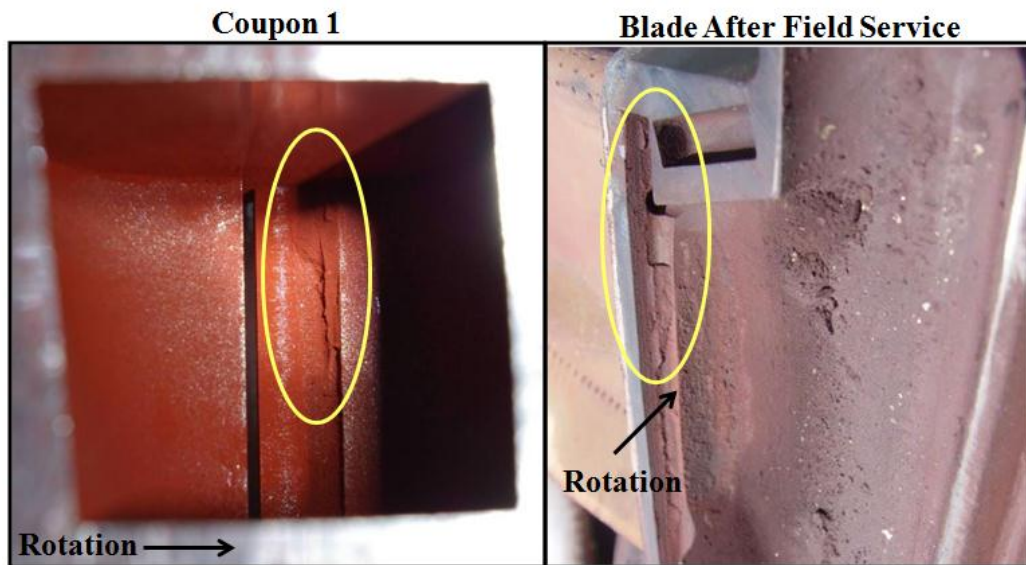


**Figure 5.7. Rust deposition in coupon 1 after rust injection test at  $\Omega = 1$  compared with a blade removed from field service (seal pins removed) [1].**

## **5.2 Flow Blockage**

To investigate the effect of pressure ratio under rotating conditions, rust was injected at pressure ratios of 1.15, 1.6, and 1.8 for coupon 1 at  $\Omega = 0.002$ . Results for these tests are provided in Figure 5.8, where the deposited rust mass is based on the proportion of total injected rust found in the test coupons at the end of the test and thus excludes rust deposited elsewhere in the test facility. Flow blockage was independent of pressure ratio. This finding is in contrast with the results from the static testing, for which blockage increased with pressure ratio due to increasingly ballistic particle behavior. Ballistic particle behavior was also observed in the rotating tests, however the centrifugal forces governed this behavior, dominating any effect from the increased fluid velocity at higher pressure ratios.



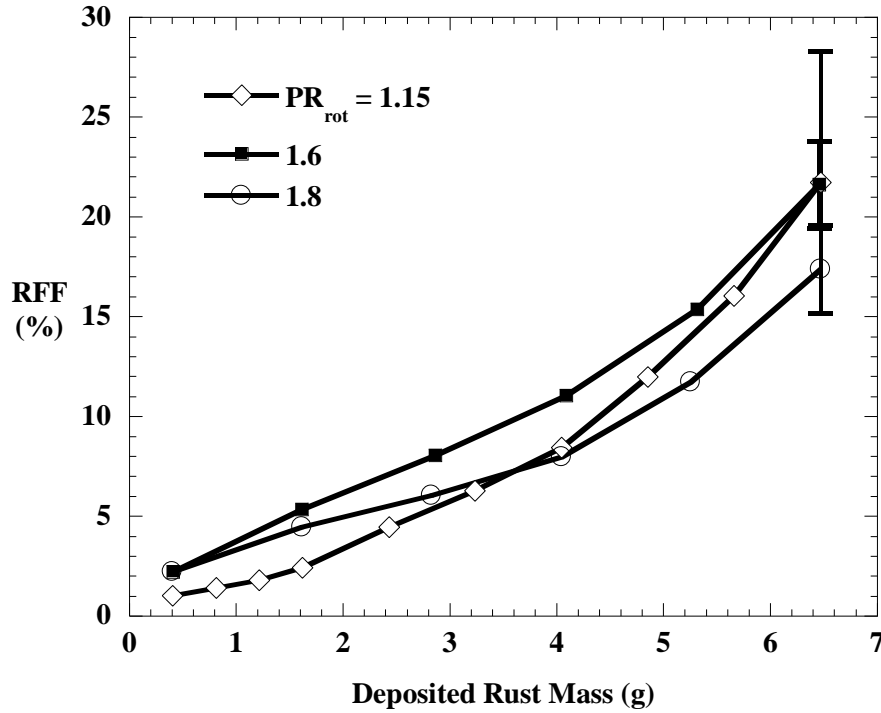


**Figure 5.8. Flow blockage as a function of deposited rust mass, coupon 1,  $\Omega = 0.002$ .**

As shown in Figure 5.9, flow blockage was similar for coupons 1 and 2 at  $\Omega = 0.002$  and for coupon 1 at  $\Omega = 1$ . There was a considerable increase in blockage for coupon 2 at  $\Omega = 1$ . Recall from Figure 3.27 that, although coupons 1 and 2 were created to have identical flow areas, coupon 2 exhibited an increased baseline flow function curve over all pressure ratios. This increase in flow function was a result of the smooth transition into the seal pin slot, which acted to reduce flow losses and more effectively pump fluid through the gap between the pin and the rough slot surface. Similarly, when rust particles were injected, this smooth transition directed particles into the contact area between the seal pin and the rough slot surface. At  $\Omega = 1$ , the coriolis acceleration delivered smaller particles to the leading side of the pin, resulting in significantly increased blockage for coupon 2. In coupon 1, the lip at the leading edge of the seal pin slot acted to shield the contact area between the pin and the slot from small particles delivered to the leading side of the seal pin at  $\Omega = 1$ . For this reason, coupon 1 exhibited less flow blockage at  $\Omega = 1$  relative to coupon 2.

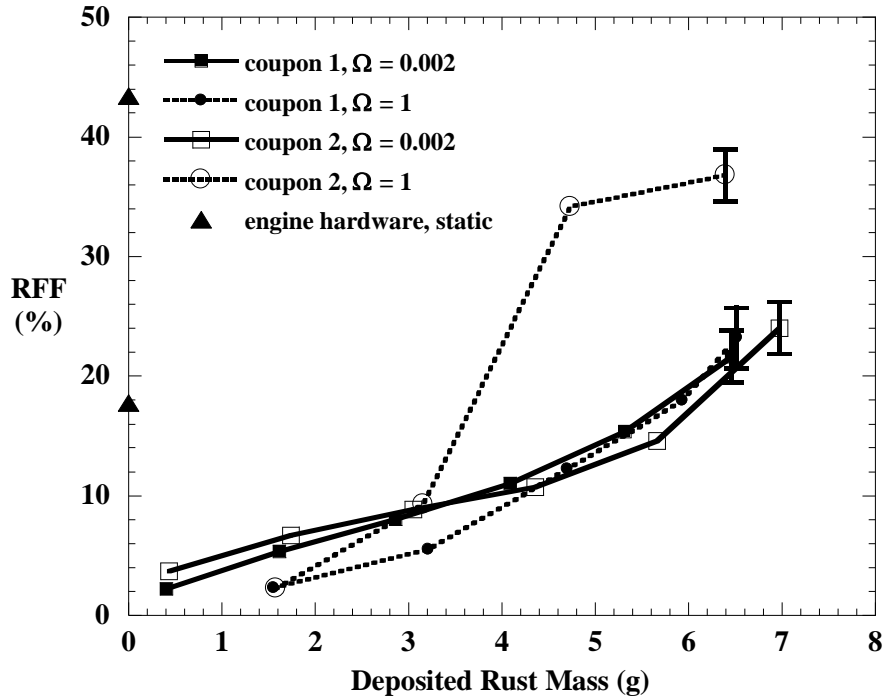


**Figure 5.9. Flow blockage as a function of deposited rust mass, coupons 1 and 2,  $\Omega = 0.002$  and  $\Omega = 1$ ,  $PR_{rot} = 1.6$ .**

The range of flow blockage for the static tests is shown on the mantissa of Figure 5.9 for reference. As discussed in Section 3.12, the injected rust mass was dramatically increased in the rotating tests in order to obtain flow blockage comparable to the static tests. More rust was required in the rotating tests since deposition began primarily on the trailing contoured surface. In contrast, the absence of rotation in the static tests resulted in particles depositing more closely to the seal pin contact areas. One test was performed in the rotating study to determine how much of the rust deposited in the test coupons was contributing to the flow blockage. Flow blockage was measured after rust was injected in coupon 1 at  $\Omega = 0.002$ . The three test coupons were then removed from the chamber, and particles not immediately near the seal pin were removed from the parts, taking care not to disturb the seal pin and particles deposited nearby. One test coupon is shown in Figure 5.10 before and after removal of particles not immediately near the seal pin. The test coupons were then reinstalled in the chamber, and flow blockage was again measured at  $\Omega = 0.002$ . The flow blockage remained constant after the removal of 96% of the rust particles deposited inside the part. This finding indicated that only particles depositing at the seal pin contact area caused flow blockage. For consistency, however, flow blockage results were reported in terms of the entire rust mass deposited in the parts.

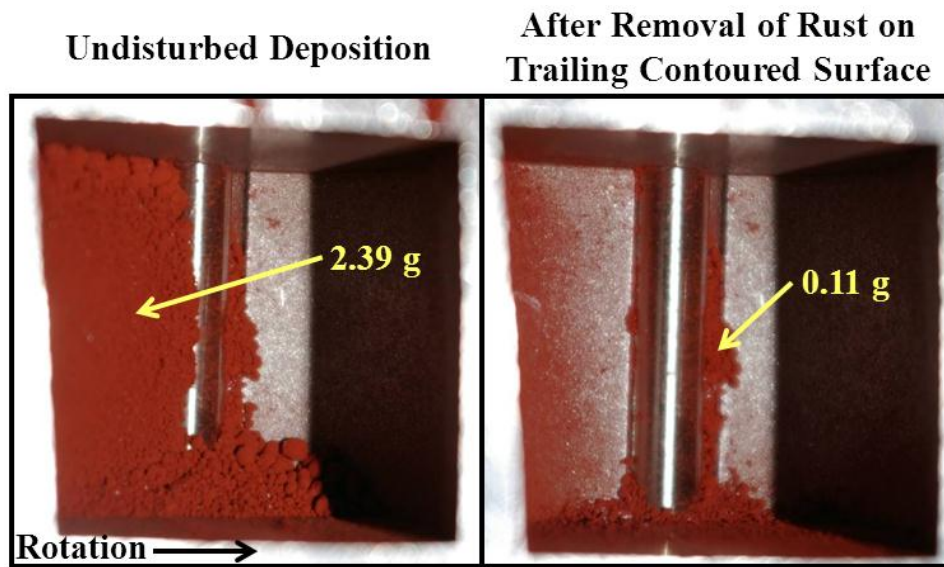


Figure 5.10. Coupon 1 before and after removal of rust deposited on trailing contoured surface.

## Chapter 6. CONCLUSIONS

Rust deposition at the axial seal pin was investigated through particle injection experiments performed on static blades from a gas turbine and on rotating coupons similar to a section of the blades. Early on in this study, rust particles composed primarily of red iron oxide were characterized in separate experiments at temperatures and centrifugal accelerations representative of gas turbine conditions. Rust particles were unaffected in their physical appearance and size distribution when heated up to 850°C, the first row blade root temperature. After spinning at 12,100 times gravitation acceleration, conditions representative of the turbine, rust particles exhibited significant compaction to twice their loose bulk density. These findings indicated that, for particles entrained in air flow near the axial seal pin, centrifugal acceleration plays a significant role in deposition while the effect of temperature is minimal.

In the static test facility, a predicted flow function based on one-dimensional isentropic flow relations was found to under-predict the flow function over pressure ratios ranging from 1.05 to 1.8. The mismatch between the predicted and measured flow functions was partially a result of using an assumed flow area for the predicted flow function but also reflected the limitations of one-dimensional analysis in modeling flow losses. In the experimental data, the choking behavior seen in the one-dimensional analysis was not observed as the pressure ratio neared the critical value of 1.89. This trend indicated that viscous losses and multi-dimensional flow effects were significant and varied with pressure ratio due to the non-ideal entrance and the small size of the flow area. The constant discharge coefficient included in the one-dimensional analysis was not sufficient to account for the losses in the seal pin flow area. From these results, it can be concluded that one-dimensional analysis does not accurately model the physics of flow through very small and uniquely shaped flow geometries such as the area around the axial seal pin.

Rust injection experiments performed in the static facility yielded flow blockages up to 74%, showing that particle deposition plays a significant role in reducing coolant flow at the axial seal pin. The pressure ratio strongly influenced deposition under non-rotating conditions. Increasing the pressure ratio from 1.05 to 1.6 increased the flow blockage by 15% to 20% for the larger rust masses tested. Particle breakage and erosion were observed in rust deposits, which indicated many particles tended to impact surfaces due to their inability to follow flow

streamlines. Visual observation and ESEM particle size analysis revealed that only the smallest particles were deposited in the narrowest flow areas at the seal pin, which underscores the challenge of preventing particle deposition in the seal pin slot since the smallest particles are the most difficult to filter from the cooling air.

For rotating tests performed even at very low centrifugal acceleration relative to engine conditions, the effect of pressure ratio was negligible. At  $\Omega = 0.002$ , flow blockage was similar for pressure ratios of 1.15, 1.6, and 1.8. Rotation caused particles to initially build up on the trailing contoured surface of the test coupons and then gradually move towards the seal pin as the deposit grew. Because of this effect, the mass loading ratio was increased from about 0.5 s in the static tests to as much as 28 s in the rotating tests to yield comparable flow blockage. Both coupons 1 and 2 exhibited similar flow blockages up to about 25% for rust injected at  $\Omega = 0.002$ .

Tests performed on the rotating test coupons at  $\Omega = 1$  were most representative of turbine conditions and provided an improved understanding of particle behavior at the seal pin. At  $\Omega = 1$ , particles were compacted into large conglomerations with the potential to inhibit motion of the seal pin. Additionally, the increased coriolis acceleration delivered smaller particles to the region leading the seal pin. For this reason, the smooth transition incorporated into coupon 2 resulted in increased flow blockage at  $\Omega = 1$  as smaller particles and air were more easily directed into the flow area between the seal pin and the rough slot surface. The smooth transition in coupon 2 was designed to eliminate the possibility of particles hanging up between the leading edge of the seal pin and the blade platform, however the increase in flow blockage indicated that more particles deposited on the leading side of the seal pin. Clearly this effect was opposite of the design goal to reduce particle deposition near the seal pin.

Based on the results from rotating tests, an alternative blade platform design is proposed in Figure 6.1, in which cross-sectional views of the seal pin and blade platforms are shown. The original design is the same as the engine hardware tested in the static facility and coupon 1 tested in the rotating facility. The proposed modification is the extension of the blade platform surface around the leading side of the seal pin, creating a more circuitous flow path to decrease the likelihood of particles being delivered to the leading side of the seal pin. Since rotating tests have indicated the dominance of ballistic particle motion in the outward radial direction, it is anticipated that, with the proposed modification, particles would be unable to follow the flow path to the leading side of the seal pin. The effect of this modification on particle deposition and

flow blockage should be experimentally analyzed prior to implementation. Computational analysis could also be performed in conjunction with experiments to improve understanding of the flow and particle behavior.

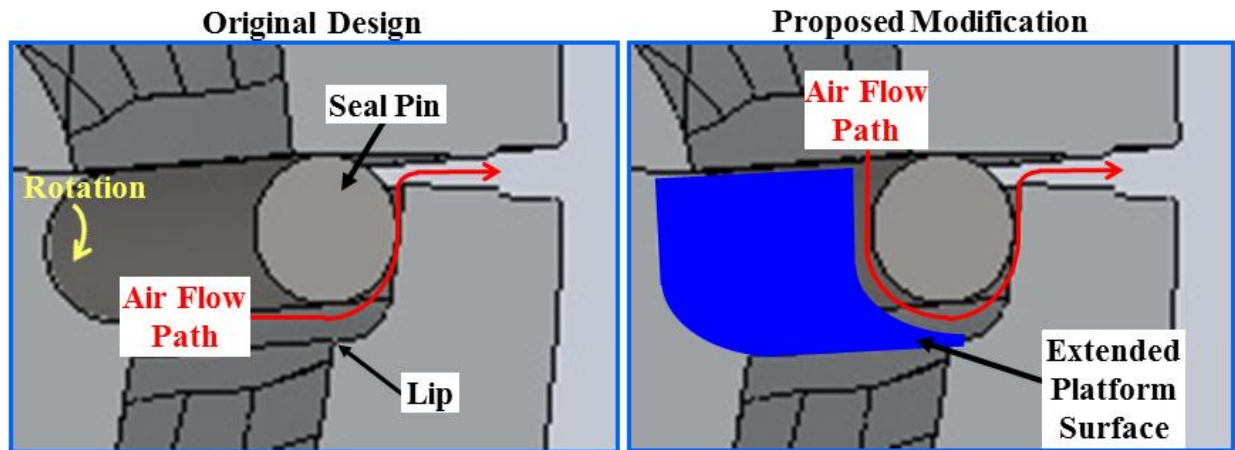


**Figure 6.1. Original blade platform design and proposed modification.**

## REFERENCES

- [1] Mount, Jonathan, “STG6-5000F Turbine Row 1 Blade Liberation,” Siemens TR-05161, Siemens Power Generation, 2005.
- [2] Blong, R.J. *Volcanic Hazards, A Sourcebook on the Effects of Explosions*. Sydney: Academic Press Australia, 1984.
- [3] Brantley, Steven R. *The Eruption of Redoubt Volcano, Alaska, December 14, 1989 – August 31, 1990*. Washington: U.S. Government Printing Office, 1990.
- [4] Katili, J.A., and Adjat Sudradjat. *Galunggung, The 1982 – 1983 Eruption*. Indonesia: Volcanological Survey of Indonesia, 1984.
- [5] Dovali, Francisco, “Rotor Air System Particulate Testing at AEC Vann Unit 2,” Siemens EC-06171, Siemens Power Generation, 2006.
- [6] Friedlander, Sheldon. K. *Smoke, Dust, and Haze: Fundamentals of Aerosol Dynamics*. New York: Oxford University Press, 2000.
- [7] Dunn, M.G., C. Padova, J.E. Moller, and R.M. Adams, “Performance Deterioration of a Turbofan and a Turbojet Engine Upon Exposure to a Dust Environment,” *Journal of Engineering for Gas Turbines and Power*, vol. 109, July, pp. 336-343, 1987.
- [8] Batcho, P.F., J.C. Moller, C. Padova, and M.G. Dunn, “Interpretation of Gas Turbine Response Due to Dust Ingestion,” *Journal of Engineering for Gas Turbines and Power*, vol. 109, July, pp. 344-352, 1987.
- [9] Dunn, M.G., C. Padova, and R.M. Adams, “Operation of Gas Turbine Engines in Dust-Laden Environments,” presented at AGARD-Advanced Technology of Aero Engine Components, Paris, May 4-8, 1987.
- [10] Kim, J., M.J. Dunn, A.J. Baran, D.P. Wade, and E.L. Tremba, “Deposition of Volcanic Materials in the Hot Sections of Gas Turbine Engines,” *Journal of Engineering for Gas Turbines and Power*, vol. 115, pp. 641-651, 1993.
- [11] Weaver, M.M., M.G. Dunn, and T. Heffernan, “Experimental Determination of the Influence of Foreign Particle Ingestion on the Behavior of Hot-Section Components Including Lamilloy,” 96-GT-337.

- [12] Wenglarz, R.A. and R.G. Fox, Jr., "Physical Aspects of Deposition from Coal-Water Fuels under Gas Turbine Conditions," *Journal of Engineering for Gas Turbines and Power*, vol. 112, pp. 9-14, 1990.
- [13] Jensen, Jared W., Sean W. Squire, Jeffrey P. Bons, and Thomas H. Fletcher, "Simulated Land-Based Turbine Deposits Generated in an Accelerated Deposition Facility," *Journal of Turbomachinery*, vol. 127, pp. 462-470, 2005.
- [14] Hamed, A. and W. Tabakoff, "Erosion and Deposition in Turbomachinery," *Journal of Propulsion and Power*, vol. 22, no. 2, Mar.-Apr., pp. 350-360, 2006.
- [15] Walsh, W.S., K.A. Thole, Chris Joe, "Effects of Sand Ingestion on the Blockage of Film-Cooling Holes," GT2006-90067.
- [16] Land, Camron C., Karen A. Thole, and Chris Joe, "Considerations of a Double-Wall Cooling Design to Reduce Sand Blockage," *Journal of Turbomachinery*, vol. 132, no. 3, pp. 031011-1 - 031011-8, 2010.
- [17] Cardwell, N.D., K.A. Thole, S.W. Burd, 2008, "Investigation of Sand Blocking within Impingement and Film Cooling Holes," GT2008-51351.
- [18] Schneider, O., H.J. Dohmen, and A.W. Reichert, "Experimental Analysis of Dust Separation in the Internal Cooling Air System of Gas Turbines," GT2002-30240.
- [19] Schneider, O., H.J. Dohmen, F.-K. Benra, and D. Brillert, "Investigations of Dust Separation in the Internal Cooling Air System of Gas Turbines," GT2003-38393.
- [20] Schneider, O., H.J. Dohmen, F.-K. Benra, and D. Brillert, "Dust Separation in a Gas Turbine Pre-Swirl Cooling Air System: A Parameter Variation," GT2004-53048.
- [21] Haider, A. and O. Levenspiel, "Drag Coefficient and Terminal Velocity on Non-Spherical Particles," *Powder Technology*, vol. 58, pp. 63-70, 1989.
- [22] Laurello, Vincent. (2009, June 26). *RE: Rust Characterization Meeting - Notes and Presentation File* [personal email].
- [23] Santisteban, Vanessa. (2009, September 15). *RE: Siemens Rust Characterization Project - Table of Parameters* [personal email].
- [24] Weaver, S.A., "Heat Transfer and Pressure Drop Augmentation in Micro Channels with Pin Fins," M.S. Thesis, The Pennsylvania State University, University Park, PA, 2010.
- [25] "Wyko Surface Profilers Technical Reference Manual," Veeco Metrology Group.



- [26] Tham, Kok-Mun. (2010, May 19). *RE: Rust Characterization Meeting Follow-up* [personal email].
- [27] Maeng, D.J., J.S. Lee, R. Jakoby, S. Kim, and S. Wittig, “Characteristics of Discharge Coefficient in a Rotating Disk System,” *Journal of Engineering for Gas Turbines and Power*, vol. 121, October, pp. 663-669, 1999.
- [28] Zucrow, Maurice J., and Joe D. Hoffman. *Gas Dynamics, Vol. 1*. New York, John Wiley, 1976.
- [29] *Compressed Gas Handbook*, NASA Office of Technology Utilization, Scientific and Technical Information Division, Washington, D.C., 1969.
- [30] Engineering Sciences Data Unit, “Pressure losses across orifice plates, perforated plates, and thick orifice plates in ducts,” Item no. 81039, London: Engineering Sciences Data Unit, 1981.
- [31] Voss, L.R., and R.N. Hollyer, Jr., “Nozzles for Air Flow Measurement,” *The Review of Scientific Instruments*, vol. 34, no. 1, pp. 70-74, 1963.
- [32] Tang, S.P. and J.B. Fenn, “Experimental Determination of the Discharge Coefficients for Critical Flow through and Axisymmetric Nozzle,” *AIAA Journal*, vol. 16, no. 1, pp. 41-46, 1978.
- [33] Kayser, John C. and Robert L. Shambaugh, “Discharge Coefficients for Compressible Flow through Small-Diameter Orifices and Convergent Nozzles,” *Chemical Engineering Science*, vol. 46, no. 7, pp. 1697-1711, 1991.
- [34] White, Frank M. *Fluid Mechanics*, 3rd ed. New York: McGraw Hill, 1994.
- [35] Beckwith, Thomas G., Roy D. Marangoni, and John H. Lienhard V. *Mechanical Measurements, Fifth Ed.* New York: Addison Wesley, 1993.
- [36] Crowe, Clayton T., and Efstathios E. Michaelides. *Multiphase Flow Handbook*. Taylor and Francis Group, 2006.

## Appendix A. CALCULATIONS FOR STATIC TESTS

### Nomenclature

#### General

$A_i$	LFE calibration constants, $i = 0,1,2$
DP	differential pressure
FF	flow function: $FF = \frac{\dot{m}\sqrt{T_0}}{P_0}$
$FF_0$	baseline static flow function from curve fit of flow data for clean engine hardware
LFE	laminar flow element
$m_i$	coefficient for baseline flow function curve fit, $i = 0,1,2,3\dots$
$\dot{m}$	mass flow rate
$P_0$	total pressure upstream of the nozzle or seal pin flow area
$p$	static pressure
PR	pressure ratio: $PR = \frac{P_0}{p_b}$
R	gas constant
RFF	reduction in flow function evaluated at blocked pressure ratio: $RFF = 1 - \frac{FF}{FF_0} \Big _{PR}$
$T_0$	total temperature upstream of the nozzle or seal pin flow area
T	temperature
$\dot{V}$	volumetric flow rate

#### Subscripts

atm	atmospheric
b	evaluated at the downstream chamber
sp	evaluated across the seal pin flow area in the test chamber
g	gage pressure
LFE	evaluated upstream of the LFE
std	standard parameter; $T_{std} = 21^\circ\text{C}$ , $p_{std} = 101 \text{ kPa}$
0	total parameter evaluated at the upstream chamber (except when used with FF)

#### Greek

$\mu$	dynamic viscosity
$\rho$	density

### Flow Function Calculation

The fundamental measured parameters for the experiment were  $T_{LFE}$ ,  $p_{LFE}$ ,  $p_{atm}$ ,  $DP_{LFE}$ ,  $T_0$ ,  $P_0$ , and  $DP_{sp}$ . Recall Figure 3.7 for a schematic of the static test facility. These measured parameters were used to calculate the flow function (FF) and pressure ratio (PR) for each test.

Air temperatures upstream of the LFE ( $T_{LFE}$ ) and at the chamber inlet ( $T_0$ ) were measured using E-type thermocouples. The air dynamic viscosity ( $\mu$ ) was calculated in micropoise using Equation A.1, which requires  $T_{LFE}$  in °F.

$$\mu = \frac{14.58 \cdot \left( \frac{T_{LFE} + 459.67}{1.8} \right)^{\frac{3}{2}}}{110.4 + \frac{T_{LFE} + 459.67}{1.8}} \quad (A.1)$$

The upstream gage pressure at the LFE ( $p_{LFE,g}$ ) was measured using an Omegadyne PX309-100G5V gage pressure transducer rated for 0-690 kPa gage (0-100 PSIG). Atmospheric pressure ( $p_{atm}$ ) measured with a Setra model 370 barometer was added to the LFE upstream gage pressure to obtain the absolute upstream LFE pressure ( $p_{LFE}$ ). The air density upstream of the LFE ( $\rho_{LFE}$ ) was calculated from the ideal gas relation as shown in Equation A.2.

$$\rho_{LFE} = \frac{p_{LFE}}{R \cdot T_{LFE}} \quad (A.2)$$

The air volumetric flow rate was measured using a Meriam Instrument LFE rated for a maximum air flow rate of 750 cm<sup>3</sup>/s (1.6 SCFM) at standard conditions. Standard temperature and pressure were defined as 21°C (70°F) and 101 kPa (14.7 PSIA), respectively. Differential pressure across the LFE was measured using a variable-diaphragm Validyne model DP103 differential pressure transducer. The diaphragm was selected based on the volume flow rate and differential pressure range for a particular test.

As provided in the LFE manual [1], Equation A.3 was used to calculate the actual air volumetric flow rate at the LFE ( $\dot{V}_{LFE}$ ) with units of actual ft<sup>3</sup>/min, where density ( $\rho_{LFE}$ ) has units of lb/ft<sup>3</sup>, differential pressure ( $DP_{LFE}$ ) has units of in. H<sub>2</sub>O at 4°C, and viscosities ( $\mu_{LFE}$  and  $\mu_{std}$ ) have units of micropoise. The LFE calibration coefficients ( $A_0$ ,  $A_1$ , and  $A_2$ ) are given in Table A.1.

$$\dot{V}_{LFE} = \left[ A_0 + A_1 \cdot \left( \frac{\rho_{LFE} \cdot DP_{LFE}}{\mu_{LFE}^2} \right) + A_2 \cdot \left( \frac{\rho_{LFE} \cdot DP_{LFE}}{\mu_{LFE}^2} \right)^2 \right] \cdot \left( \frac{DP_{LFE}}{\mu_{LFE}} \right) \cdot \left( \frac{\mu_{std}}{\mu_{LFE}} \right) \quad (A.3)$$

**Table A.1. Laminar Flow  
Element Calibration Coefficients**

$A_0$	3.70704E01
$A_1$	-9.58300E04
$A_2$	1.01032E08

The air mass flow rate ( $\dot{m}$ ) was then calculated from the density ( $\rho_{LFE}$ ) and actual volume flow rate ( $\dot{V}_{LFE}$ ) using Equation A.4.

$$\dot{m} = \rho_{LFE} \cdot \dot{V}_{LFE} \quad (A.4)$$

The upstream chamber total pressure ( $P_0$ ) was measured using an Omegadyne model PX319-100A5V absolute pressure transducer rated for 0-690 kPa (0-100 PSIA). The upstream chamber was sufficiently large to be considered as a plenum, so the measured static pressure was equal to the total pressure. Ultimately the mass flow rate ( $\dot{m}$ ), upstream chamber total temperature ( $T_0$ ), and upstream chamber total pressure ( $P_0$ ) were used to calculate the dimensional flow function (FF) given by Equation A.5. The flow function was reported with units of  $m \cdot s \cdot K^{1/2}$ .

$$FF = \frac{\dot{m} \sqrt{T_0}}{P_0} \quad (A.5)$$

The seal pin differential pressure ( $DP_{sp}$ ) was measured using a variable-diaphragm Validyne model DP15 differential pressure transducer. The diaphragm was selected based on the pressure ratio for a particular test. The upstream total to downstream static pressure ratio (PR) was calculated using Equation A.6.

$$PR = \frac{P_0}{P_0 - DP_{sp}} = \frac{P_0}{P_b} \quad (A.6)$$

### Blockage Calculation

The reduction in flow function (RFF) was calculated using Equation A.7, where both the clean baseline ( $FF_0$ ) and blocked flow functions were evaluated at the blocked pressure ratio.

$$RFF = 1 - \frac{FF}{FF_0} \bigg|_{PR} \quad (A.7)$$

Recalling Figure 3.25, injecting rust particles resulted in a decrease in flow function (FF) accompanied by a slight change in pressure ratio (PR). Due to the dependency of flow function on pressure ratio, a polynomial curve fit of flow function versus pressure ratio for clean baseline conditions was used to evaluate the clean flow function ( $FF_0$ ) at the blocked pressure ratio. This baseline flow function was calculated using Equation A.8, for which the coefficients for are provided in Table A.2.

$$FF_0 = m_0 + m_1 \cdot PR + m_2 \cdot PR^2 + m_3 \cdot PR^3 + m_4 \cdot PR^4 + m_5 \cdot PR^5 + m_6 \cdot PR^6 \quad (A.8)$$

**Table A.2. Coefficients for  
Static Baseline Flow Function**

m <sub>0</sub>	1.196024E-06
m <sub>1</sub>	-8.112001E-06
m <sub>2</sub>	1.812999E-05
m <sub>3</sub>	-1.935233E-05
m <sub>4</sub>	1.093568E-05
m <sub>5</sub>	-3.166676E-06
m <sub>6</sub>	3.710954E-07

## References

- [1] Meriam Process Technologies, “Laminar Flow Elements Installation and Operation Instructions,” File No. 501:440-11.

## Appendix B. CALCULATIONS FOR ROTATING TESTS

### Nomenclature

#### General

DP	differential pressure
$m_i$	coefficient for baseline flow function curve fit, $i = 0, 1, 2, 3 \dots$
$P_0$	total pressure upstream of the nozzle or seal pin flow area
$p$	static pressure
$PR_{rot}$	rotational pressure ratio
$r$	rotating chamber outer radius
$R$	gas constant
$T_{rot}$	rotational temperature
$T$	temperature
$v$	velocity

#### Subscripts

b	evaluated just downstream of the test coupons
w	measured at the inside diameter of the ballistic wall
sp	evaluated across the seal pin flow area in the rotating chamber
0	total parameter upstream of the rotating chamber

#### Greek

$\omega$	rotational speed
$\rho$	density

### Overview

For the rotating tests, the measurement equipment and fundamental measured parameters were the same as for the static tests except for the addition of the rotational speed measurement. Recall Figure 3.9 for a schematic of the rotating test facility. As discussed in Section 3.7, however, rotational forms of the flow function and pressure ratio were used to account for additional energy imparted to the flow due to centrifugal acceleration. A mathematical correction was applied to the measured differential pressure across the rotating chamber to account for the pressure difference between the downstream pressure taps in the ballistic wall and the exit of the test coupons. The calculation of the chamber differential pressure is provided in the following section.

The reduction in flow function was calculated as in Equation A.7 using the rotational forms of the flow function and pressure ratio. Similar to the static tests, polynomial curve fit equations were used to calculate the baseline flow function for evaluating flow blockage at a

constant pressure ratio. The baseline flow function for  $\Omega = 0.002$  was calculated using Equation B.1, for which coefficients are provided in Table B.1. Equation B.2 was used to calculate the baseline flow function for  $\Omega = 1$ , with coefficients for coupons 1 and 2 provided in Tables B.2 and B.3, respectively.

$$FF_{0,rot} = m_0 + m_1 \cdot PR_{rot} + m_2 \cdot PR_{rot}^2 + m_3 \cdot PR_{rot}^3 + m_4 \cdot PR_{rot}^4 + m_5 \cdot PR_{rot}^5 + m_6 \cdot PR_{rot}^6 \quad (B.1)$$

**Table B.1. Baseline Flow Function Coefficients for Coupons 1 and 2,  $\Omega = 0.002$**

$m_0$	-5.168309E-06
$m_1$	2.058363E-05
$m_2$	-3.422925E-05
$m_3$	3.040276E-05
$m_4$	-1.517089E-05
$m_5$	4.026809E-06
$m_6$	-4.438244E-07

$$FF_{0,rot} = m_0 + m_1 \cdot PR_{rot} + m_2 \cdot PR_{rot}^2 + m_3 \cdot PR_{rot}^3 + m_4 \cdot PR_{rot}^4 \quad (B.2)$$

**Table B.2. Baseline Flow Function Coefficients for Coupon 1,  $\Omega = 1$**

$m_0$	-3.879101E-07
$m_1$	8.166895E-07
$m_2$	-6.173690E-07
$m_3$	2.141787E-07
$m_4$	-2.830932E-08

**Table B.3. Baseline Flow Function Coefficients for Coupon 2,  $\Omega = 1$**

$m_0$	-5.926693E-07
$m_1$	1.232554E-06
$m_2$	-9.050933E-07
$m_3$	3.028602E-07
$m_4$	-3.846552E-08

### Chamber Differential Pressure Correction

The downstream pressure tap used to measure differential pressure across the test coupons was installed flush with the inside diameter of the ballistic wall, about 8 cm radially

outward from the outer diameter of the chamber and the exit of test coupons. It was therefore necessary to correct for the pressure difference between the measured pressure at the ballistic wall ( $p_w$ ) and the desired back pressure at the exit to the test coupons ( $p_b$ ). Flow outside the rotating chamber was assumed to behave as a free vortex for which the Bernoulli equation can be applied everywhere. The Bernoulli equation written for locations just downstream of the test coupons and at the ballistic is given in Equation B.3. The no-slip condition was assumed, resulting in the circumferential velocity matching that of the ballistic wall and the chamber outer diameter at each respective location. Incompressible flow with constant density was also assumed.

$$\frac{p_b}{\rho_b} + \frac{v_b^2}{2} = \frac{p_w}{\rho_b} \quad (\text{B.3})$$

Rewriting the circumferential velocity at the test coupon exit in terms of the container outside radius ( $r$ ) and rotating speed ( $\omega$ ) and solving for the pressure at the test coupon exit yields Equation B.4.

$$p_b = p_w - \frac{1}{2} \rho_b (r \cdot \omega)^2 \quad (\text{B.4})$$

The downstream density was approximated from the ideal gas relation as in Equation B.5.

$$\rho_b = \frac{p_w}{R \cdot T_w} \quad (\text{B.5})$$

Recall that chamber differential pressure transducer was connected on the high side to the pressure tap just upstream of the rotary coupling and on the low side to the pressure tap at the ballistic wall. In this configuration, the differential pressure between the chamber upstream and the ballistic wall ( $DP_w$ ) was measured as given in Equation B.6.

$$DP_w = P_0 - p_w \quad (\text{B.6})$$

The desired differential pressure was the differential pressure across the test coupon seal pins ( $DP_{sp}$ ), which was calculated using Equation B.7. Nominal values for the correction term in Equation B.7 are provided in Table B.4.

$$DP_{sp} = DP_w + \frac{1}{2} \rho_b (r \cdot \omega)^2 \quad (\text{B.7})$$



**Table B.4. Pressure Correction Nominal Values**

		Pressure Correction, $1/2 \cdot \rho(r \cdot \omega)^2$	
$\Omega$	$PR_{rot}$	Nominal Value (kPa)	% of $DP_w$
0.002	1.15	0.018	0.12
	1.6	0.016	0.03
	1.8	0.016	0.02
1	1.3	7.3	58
	1.6	7.3	19
	2.1	7.3	8.7

The rotational pressure ratio across the test coupons was then calculated from Equation B.8, where  $P_0$  and  $T_0$  are, respectively, the measured upstream total pressure and temperature. Recall Equation 3.19 for the definition of the rotational temperature ( $T_{rot}$ ).

$$PR_{rot} = \left( \frac{P_0}{P_0 - DP_{sp}} \right) \left( 1 + \frac{T_{rot}}{T_0} \right)^{\frac{\gamma}{\gamma-1}} \quad (B.8)$$

## Appendix C. UNCERTAINTY ANALYSIS FOR STATIC TESTS

### Nomenclature

#### General

DP	differential pressure
FF	flow function: $FF = \frac{\dot{m}\sqrt{T_0}}{P_0}$
FF <sub>0</sub>	baseline static flow function from curve fit of flow data for clean engine hardware
LFE	laminar flow element
$\dot{m}$	mass flow rate
m <sub>rust</sub>	rust mass
MLR	rust mass loading ratio: $MLR = \frac{m_{rust}}{\dot{m}}$
P <sub>0</sub>	total pressure upstream of the nozzle or seal pin flow area
p	static pressure
PR	pressure ratio: $PR = \frac{P_0}{p_b}$
RFF	reduction in flow function evaluated at blocked pressure ratio: $RFF = 1 - \frac{FF}{FF_0} \Big _{PR}$
T <sub>0</sub>	total temperature upstream of the nozzle or seal pin flow area
T	temperature
U <sub>bi</sub>	bias uncertainty
U <sub>p</sub>	precision uncertainty
U	total parameter uncertainty, various subscripts

#### Subscripts

atm	atmospheric
b	evaluated at the downstream chamber
g	gage pressure
LFE	evaluated upstream of the LFE
sp	evaluated across the seal pin flow area in the test chamber

### Flow Function Uncertainty

An uncertainty analysis was performed for the flow function (FF), which was calculated from experimental data as shown in Equation C.1. The functional dependence of flow function on measured parameters is given in Equation C.2 for a given flow area. Details of the mass flow rate ( $\dot{m}$ ) calculation can be found in Appendix A.

$$FF = \frac{\dot{m}\sqrt{T_0}}{P_0} \quad (C.1)$$

$$FF = f(p_{\text{atm}}, p_{\text{LFE,g}}, P_0, DP_{\text{LFE}}, T_{\text{LFE}}, T_0) \quad (\text{C.2})$$

Measurement error includes bias error, which causes the measured value to vary from the actual value by a fixed amount for all measurements, and precision error, which causes variation in the measured value for repeated measurements of the same actual value. When accounting for the uncertainty of a measured value, bias and precision errors are considered, respectively, as the bias uncertainty ( $U_{\text{bi}}$ ) and precision uncertainty ( $U_{\text{p}}$ ). The total uncertainty ( $U$ ) for a measured value was determined from Equation C.3. From this point forward, all uncertainties represent total uncertainties.

$$U = \sqrt{U_{\text{bi}}^2 + U_{\text{p}}^2} \quad (\text{C.3})$$

The partial derivative method as described in [1] was used to determine propagation of uncertainty from the measured parameters to the overall flow function uncertainty ( $U_{\text{FF}}$ ), which is given in Equation C.4. The overall flow function uncertainty was previously reported in Table 3.11.

$$U_{\text{FF}} = \left[ \left( \frac{\partial FF}{\partial p_{\text{atm}}} \cdot U_{\text{patm}} \right)^2 + \left( \frac{\partial FF}{\partial p_{\text{LFE,g}}} \cdot U_{\text{pLFE,g}} \right)^2 + \left( \frac{\partial FF}{\partial P_0} \cdot U_{\text{P0}} \right)^2 + \left( \frac{\partial FF}{\partial DP_{\text{LFE}}} \cdot U_{\text{DPLFE}} \right)^2 + \left( \frac{\partial FF}{\partial T_{\text{LFE}}} \cdot U_{\text{TLFE}} \right)^2 + \left( \frac{\partial FF}{\partial T_0} \cdot U_{\text{T0}} \right)^2 \right]^{\frac{1}{2}} \quad (\text{C.4})$$

Parameter uncertainties and the overall flow function uncertainty ( $U_{\text{FF}}$ ) were calculated at three pressure ratios, namely  $PR = 1.05, 1.15$ , and  $1.6$ . The relative contribution of each measured parameter towards the overall flow function uncertainty is given in Figure C.1 for these three pressure ratios. The gage pressure upstream of the LFE ( $p_{\text{LFE,g}}$ ), the total upstream chamber pressure ( $P_0$ ), and the LFE upstream temperature ( $T_{\text{LFE}}$ ) measurements were the largest contributors to the overall flow function uncertainty. The uncertainties of all the measured parameters were driven by the instrument bias uncertainties. For each measured parameter used to calculate the flow function, the same instrument was used for all tests, resulting in a constant bias uncertainty. Increasing the pressure ratio (and thus  $p_{\text{LFE,g}}$ ,  $P_0$ , and  $DP_{\text{LFE}}$ ) diminished the proportion of bias uncertainty to the measured value and thus reduced the relative contributions of  $p_{\text{LFE}}$ ,  $P_0$ , and  $DP_{\text{LFE}}$  to the overall flow function uncertainty. The LFE upstream temperature ( $T_{\text{LFE}}$ ) and chamber upstream temperature ( $T_0$ ) were approximately constant for all experiments,

and therefore their relative contributions to overall flow function uncertainty increased with pressure ratio because of the diminishing contributions of  $p_{LFE}$ ,  $P_0$ , and  $DP_{LFE}$ . Compared with  $T_0$ ,  $T_{LFE}$  contributed significantly more to the total flow function uncertainty due to its use in a squared term when calculating the actual air volume flow rate.

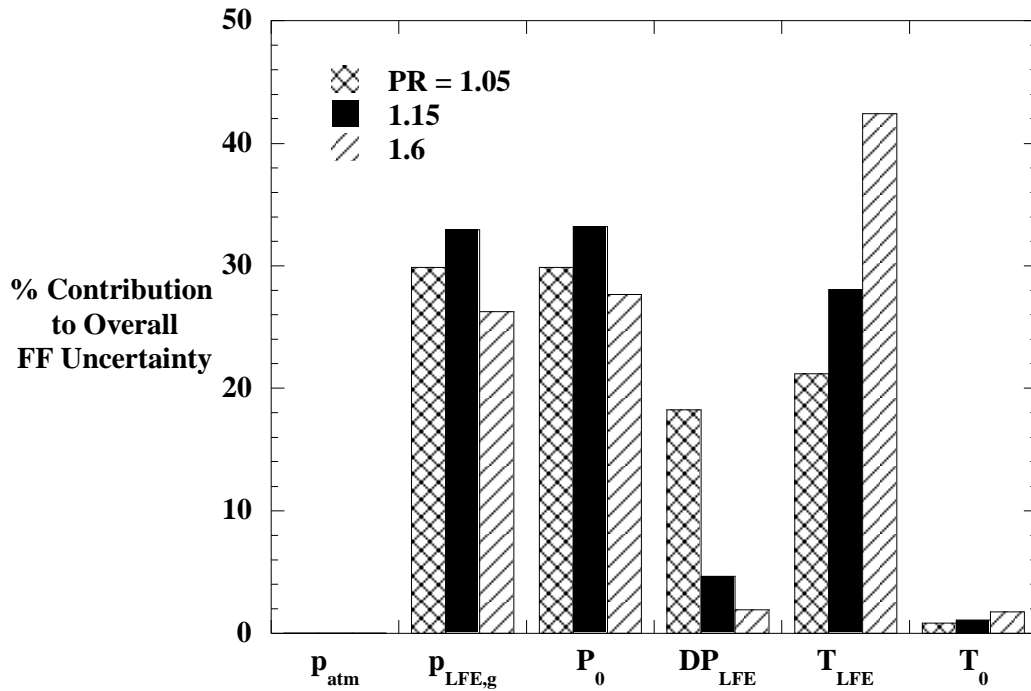


**Figure C.1. Relative contributions of measured parameters to the overall flow function uncertainty.**

Tables C.1, C.2, and C.3 summarize parameter uncertainties and their relative contributions to the overall flow function uncertainty ( $U_{FF}$ ) for particular tests at each of the three pressure ratios studied.

**Table C.1. Flow Function Parameter Uncertainties for PR = 1.05**

Parameter	Value		Uncertainty	Units	% Contribution to $U_{FF}$
$p_{atm}$	97.6	$\pm$	0.022	kPa	0.005
$p_{LFE,g}$	4.27	$\pm$	1.72	kPa	30
$P_0$	102	$\pm$	1.72	kPa	30
$DP_{LFE}$	0.165	$\pm$	0.002	kPa	18
$T_{LFE}$	29.4	$\pm$	1.70	$^{\circ}\text{C}$	21
$T_0$	29.1	$\pm$	1.70	$^{\circ}\text{C}$	0.83
FF	1.21E-08	$\pm$	3.74E-10	m-s-K <sup>1/2</sup>	

**Table C.2. Flow Function Parameter Uncertainties for PR = 1.15**

Parameter	Value		Uncertainty	Units	% Contribution to $U_{FF}$
$p_{atm}$	97.6	$\pm$	0.022	kPa	0.005
$p_{LFE,g}$	14.48	$\pm$	1.72	kPa	33
$P_0$	113	$\pm$	1.72	kPa	33
$DP_{LFE}$	0.376	$\pm$	0.002	kPa	4.7
$T_{LFE}$	30.2	$\pm$	1.70	$^{\circ}C$	28
$T_0$	30.3	$\pm$	1.70	$^{\circ}C$	1.1
FF	2.74E-08	$\pm$	7.28E-10	m-s-K <sup>1/2</sup>	

**Table C.3. Flow Function Parameter Uncertainties for PR = 1.6**

Parameter	Value		Uncertainty	Units	% Contribution to $U_{FF}$
$p_{atm}$	97.6	$\pm$	0.022	kPa	0.004
$p_{LFE,g}$	58.4	$\pm$	1.72	kPa	26
$P_0$	156	$\pm$	1.72	kPa	28
$DP_{LFE}$	0.734	$\pm$	0.002	kPa	1.9
$T_{LFE}$	33.1	$\pm$	1.70	$^{\circ}C$	42
$T_0$	32.4	$\pm$	1.70	$^{\circ}C$	1.7
FF	5.19E-08	$\pm$	1.09E-09	m-s-K <sup>1/2</sup>	

### Reduction in Flow Function Uncertainty

An uncertainty analysis was also performed on the pressure ratio (PR) and reduction in flow function (RFF), defined in Equations C.5 and C.6, respectively. The functional dependence of RFF on the flow function at blocked conditions and measured parameters chamber upstream pressure ( $P_0$ ) and seal pin differential pressure ( $DP_{sp}$ ) is given in Equation C.7.

$$PR = \frac{P_0}{P_0 - DP_{sp}} \quad (C.5)$$

$$RFF = 1 - \frac{FF}{FF_0} \bigg|_{PR} \quad (C.6)$$

$$RFF = f(FF, P_0, DP_{sp}) \quad (C.7)$$

Uncertainty for the pressure ratio ( $U_{PR}$ ) and reduction in flow function ( $U_{RFF}$ ) were calculated using the partial derivative method as given in Equations C.8 and C.9, respectively.

Uncertainty values for pressure ratio and reduction in flow function were previously reported in Table 3.11.

$$U_{PR} = \sqrt{\left(\frac{\partial PR}{\partial P_0} \cdot U_{P_0}\right)^2 + \left(\frac{\partial PR}{\partial DP_{sp}} \cdot U_{DP_{sp}}\right)^2} \quad (C.8)$$

$$U_{RFF} = \sqrt{\left(\frac{\partial RFF}{\partial FF} \cdot U_{FF}\right)^2 + \left(\frac{\partial RFF}{\partial P_0} \cdot U_{P_0}\right)^2 + \left(\frac{\partial RFF}{\partial DP_{sp}} \cdot U_{DP_{sp}}\right)^2} \quad (C.9)$$

The relative contributions of the flow function (FF), upstream chamber pressure ( $P_0$ ), and chamber differential chamber pressure ( $DP_{sp}$ ), all evaluated at blocked conditions, to the overall RFF uncertainty are given in Figure C.2 for the cases of  $PR = 1.05$ , 1.15, and 1.6. For all three cases, the main contributor to the RFF uncertainty was the uncertainty in the flow function measured at blocked conditions. Contributions to uncertainty of FF measured at blocked conditions are similar to those given for FF in Figure C.1.

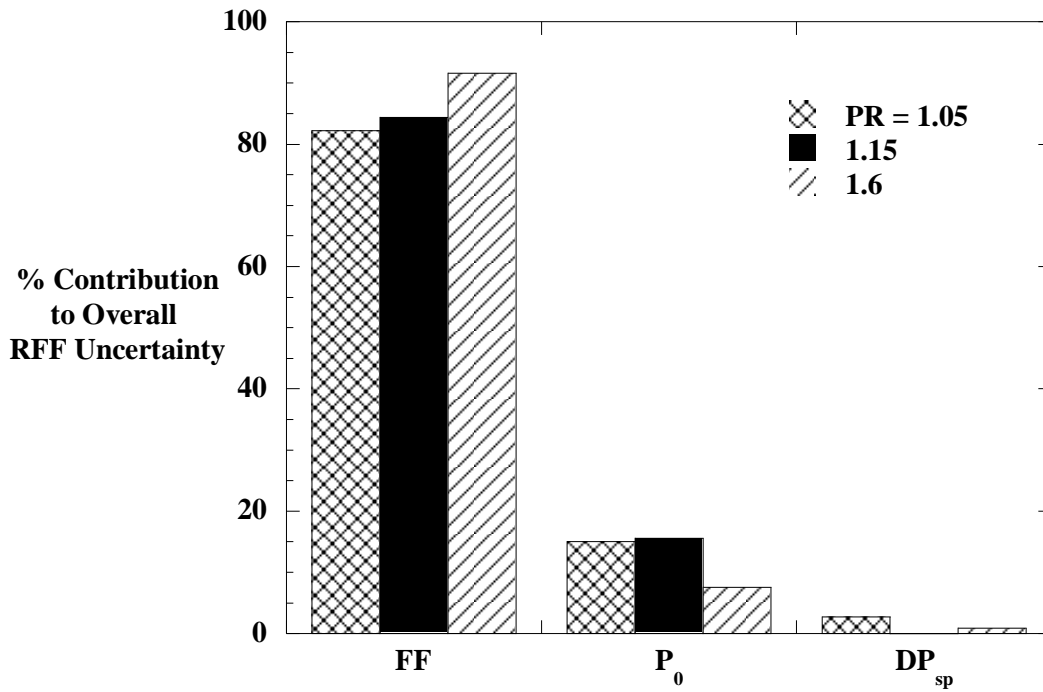


**Figure C.2. Relative contributions of parameters to the overall reduction in flow function uncertainty.**

Tables C.4, C.5, and C.6 summarize the parameter nominal values used in the RFF uncertainty calculation along with their uncertainties for blockage tests performed at  $PR = 1.05$ ,

1.15, and 1.6, respectively. Holding the mass loading ratio (MLR) constant, the uncertainty in RFF decreased with increasing pressure ratio due to the decrease in FF uncertainty as a percentage of the nominal FF value. Furthermore, as the pressure ratio was increased, the increase in nominal RFF value decreased the RFF uncertainty as a percentage of the nominal RFF value.

**Table C.4. Reduction in Flow Function Parameter Uncertainties for PR = 1.05**

<b>m<sub>rust</sub> = 0.039 g, MLR = 0.50 s</b>					
<b>Parameter</b>	<b>Value</b>		<b>Uncertainty</b>	<b>Units</b>	<b>% Contribution to U<sub>RFF</sub></b>
FF	1.03E-08	±	3.30E-10	m-s-K <sup>1/2</sup>	82
P <sub>0</sub>	102	±	1.72	kPa	15
DP <sub>sp</sub>	4.76	±	0.034	kPa	2.7
RFF	13.3	±	3.1	%	

**Table C.5. Reduction in Flow Function Parameter Uncertainties for PR = 1.15**

<b>m<sub>rust</sub> = 0.089 g, MLR = 0.50 s</b>					
<b>Parameter</b>	<b>Value</b>		<b>Uncertainty</b>	<b>Units</b>	<b>% Contribution to U<sub>RFF</sub></b>
FF	2.12E-08	±	5.72E-10	m-s-K <sup>1/2</sup>	84
P <sub>0</sub>	112	±	1.72	kPa	16
DP <sub>sp</sub>	14.5	±	0.002	kPa	0.001
RFF	21.9	±	2.3	%	

**Table C.6. Reduction in Flow Function Parameter Uncertainties for PR = 1.6**

<b>m<sub>rust</sub> = 0.232 g, MLR = 0.50 s</b>					
<b>Parameter</b>	<b>Value</b>		<b>Uncertainty</b>	<b>Units</b>	<b>% Contribution to U<sub>RFF</sub></b>
FF	3.27E-08	±	7.01E-10	m-s-K <sup>1/2</sup>	92
P <sub>0</sub>	156	±	1.72	kPa	7.5
DP <sub>sp</sub>	58.57	±	0.218	kPa	0.86
RFF	36.5	±	1.4	%	

## References

- [1] Beckwith, Thomas G., Roy D. Marangoni, and John H. Lienhard V. *Mechanical Measurements, Fifth Ed.* New York: Addison Wesley, 1993.

## Appendix D. UNCERTAINTY ANALYSIS FOR ROTATING TESTS

### Nomenclature

#### General

$a_c$	centrifugal acceleration
$a_{c,e}$	engine centrifugal acceleration at base load conditions
DP	differential pressure
$FF_{rot}$	rotational dimensional flow function: $FF_{rot} = \frac{\dot{m}\sqrt{T_{0,rot}}}{P_{0,rot}} \quad (m \cdot s \cdot K^{1/2})$
$FF_{0,rot}$	baseline rotational flow function from curve fit of flow data for clean test coupons
LFE	laminar flow element
$\dot{m}$	mass flow rate
$P_0$	total pressure upstream of the nozzle or seal pin flow area
$P_{0,rot}$	rotational total pressure upstream of the nozzle or seal pin flow area
$p$	static pressure
$PR_{rot}$	upstream total rotational to downstream static pressure ratio: $PR_{rot} = \frac{P_{0,rot}}{p_b}$
RFF	reduction in flow function evaluated at blocked pressure ratio: $RFF = 1 - \frac{FF_{rot}}{FF_{0,rot}} \bigg _{PR_{rot}}$
$T_0$	total temperature upstream of the nozzle or seal pin flow area
$T_{rot}$	rotational temperature
$T_{0,rot}$	rotational total temperature upstream of the nozzle or seal pin flow area
$T$	temperature
$U$	total parameter uncertainty, various subscripts

#### Subscripts

atm	atmospheric
g	gage pressure
LFE	evaluated upstream of the LFE
sp	evaluated across the seal pin flow area in the test chamber

#### Greek

$\gamma$	ratio of specific heats
$\omega$	rotating speed
$\Omega$	centrifugal acceleration relative to engine: $\Omega = \frac{a_c}{a_{c,e}}$



## Flow Function Uncertainty

An uncertainty analysis was performed for the rotational flow function ( $FF_{\text{rot}}$ ), which was calculated using Equation D.1. Equations for the upstream rotational total temperature ( $T_{0,\text{rot}}$ ) and pressure ( $P_{0,\text{rot}}$ ) were previously provided in Section 3.7. Details of the mass flow rate ( $\dot{m}$ ) calculation were provided in Appendix A. The functional dependence of  $FF_{\text{rot}}$  on measured parameters is given in Equation D.2.

$$FF_{\text{rot}} = \frac{\dot{m} \sqrt{T_{0,\text{rot}}}}{P_{0,\text{rot}}} \quad (\text{D.1})$$

$$FF_{\text{rot}} = f(p_{\text{atm}}, p_{\text{LFE,g}}, P_0, DP_{\text{LFE}}, T_{\text{LFE}}, T_0, \omega) \quad (\text{D.2})$$

The partial derivative method described in [1] was used to determine the propagation of uncertainty from the measured parameters to the calculated values. The overall uncertainty for the rotational flow function ( $U_{FF\text{rot}}$ ) was calculated using Equation D.3. Values for the  $U_{FF\text{rot}}$  were previously provided in Table 3.12 and Table 3.13, respectively, for  $\Omega = 0.002$  and  $\Omega = 1$ .

$$U_{FF\text{rot}} = \left[ \left( \frac{\partial FF_{\text{rot}}}{\partial p_{\text{atm}}} \cdot U_{p_{\text{atm}}} \right)^2 + \left( \frac{\partial FF_{\text{rot}}}{\partial p_{\text{LFE,g}}} \cdot U_{p_{\text{LFE,g}}} \right)^2 + \left( \frac{\partial FF_{\text{rot}}}{\partial P_0} \cdot U_{P_0} \right)^2 + \left( \frac{\partial FF_{\text{rot}}}{\partial DP_{\text{LFE}}} \cdot U_{DP_{\text{LFE}}} \right)^2 + \left( \frac{\partial FF_{\text{rot}}}{\partial T_{\text{LFE}}} \cdot U_{T_{\text{LFE}}} \right)^2 + \left( \frac{\partial FF_{\text{rot}}}{\partial T_0} \cdot U_{T_0} \right)^2 + \left( \frac{\partial FF_{\text{rot}}}{\partial \omega} \cdot U_{\omega} \right)^2 \right]^{\frac{1}{2}} \quad (\text{D.3})$$

Parameter uncertainties and the overall rotational flow function uncertainty ( $U_{FF\text{rot}}$ ) were calculated for  $\Omega = 0.002$  at  $PR_{\text{rot}} = 1.15, 1.6, \text{ and } 1.8$  and for  $\Omega = 1$  for both coupons. The contributions of each parameter uncertainty to  $U_{FF\text{rot}}$  are given in Figure D.1 and Figure D.2 for  $\Omega = 0.002$  and  $\Omega = 1$ , respectively. Uncertainty in the temperature measured just upstream of the LFE ( $T_{\text{LFE}}$ ) was the main contributor to  $U_{FF\text{rot}}$ . Similar to the trend observed in the static tests, the increased pressure ratios and mass flow rates tested in the rotating facility diminished the relative contributions of the uncertainty in the LFE gage pressure ( $p_{\text{LFE,g}}$ ) and the upstream total pressure ( $P_0$ ) while the relative contribution of  $T_{\text{LFE}}$  increased since the temperature was approximately constant.

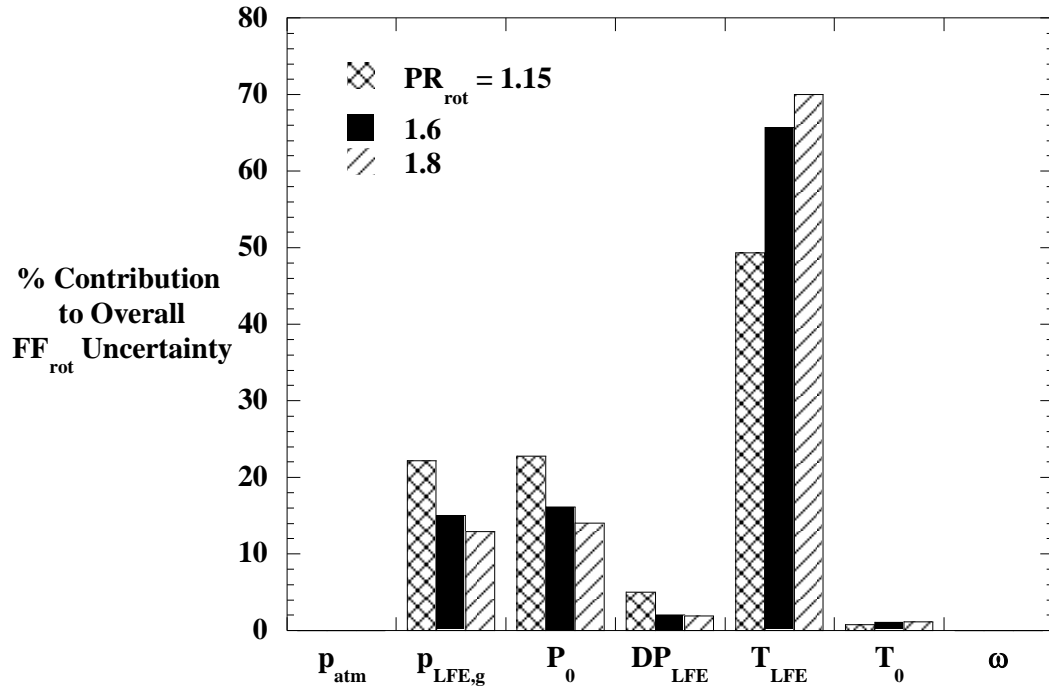


Figure D.1. Relative contributions of the measured parameters to the rotational flow function uncertainty for  $\Omega = 0.002$ .

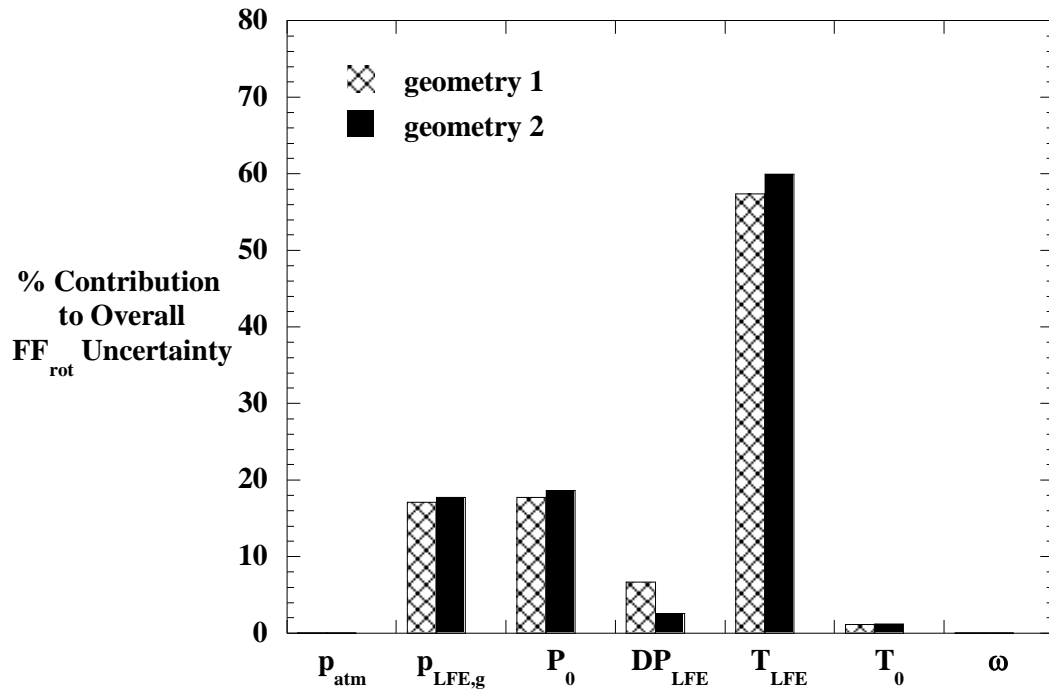


Figure D.2. Relative contributions of the measured parameters to the rotational flow function uncertainty for  $\Omega = 1$ ,  $PR_{\text{rot}} = 1.6$ .

Tables D.1, D.2, and D.3 summarize the uncertainties of parameters used to calculate the flow function for  $\Omega = 0.002$  at rotational pressure ratios of 1.15, 1.6, and 1.8, respectively. Tables D.4 and D.5 summarize the uncertainties of parameters used to calculate the flow function for  $\Omega = 1$  for coupon 1 and 2, respectively.

**Table D.1. Flow Function Parameter Uncertainties for  $\Omega = 0.002$ ,  $PR_{\text{rot}} = 1.15$**

Parameter	Value		Uncertainty	Units	% Contribution to $U_{\text{FFrot}}$
$p_{\text{atm}}$	97.8	$\pm$	0.022	kPa	0.004
$p_{\text{LFE,g}}$	13.7	$\pm$	1.72	kPa	22
$P_0$	111	$\pm$	1.72	kPa	23
$DP_{\text{LFE}}$	0.467	$\pm$	0.003	kPa	5.0
$T_{\text{LFE}}$	21.4	$\pm$	1.70	$^{\circ}\text{C}$	49
$T_0$	25.5	$\pm$	1.70	$^{\circ}\text{C}$	0.77
$\omega$	553	$\pm$	3	rpm	2E-07
$FF_{\text{rot}}$	3.64E-08	$\pm$	1.18E-09	$\text{m-s-K}^{1/2}$	

**Table D.2. Flow Function Parameter Uncertainties for  $\Omega = 0.002$ ,  $PR_{\text{rot}} = 1.6$**

Parameter	Value		Uncertainty	Units	% Contribution to $U_{\text{FFrot}}$
$p_{\text{atm}}$	96.9	$\pm$	0.022	kPa	0.002
$p_{\text{LFE,g}}$	59.3	$\pm$	1.72	kPa	15
$P_0$	155	$\pm$	1.72	kPa	16
$DP_{\text{LFE}}$	0.845	$\pm$	0.003	kPa	2.0
$T_{\text{LFE}}$	21.6	$\pm$	1.70	$^{\circ}\text{C}$	66
$T_0$	25.3	$\pm$	1.70	$^{\circ}\text{C}$	1.1
$\omega$	518	$\pm$	3	rpm	3E-07
$FF_{\text{rot}}$	6.48E-08	$\pm$	1.78E-09	$\text{m-s-K}^{1/2}$	

**Table D.3. Flow Function Parameter Uncertainties for  $\Omega = 0.002$ ,  $PR_{rot} = 1.8$** 

Parameter	Value		Uncertainty	Units	% Contribution to $U_{FFrot}$
$p_{atm}$	96.7	$\pm$	0.022	kPa	0.002
$p_{LFE,g}$	78.3	$\pm$	1.72	kPa	13
$P_0$	174	$\pm$	1.72	kPa	14
$DP_{LFE}$	0.925	$\pm$	0.003	kPa	1.9
$T_{LFE}$	23.6	$\pm$	1.70	$^{\circ}C$	70
$T_0$	26.4	$\pm$	1.70	$^{\circ}C$	1.2
$\omega$	501	$\pm$	3	rpm	3E-07
$FF_{rot}$	6.94E-08	$\pm$	1.81E-09	m-s-K <sup>1/2</sup>	

**Table D.4. Flow Function Parameter Uncertainties  
for Coupon 1,  $\Omega = 1$ ,  $PR_{rot} = 1.6$** 

Parameter	Value		Uncertainty	Units	% Contribution to $U_{FFrot}$
$p_{atm}$	97.9	$\pm$	0.022	kPa	0.003
$p_{LFE,g}$	39.7	$\pm$	1.72	kPa	17
$P_0$	137	$\pm$	1.72	kPa	18
$DP_{LFE}$	0.441	$\pm$	0.003	kPa	6.7
$T_{LFE}$	23.1	$\pm$	1.70	$^{\circ}C$	57
$T_0$	23.1	$\pm$	1.70	$^{\circ}C$	1.1
$\omega$	10342	$\pm$	2	rpm	3E-05
$FF_{rot}$	3.20E-08	$\pm$	9.48E-10	m-s-K <sup>1/2</sup>	

**Table D.5. Flow Function Parameter Uncertainties  
for Coupon 2,  $\Omega = 1$ ,  $PR_{rot} = 1.6$** 

Parameter	Value		Uncertainty	Units	% Contribution to $U_{FFrot}$
$p_{atm}$	97.6	$\pm$	0.022	kPa	0.003
$p_{LFE,g}$	39.2	$\pm$	1.72	kPa	18
$P_0$	137	$\pm$	1.72	kPa	19
$DP_{LFE}$	0.712	$\pm$	0.003	kPa	2.6
$T_{LFE}$	20.3	$\pm$	1.70	$^{\circ}C$	60
$T_0$	20.3	$\pm$	1.70	$^{\circ}C$	1.2
$\omega$	10302	$\pm$	2	rpm	4E-05
$FF_{rot}$	5.22E-08	$\pm$	1.53E-09	m-s-K <sup>1/2</sup>	

## Reduction in Flow Function Uncertainty

An uncertainty analysis was also performed on the rotational pressure ratio ( $PR_{rot}$ ) and reduction in flow function (RFF), defined in Equations D.4 and D.5, respectively. The functional dependence of the rotational pressure ratio on the measured parameters  $P_0$ ,  $T_0$ , and  $\omega$  and on the corrected seal pin differential pressure  $DP_{sp}$  is given in Equation D.6. The functional dependence of RFF on the blocked and baseline rotational flow functions is given in Equation D.7.

$$PR_{rot} = \left( \frac{P_0}{P_0 - DP_{sp}} \right) \left( 1 + \frac{T_{rot}}{T_0} \right)^{\frac{\gamma}{\gamma-1}} \quad (D.4)$$

$$RFF = 1 - \frac{FF_{rot}}{FF_{0,rot}} \bigg|_{PR_{rot}} \quad (D.5)$$

$$PR_{rot} = f(P_0, T_0, \omega, DP_{sp}) \quad (D.6)$$

$$RFF = f(FF_{rot}, FF_{0,rot}) \quad (D.7)$$

Uncertainties for the rotational pressure ratio ( $U_{PR_{rot}}$ ) and the reduction in flow function ( $U_{RFF}$ ) were calculated using the partial derivative method as in Equations D.8 and D.9, respectively. Uncertainty values for pressure ratio and reduction in flow function were previously reported in Table 3.12 for  $\Omega = 0.002$  and Table 3.13 for  $\Omega = 1$ .

$$U_{PR_{rot}} = \sqrt{\left( \frac{\partial PR_{rot}}{\partial P_0} \cdot U_{P_0} \right)^2 + \left( \frac{\partial PR_{rot}}{\partial T_0} \cdot U_{T_0} \right)^2 + \left( \frac{\partial PR_{rot}}{\partial \omega} \cdot U_{\omega} \right)^2 + \left( \frac{\partial PR_{rot}}{\partial DP_{sp}} \cdot U_{DP_{sp}} \right)^2} \quad (D.8)$$

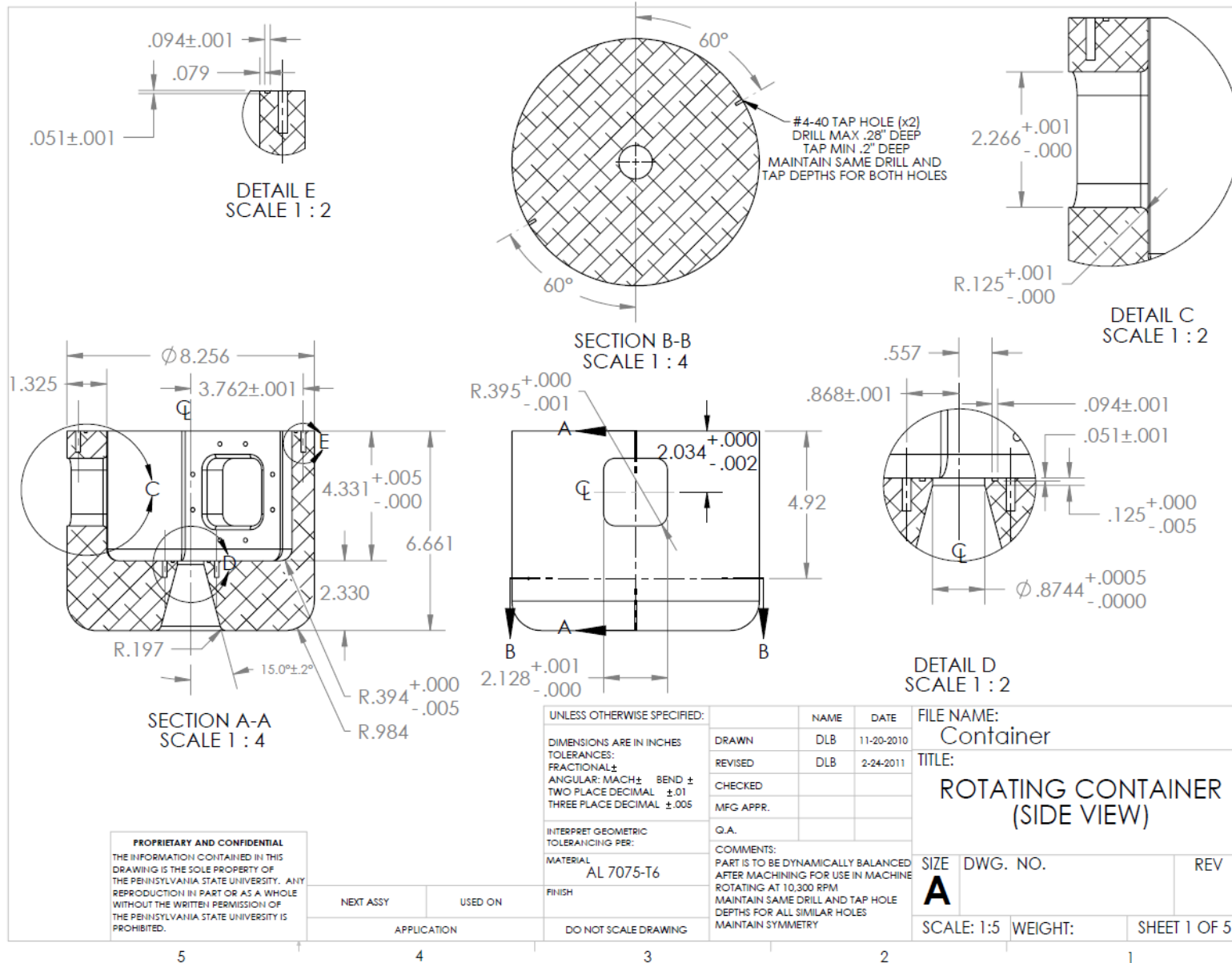
$$U_{RFF} = \sqrt{\left( \frac{\partial RFF}{\partial FF_{rot}} \cdot U_{FF_{rot}} \right)^2 + \left( \frac{\partial RFF}{\partial FF_{0,rot}} \cdot U_{FF_{0,rot}} \right)^2} \quad (D.9)$$

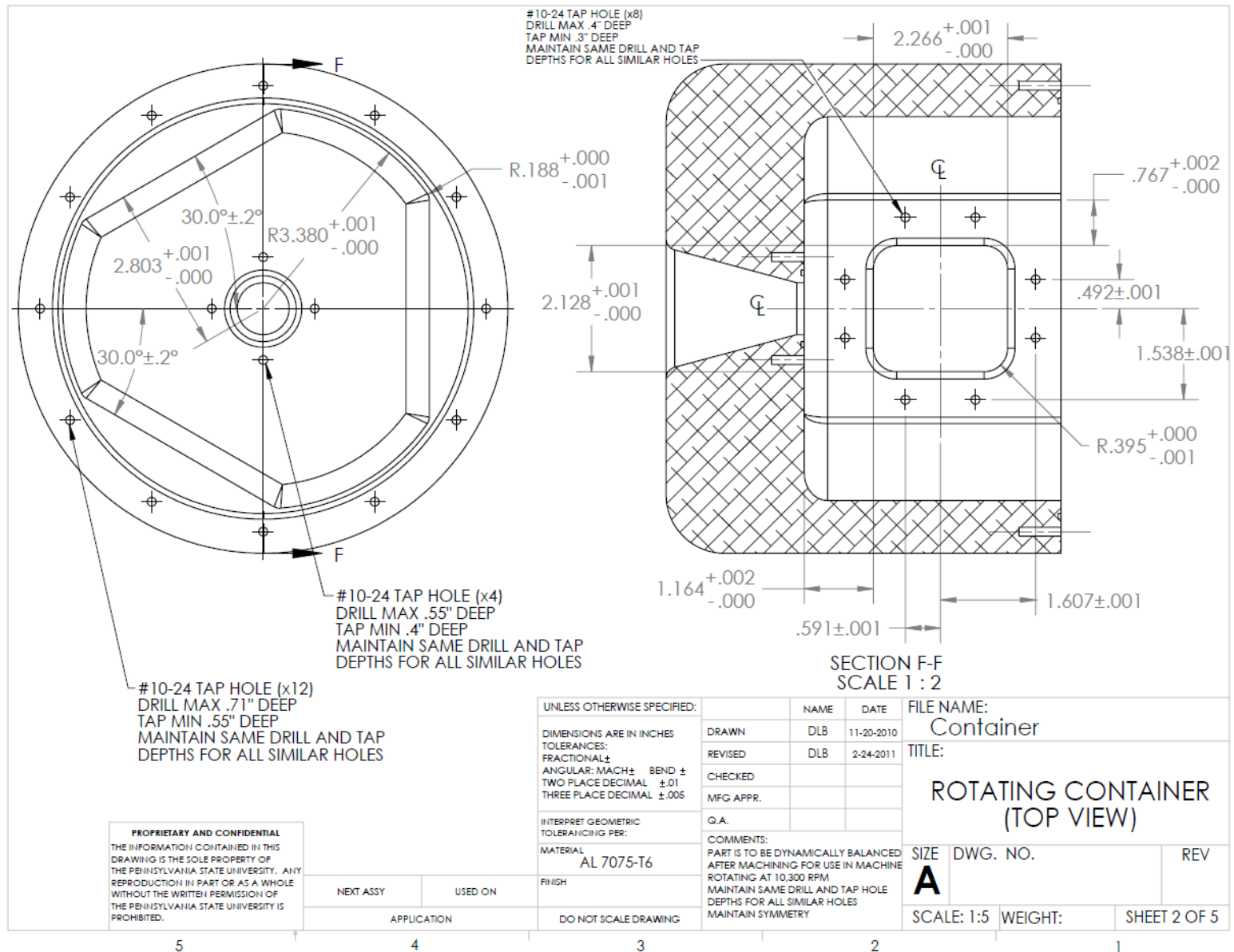
Parameter uncertainties and the overall reduction in flow function uncertainty ( $U_{RFF}$ ) were calculated for  $\Omega = 0.002$  at  $PR_{rot} = 1.15, 1.6$ , and  $1.8$  and for  $\Omega = 1$  for both coupons. As in the static tests, uncertainty in the reduction in flow function was mainly driven by the uncertainty in the flow function at blocked conditions.

## References

- [1] Beckwith, Thomas G., Roy D. Marangoni, and John H. Lienhard V. *Mechanical Measurements, Fifth Ed.* New York: Addison Wesley, 1993.

## **Appendix E. ENGINEERING DRAWINGS**





**PROPRIETARY AND CONFIDENTIAL**  
THE INFORMATION CONTAINED IN THIS DRAWING IS THE SOLE PROPERTY OF THE PENNSYLVANIA STATE UNIVERSITY. ANY REPRODUCTION IN PART OR AS A WHOLE WITHOUT THE WRITTEN PERMISSION OF THE PENNSYLVANIA STATE UNIVERSITY IS PROHIBITED.

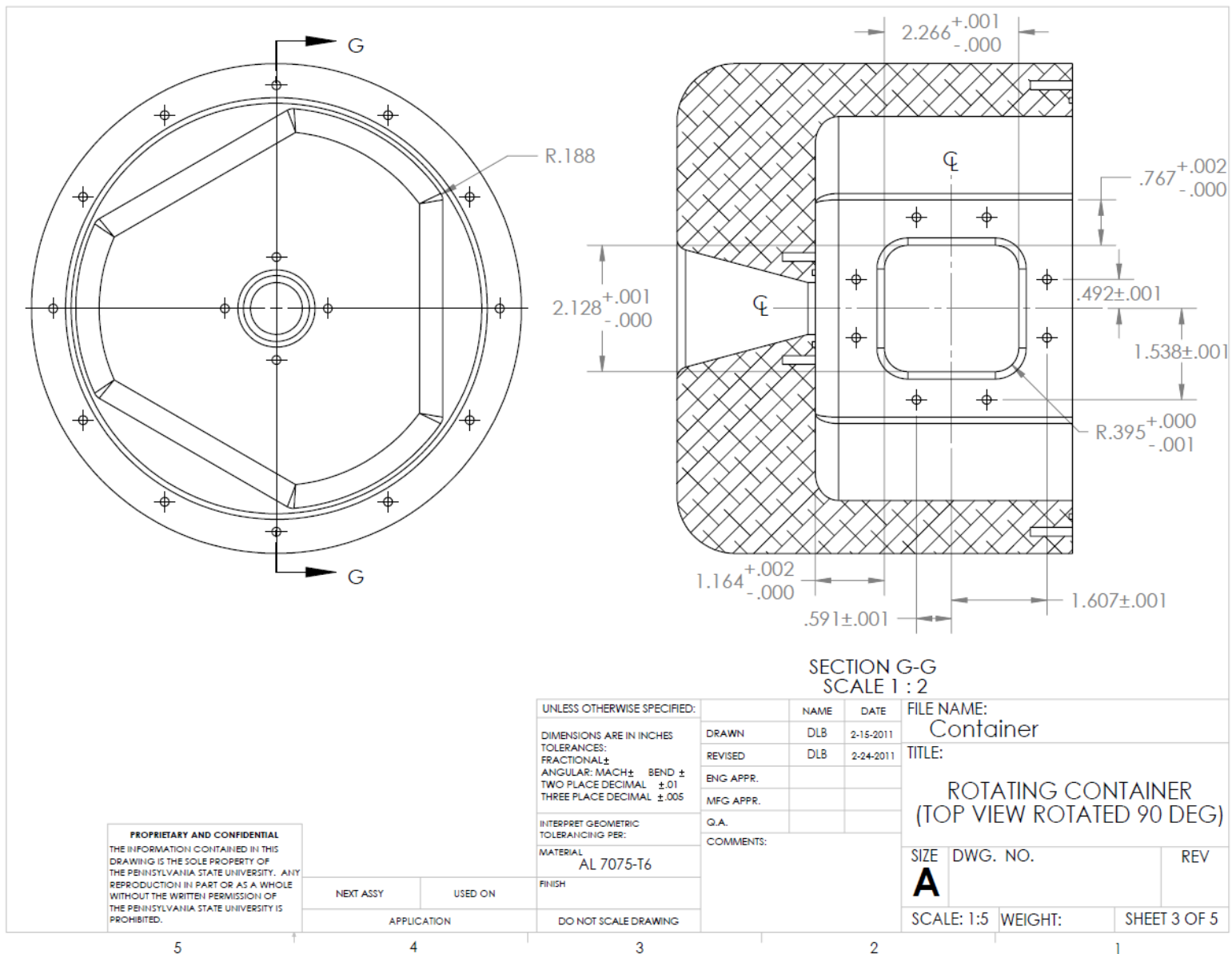
NEXT ASSY USED ON APPLICATION

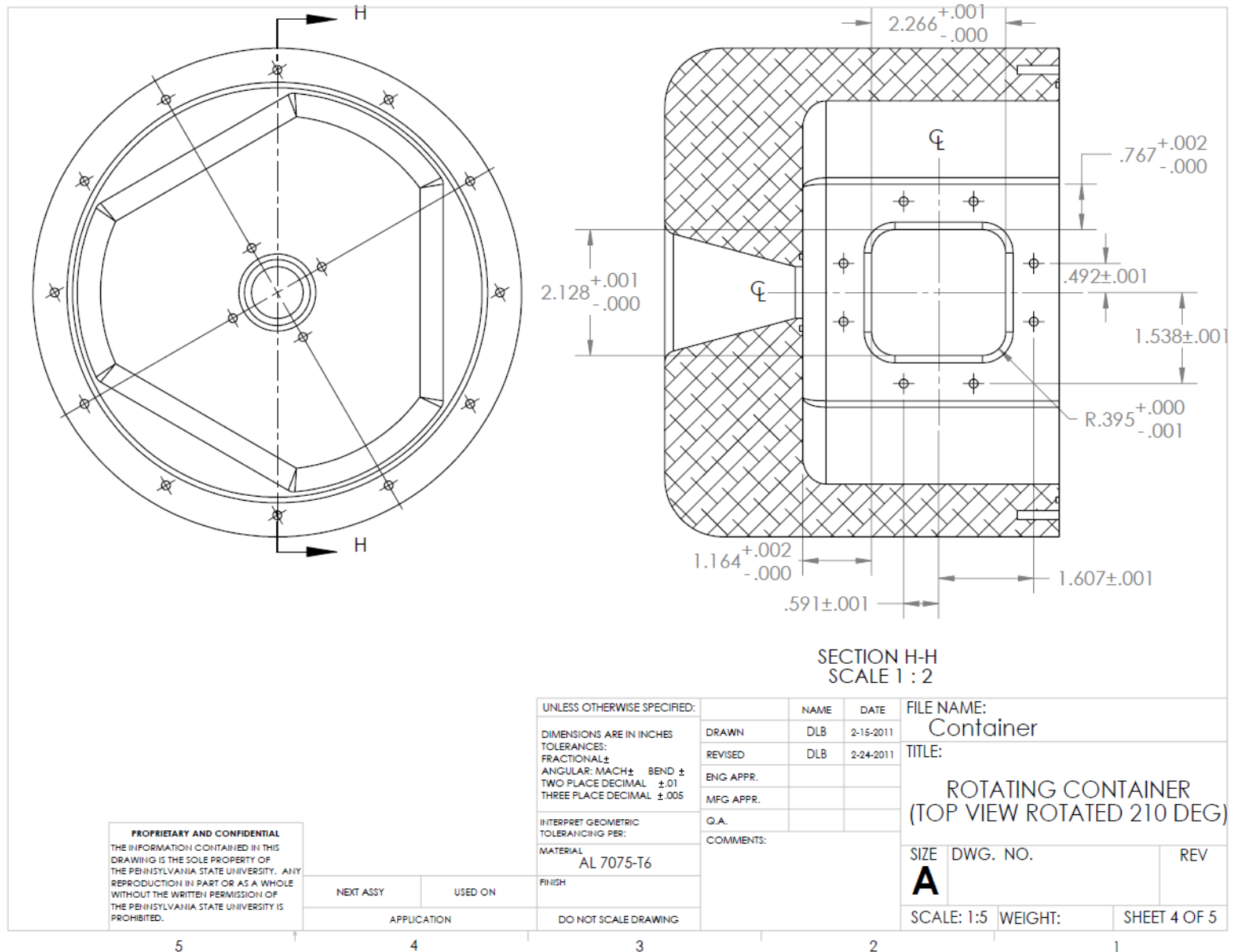
UNLESS OTHERWISE SPECIFIED:  
DIMENSIONS ARE IN INCHES  
TOLERANCES:  
FRACTIONAL ±  
ANGULAR: MACH ± BEND ±  
TWO PLACE DECIMAL ±.01  
THREE PLACE DECIMAL ±.005  
INTERPRET GEOMETRIC TOLERANCING PER:  
MATERIAL AL 7075-T6  
FINISH DO NOT SCALE DRAWING

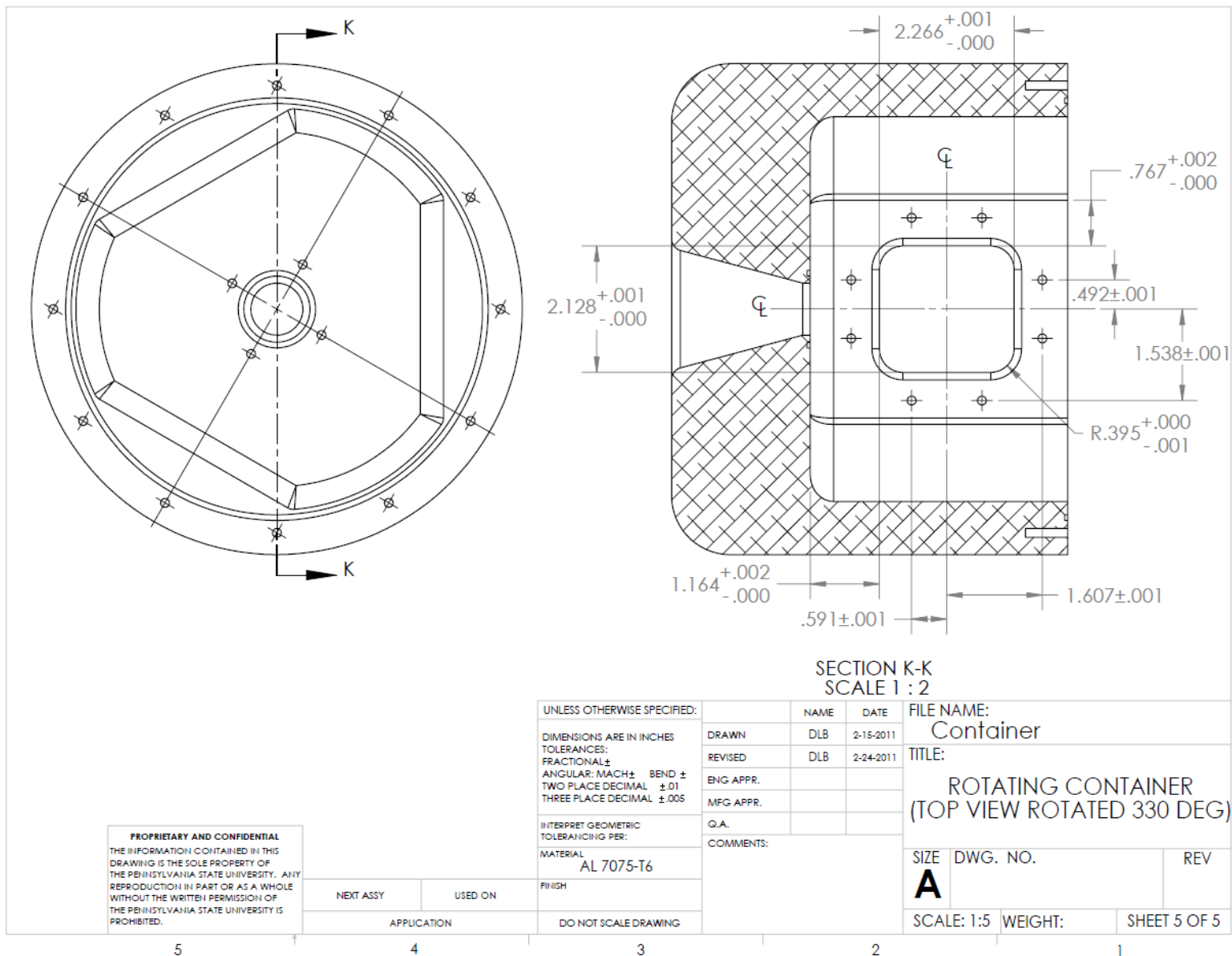
DRAWN DLB 11-20-2010  
REVISED DLB 2-24-2011  
CHECKED  
MFG APPR.  
Q.A.  
COMMENTS:  
PART IS TO BE DYNAMICALLY BALANCED AFTER MACHINING FOR USE IN MACHINE ROTATING AT 10,300 RPM  
MAINTAIN SAME DRILL AND TAP HOLE DEPTHS FOR ALL SIMILAR HOLES  
MAINTAIN SYMMETRY

FILE NAME: Container  
TITLE: ROTATING CONTAINER (TOP VIEW)  
SIZE DWG. NO. REV  
SCALE: 1:5 WEIGHT: SHEET 2 OF 5

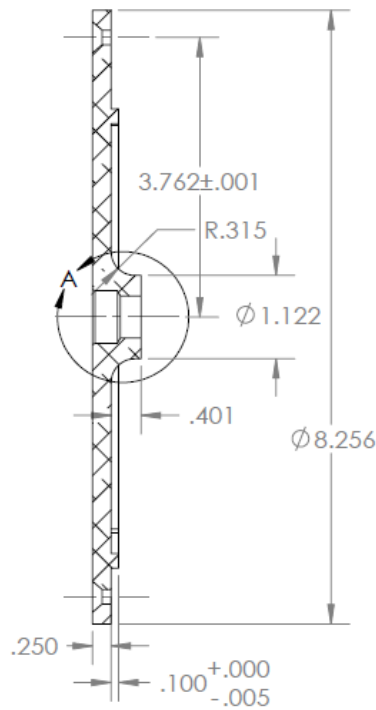
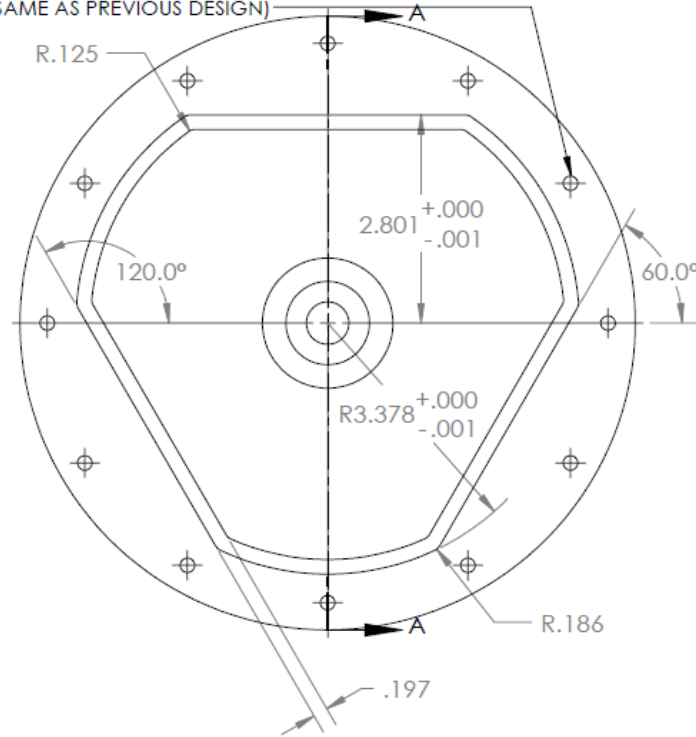






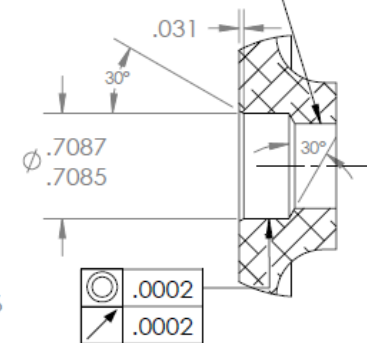


#10-24 CLEARANCE HOLE (x12)  
82 DEG C-SINK FLUSH ON REVERSE SIDE  
MAINTAIN SAME C-SINK DEPTH  
FOR ALL SIMILAR HOLES  
(SAME AS PREVIOUS DESIGN)



SECTION A-A  
SCALE 1 : 2

M16x1.5 LEFT HAND  
THREAD TAP HOLE



DETAIL A  
SCALE 1 : 1  
(SAME AS PREVIOUS DESIGN)

**PROPRIETARY AND CONFIDENTIAL**  
THE INFORMATION CONTAINED IN THIS  
DRAWING IS THE SOLE PROPERTY OF  
THE PENNSYLVANIA STATE UNIVERSITY. ANY  
REPRODUCTION IN PART OR AS A WHOLE  
WITHOUT THE WRITTEN PERMISSION OF  
THE PENNSYLVANIA STATE UNIVERSITY IS  
PROHIBITED.

NEXT ASSY

USED ON

APPLICATION

UNLESS OTHERWISE SPECIFIED:

DIMENSIONS ARE IN INCHES  
TOLERANCES:  
FRACTIONAL ±  
ANGULAR: MACH ± BEND ±  
TWO PLACE DECIMAL ±.01  
THREE PLACE DECIMAL ±.005

INTERPRET GEOMETRIC  
TOLERANCING PER:

MATERIAL  
AL 7075-T6

FINISH

DO NOT SCALE DRAWING

NAME	DATE
DRAWN DLB	6-14-2011
CHECKED	
ENG APPR.	
MFG APPR.	
Q.A.	
COMMENTS:	
FOR USE IN MACHINE ROTATING AT 10,300 RPM	
FITS WITH PART CALLED "ROTATING CONTAINER"	

FILE NAME: Lid_Reduced_Mass		
TITLE:  REDUCED MASS CONTAINER LID		
SIZE <b>A</b>	DWG. NO.	REV
SCALE: 1:2	WEIGHT:	SHEET 1 OF 1

5

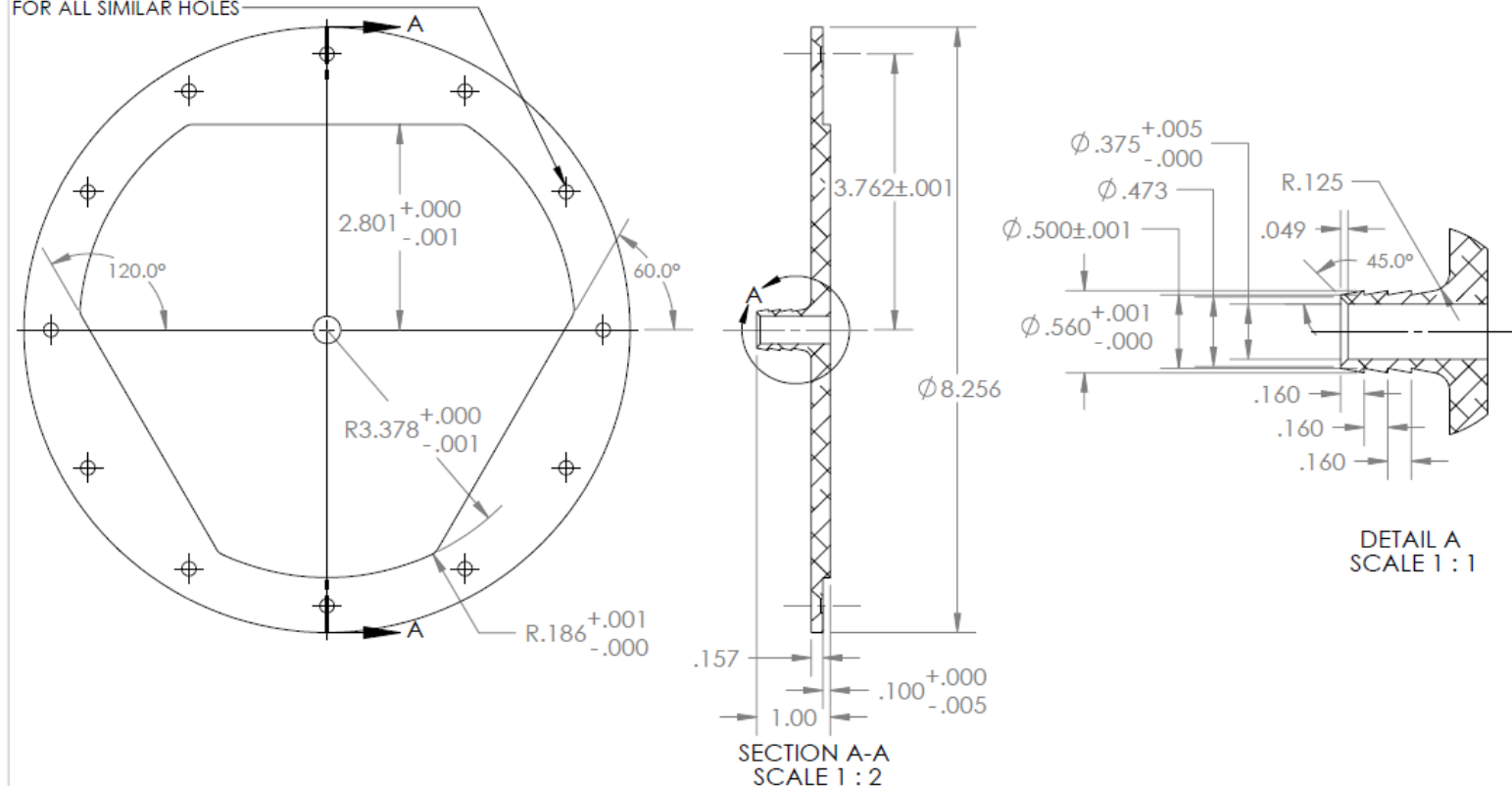
4

3

2

1

#10-24 CLEARANCE HOLE (x12)  
82 DEG C-SINK FLUSH ON REVERSE SIDE  
MAINTAIN SAME C-SINK DEPTH  
FOR ALL SIMILAR HOLES



**PROPRIETARY AND CONFIDENTIAL**  
THE INFORMATION CONTAINED IN THIS  
DRAWING IS THE SOLE PROPERTY OF  
THE PENNSYLVANIA STATE UNIVERSITY. ANY  
REPRODUCTION IN PART OR AS A WHOLE  
WITHOUT THE WRITTEN PERMISSION OF  
THE PENNSYLVANIA STATE UNIVERSITY IS  
PROHIBITED.

		UNLESS OTHERWISE SPECIFIED:		NAME		DATE		FILE NAME: Lid with Hose Barb	
		DIMENSIONS ARE IN INCHES		DRAWN		DLB		6-21-2011	
		TOLERANCES:		REVISED		DLB		6-22-2011	
		FRACTIONAL ±		ENG APPR.				TITLE:  CONTAINER LID WITH HOSE BARB	
		ANGULAR: MACH ± BEND ±		MFG APPR.					
		TWO PLACE DECIMAL ±.01		G.A.					
		THREE PLACE DECIMAL ±.005		COMMENTS:					
		INTERPRET GEOMETRIC TOLERANCING PER:		PART IS TO BE DYNAMICALLY BALANCED AFTER MACHINING FOR USE IN MACHINE ROTATING AT 10,300 RPM		SIZE <b>A</b>		DWG. NO.	
		MATERIAL							
		AL7075-T6						REV	
NEXT ASSY		USED ON		FINISH					
APPLICATION		DO NOT SCALE DRAWING		FITS WITH PART CALLED "ROTATING CONTAINER"		SCALE: 1:2		WEIGHT:	
								SHEET 1 OF 1	

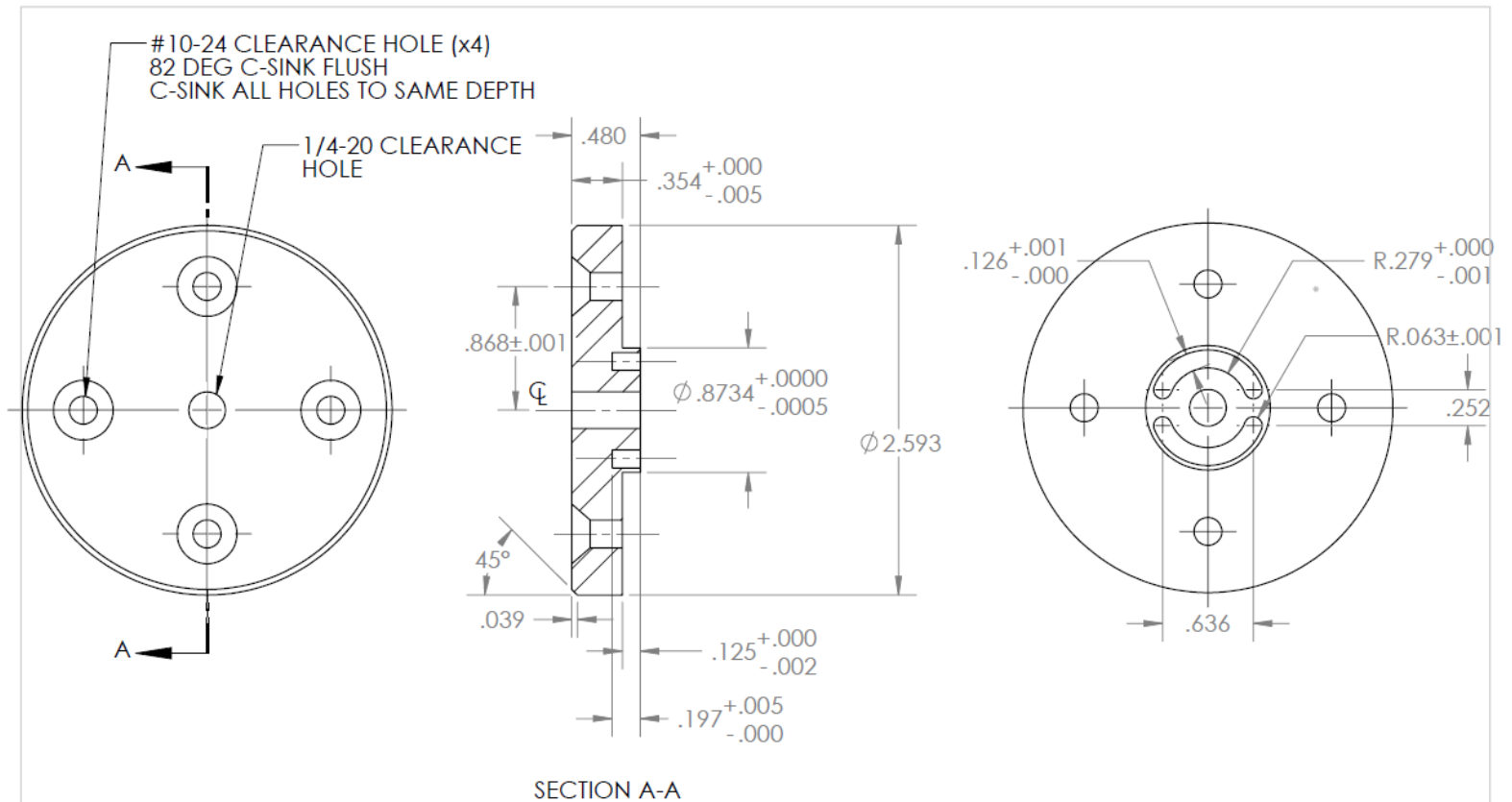
5

4

3

2

1



SECTION A-A

**PROPRIETARY AND CONFIDENTIAL**  
 THE INFORMATION CONTAINED IN THIS DRAWING IS THE SOLE PROPERTY OF THE PENNSYLVANIA STATE UNIVERSITY. ANY REPRODUCTION IN PART OR AS A WHOLE WITHOUT THE WRITTEN PERMISSION OF THE PENNSYLVANIA STATE UNIVERSITY IS PROHIBITED.

		UNLESS OTHERWISE SPECIFIED:		NAME		DATE		FILE NAME:	
		DIMENSIONS ARE IN INCHES		DRAWN		DLB		Collar	
		TOLERANCES:		REVISED		DLB		2-24-2011	
		FRACTIONAL ±		ENG APPR.				TITLE:	
		ANGULAR: MACH ± BEND ±		MFG APPR.					
		TWO PLACE DECIMAL ±.01		Q.A.					
		THREE PLACE DECIMAL ±.005						ROTATING CONTAINER COLLAR	
		INTERPRET GEOMETRIC TOLERANCING PER:		COMMENTS:					
		MATERIAL		AFTER MACHINING HEAT TREAT TO MINIMUM 60HRC					
		SS 440A, 440B, OR 440C		FITS WITH PART CALLED "ROTATING CONTAINER"				SIZE	
		FINISH						DWG. NO.	
		NEXT ASSY		USED ON				REV	
		APPLICATION		DO NOT SCALE DRAWING				SCALE: 1:1	
								WEIGHT:	
								SHEET 1 OF 1	

5

4

3

2

1

